PHYSICAL MODULATION TO THE BIOLOGICAL PRODUCTION IN THE SOUTH CHINA SEA: A PHYSICAL-BIOLOGICAL COUPLED MODEL APPROACH

by

Wenfang Lu

A dissertation submitted to the Faculty of the University of Delaware in partial fulfillment of the requirements for the degree of Doctor of Philosophy in Oceanography

Fall 2017

PHYSICAL MODULATION TO THE BIOLOGICAL PRODUCTION

IN THE SOUTH CHINA SEA:

A PHYSICAL-BIOLOGICAL COUPLED MODEL APPROACH

by

Wenfang Lu

Approved: ______________________________

Mark A. Moline, Ph.D.
Director of the School of Marine Science and Policy

Approved: ______________________________

Estella Atekwana, Ph.D.
Dean of the College of Earth, Ocean, and Environment

Approved: ______________________________

Ann L. Ardis, Ph.D.
Senior Vice Provost for Graduate and Professional Education

I certify that I have read this dissertation and that in my opinion it meets the academic and professional standard required by the University as a dissertation for the degree of Doctor of Philosophy.

Signed:

Xiao-Hai Yan, Ph.D.
Professor in charge of dissertation

I certify that I have read this dissertation and that in my opinion it meets the academic and professional standard required by the University as a dissertation for the degree of Doctor of Philosophy.

Signed:

Yuwu Jiang, Ph.D.
Member of dissertation committee

I certify that I have read this dissertation and that in my opinion it meets the academic and professional standard required by the University as a dissertation for the degree of Doctor of Philosophy.

Signed:

I. Pablo Huq, Ph.D.
Member of dissertation committee

I certify that I have read this dissertation and that in my opinion it meets the academic and professional standard required by the University as a dissertation for the degree of Doctor of Philosophy.

Signed:

Wei Zhuang, Ph.D.
Member of dissertation committee

ACKNOWLEDGMENTS

I would like to thank my advisor, Dr Xiao-Hai Yan, and co-advisor, Dr Yuwu Jiang, for their support and help. I, who started graduate study as a nothing-knower in Oceanography, cannot finish this dissertation without their detailed guidance. Dr Xiao-Hai is my guiding star in the ocean, pointing towards the direction of excellence. Dr Yuwu is a great mentor, not only helpful in academia but also in my life. I am so grateful to work with you.

I would like to extend my gratefulness to all my colleagues during my PhD study, especially to Dr Pablo Huq and Dr Wei Zhuang for their creative inputs, suggestions and comments. I also thank the lecturers of my courses, Dr Tobias Kukulka, Dr Andreas Münchow, Dr Fabrice Veron and Dr Matthew Oliver, since I learnt so much from you. Thanks to the graduate students in Robinson Hall for the engraved happy memories with all of you, especially, Enhui Liao, Dong Wang, Jin Sha, Zheguang Zou, Lu Han, Helen, Chi Yan, Yuening Ma, Peter Washam, Alfred Yan, and Andre Rodrigues, my best friends in UD.

Sincerely, thank you.

This work is dedicated to my beloved fiancée, Ms Xixi Chen.

TABLE OF CONTENTS

LIST OF TABLES

LIST OF FIGURES

ABSTRACT

South China Sea (SCS) is a typical marginal sea with the characteristics of open ocean. This distinct property makes SCS an ideal environment to study the modulation mechanisms from various physical processes to the marine biogeochemical (BGC) system. In order to comprehensively investigate the role of various physical processes, such as oceanic circulation, mesoscale eddies, atmospheric forcing, and oceanic fronts, two case studies were conducted in this dissertation with focus on the two hotspots identified by reviewing previous literatures on the BGC systems of the SCS, i.e., winter bloom in the Luzon Strait (referred as LZB), and the summer Vietnam boundary upwelling system (VBUS).

For the case study on the LZB, a coupled physical-biological (TFOR-NPZD) model was developed in order to study the mechanisms. Based on a simulation for 2010, the results showed that the TFOR-NPZD model was capable of reproducing the key features of the LZB, such as the location, inverted-V shape, twin-core structure and bloom intensity. The simulation showed that the LZB was triggered during the relaxation period of intensified northeasterly winds of the winter monsoon, when the deepened mixed layer started to shoal. Nutrient diagnostics showed that vertical mixing was responsible for the nutrient supply to the upper ~40 m layer, while subsurface upwelling supplied nutrients to the region below the mixed layer. Hydrodynamic diagnostics showed that the advection of relative vorticity (RV) primarily contributed to the subsurface upwelling. The RV advection was resulted

from an offshore jet, which was associated with a northeasterly wind, flowed across the ambient RV field.

For the process-oriented case study on the VBUS, investigation on the remote sensing data revealed a tight spatio-temporal covariance of the biological productivity and the circulation. High level of biological production was associated with high level of surface current intensity, which accounted for ~12% of the variability in the production. A coupled physical-biological (TFOR-CoSiNE) model with the emphasis on the mesoscale phenomena was developed to study the detailed processes in VBUS. Validation against satellite and *in-situ* data suggested that the capability of the model system in reproducing the key features of the summer VBUS, including the positive contribution from the circulation. Inspection into the model results highlighted the circulation's role in local BGC system, where the separation and the anticyclone pattern from the circulation were favorable for the recycling of the nutrients. The weakened circulation was associated with an abnormal non-separated circulation pattern, which would leak the organic matters and reduce the nutrient inventory in the VBUS. In a numerical experiment where the circulation was manipulated presenting a weak tendency of separation, the nitrate inventory could be reduced by ~25% while the production reduced by ~16%, demonstrating the significance of the circulation's role.

The previous two case studies demonstrate that the above-mentioned physical processes not only redistribute the water with high biological productivity, but also systematically modify the source-and-sink pattern of nutrient (mainly nitrogen) as the most important limiting factor of biological production in the oligotrophic SCS. By inducing vertical motion of water mass and horizontal transport of high nutrient coastal water, physical processes fuel the nutrient available for biological production in the upper layer via various mechanisms. Thus, the BGC cycle in the SCS is highly modulated by the physical dynamical processes.

Chapter 1

INTRODUCTION

1.1 South China Sea: Physical Setting

The South China Sea (SCS) is a large semi-enclosed marginal sea located in the subtropical western Pacific Ocean. It spans from approximately 3°S at the coasts of Borneo and Sumatra to 23°N at the southern coasts of China; and from 99°E to 121°E covering the sea area from Malaysian Peninsula to the western Philippine Islands [*Wong et al.*, 2007; *Wyrtki*, 1961]. The approximate area of SCS is 3.5×10^6 km^2. The SCS is bordered by extensive continental shelves (e.g., along southern coasts of China, and southern coasts of Vietnam), and consists of deep interior basin which can be as deep as 5000 m (ca. 60% by area) [*K-K Liu et al.*, 2010; *Wong et al.*, 2007]. Counterclockwise, the SCS exchanges its water with the western North Pacific Ocean through the Luzon Strait (LS), with Eastern China Sea through the Taiwan Strait, with the Java Sea through the Karimata Strait, and with the Sulu Sea through the Mindoro Strait [*Zhuang et al.*, 2010b]. Among these channels, the LS is the only major channel that allows significant water mass exchange with the open ocean due to its relative deep depth (sill ~2400 m, [*K K Liu et al.*, 2002]).

The SCS is predominantly controlled by the East Asian Monsoon, which has southwesterly winds in the summer, from June to September, and strong northeasterly winds from November to the March of next year [*Liu et al.,* 2002]. During northeastern monsoon season, the prevailing wind has a magnitude of 9 m s^{-1}, while the southwestern winds are about 6 m s^{-1} in summer [*Hu et al.*, 2000]. Under the influence of the East Asian Monsoon, cyclonic and anti-cyclonic basin-scale surface circulations are formed in winter and summer, respectively [*Gan and Qu*, 2008; *Hu et al.*, 2000]. Due to its location in the tropical zone, the sea surface temperature (SST) is consistently high all year round [*Wong et al.*, 2007]. Strong stratification inhibits surface wind-induced mixing, resulting in shallow mixed layer depth of ~20 m in summer and ~80 m in winter [*C-M Tseng*, 2005; *Wong*, 2002].

The Kuroshio flows northward but frequently penetrates the SCS from the surface and deep layers of the LS [*G Wang et al.*, 2012]. The transport of the Luzon Strait are hence characterized with an annual westward flux of ~4-10 Sv and a “sandwich-like” vertical structure, which is inward to the SCS in the surface and deep layer and outward in the intermediate layer [*Gan et al.*, 2016; *Qu*, 2000; *Xu and Oey*, 2014]. The circulation of SCS is profoundly influencedby the sandwich-like transport. For the deep layer, the inflow from the open Pacific Ocean cooler and denser than the SCS water sinks to the deep basin of SCS [*Qu et al.*, 2006]. Since SCS interior basin below 2400 m is completely isolated [*Dai et al.*, 2013], the overflow should be counterbalanced by upwelling [*G Wang et al.*, 2011] or diapycnal mixing [*Tian et al.*, 2009] in order to conserve water mass in the deep basin. The resultant intensive vertical exchange also results in the relatively short renew time of the SCS water [*Wong et al.*, 2007]. Forced by the external input of planetary vorticity flux in each layer, and also in addition by the east Asian Monsoon, the circulation in the SCS presents cyclonic-anticyclonic-cyclonic pattern from surface to the deep [*Gan et al.*, 2016; *Qu et al.*, 2000].

The Kuroshio loop current drives both cyclonic and anticyclonic mesoscale eddies near the LS through eddy shedding [*Wu and Chiang*, 2007; *Metzger and Hurlburt*, 2001; *Wang et al.*, 2003]. On average, 32.8 mesoscale eddies are observed by altimetry per year, ~52% being cyclonic [*Xiu et al.*, 2010]. The genesis of mesoscale eddies in the SCS presents geographical identity, which could be grouped into Kuroshio-, wind-curl-, or local circulation-driven [*G Wang et al.*, 2003].

1.2 South China Sea: Biogeochemistry

Because basin-scale gyres in the surface circulation isolate the interior water of the SCS, this area is characterized by oligotrophic water, despite of the terrestrial inputs from several rivers [*Wong et al.*, 2007]. Therefore, the surface chlorophyll-a concentration (hereafter, CHL), which is widely used as an indicator of the primary producer biomass, in the SCS is typically at low (~0.1 mg m^{-3}) level [*I I Lin et al.*, 2010]. Mostly controlled by the monsoon, the surface CHL shows substantial seasonality, which is highest in winter and lowest in summer [*K K Liu et al.*, 2002]. As a result, in terms of carbon cycle as a whole, SCS serves as a weak CO_2 source to the atmosphere, especially during summer [*Dai et al.*, 2013]. At longer temporal scale, the variation of CHL is also modulated by ENSO cycle [*Kuo et al.*, 2004; *Palacz et al.*, 2011; *S P Xie et al.*, 2003], and the global climate changes [*Ning et al.*, 2009].

Previous studies of the biogeochemistry in the SCS identify two hotspots: winter Luzon bloom (LZB) and summer Vietnam Boundary Upwelling System (VBUS). The properties and distinctions of the two ecosystems are reviewed below.

1.2.1 Winter Luzon Upwelling (LZU) and Associated Bloom (LZB)

Winter Luzon Blooms (LZB), which have been confirmed by many observational and remote sensing studies, occasionally appear northwest of the Luzon Island. In contrast with common spring phytoplankton blooms over the continental shelf

[*Sverdrup*, 1953; *Townsend et al.*, 1992], the LZB usually flourishes in winter over water depths greater than 2500 m [*Tang et al.*, 1999]. In the oligotrophic SCS, blooms have a pulse impact on the productivity of the local marine ecosystem, and hence on ocean carbon flux [*Townsend et al.*, 1992]. Moreover, studying the dynamics of the LZB will increase understanding of the complex biogeochemical circumstances near the LS.

The oceanography community has investigated the remarkable spatial and temporal features and significance of the LZB. *Shaw et al.* [1996] discovered the subsurface upwelling off the northeastern coast of the Luzon Island from hydrologic data taken in December 1990. From the pigment concentration results of historical Coastal Zone Color Scanner (CZCS) data from 1979 to 1986, *Tang et al.* [1999] found that the LZB occurred in December 1979, February 1983, February 1985, and January 1986. *Shang et al.* [2012] revealed that the bloom generally persists from November to February, and peaks in December. *Peñaflor et al.* [2007] showed that the LZB reached its maximum intensity in early spring with approximate chlorophyll-a (hereafter CHL) concentrations of 2.0 mg m^{-3}. Using an analytically derived phytoplankton absorption coefficient, *Shang et al.* [2012] revealed the explicit inverted-V and two-wing (nearshore and offshore) structure of the LZB from satellite images. The nearshore wing of the LZB was investigated for the first time by *Peñaflor et al.* [2007] and they attributed its structure to lee effects from the Kuroshio flowing pass the Luzon Island. The riverine influences from the Cagayan River and the Gaoping River are localized relative to the Kuroshio influence. On the other hand, for the offshore bloom patch, possible nutrient sources proposed by *Tang et al.* [1999] were (1) remote advection from the nearshore, (2) local upwelling by fronts or eddy processes or (3) enhanced vertical mixing.

Many different mechanisms for the offshore bloom have been proposed and discussed. [*C-C Chen et al.*, 2006] inferred from in-situ data that a shallower mixed layer depth (MLD) in winter was associated with upwelling caused by Ekman pumping. *J J Wang et al.* [2010] found that the MLD, which was derived from NASA's Ocean Biogeochemical Model, became deeper in winter, and classical Ekman pumping theory was highlighted to be responsible for the LZB in collaboration with wind-induced mixing. In addition to the wind-induced upwelling mechanism, Kuroshio loops across the middle of the LS could also be responsible for the LZB [*Peñaflor et al.*, 2007; *Shang et al.*, 2012]. Local upwelling related to Kuroshio-eddy interaction or Kuroshio-topography effects can be deduced from remote sensing evidence [*Shang et al.*, 2012]. *Peñaflor et al.* [2007] proposed that the LZB was associated with the interaction between Kuroshio and the basin circulation; however, the underlying mechanism was not clear. *Shaw et al.* [1996] noted that the driving force for the upwelling was associated with the sub-basin scale deep circulation, namely the Luzon Coastal Current (LCC) reported by [*Fang et al.*, 1998] and [*Hu et al.*, 2000]. This genesis mechanism was also invoked by *K K Liu et al.* [2002]. Beyond the above effects, eddy pumping effects on the LZB was also highlighted by *Y-L L Chen et al.* [2007]. The dynamics of SCS was characterized by vigorous eddy activity with eddy-generated vertical exchanges playing an essential role in the upper ocean ecosystem [*Klein and Lapeyre*, 2009]. Mesoscale activity in this area may also dramatically modify the vertical distribution and horizontal pattern of nutrients, thereby affecting productivity.

1.2.2 Vietnam Boundary Upwelling System (VBUS)

During southwestern monsoon period, upwelling-favorable wind prevails near the Vietnamese coasts. The offshore Ekman transport drives surface divergence, thus results in upwelling of cold and nutrient-replete subsurface water along the bottom (hereafter referred as VBUS). Centered at ~109ºE between 14ºN and 17ºN along the Vietnamese coast [*Loisel et al.*, 2017], the upwelling was confirmed by cruise investigation [*Dippner et al.*, 2006] and remote sensing observation [*Kuo et al.*, 2000]. This phenomenon has also been examined with regional ocean models [*Chai et al.*, 2009; *G Liu and Chai*, 2009; *K K Liu et al.*, 2002].

In VBUS, the extent and intensity of the upwelling is primarily controlled by the wind speed of the alongshore component of the monsoon, likewise in other coastal upwelling system, such as the coastal upwelling system of California or mid-Atlantic Bight [*Gruber et al.*, 2011]. Compared with the latter two, VBUS appears to be the most intensive one, which was revealed by intercomparison of surface temperature drawdown (3~5 ^{o}C for VBUS) and cold filament length (~500 km) [*Kuo et al.*, 2004]. To the first order, the seasonality of the VBUS and co-occurred coastal phytoplankton bloom was driven by the seasonal cycle of the East Asian Monsoon [*K K Liu et al.*, 2002].

At various temporal scales, the monsoon is modulated by climatic variation. For instance, at interannual scale, El Niño events generally weaken the monsoon, resulting in higher SST and lower productivity during the summer following the recent El Niño event [*Dippner et al.*, 2006; *Hein et al.*, 2013]. Delayed by six month, the intensity of upwelling-related cold filament well correlates with the ENSO [*S P Xie et al.*, 2003]. The influence of ENSO is further prolonged by the Indian Ocean Dipole (IOD) mode [*S-P Xie et al.*, 2009]. Positive IOD and La Niña event is favorable to the upwelling and bloom intensity [*X Liu et al.*, 2012]. Besides, at 30-60 day periods, the Madden-Julian Oscillation is considered a major cause in modulating the summer SST anomaly with approximate one-week delay [*X Liu et al.*, 2012].

In addition to the modulation of climatic variability, local land-air-sea interaction also systematically modifies the VBUS system. The north-south running mountain blocks the southwesterly winds, forming a strong wind jet off east of Vietnam. Accompanied with intense wind curls (positive curl in the north), offshore cold filament jet is driven [*Gan and Qu*, 2008]. At vertical, the offshore jet is relatively homogeneous because it is largely barotropic, extending from surface to at least 200 m depth [*Gan and Qu*, 2008]. The cold offshore jet disrupts the summer SST warming, resulting in a semi-annual SST variation in the SCS [*S P Xie et al.*, 2003]. In addition, the cold filament further feedbacks to the air, leading to ~30% reduction of the wind speed by enhancing the onshore sea-breeze [*Zheng et al.*, 2016].

Not only modulated by the atmospheric forcing, VBUS is also subjected to the mesoscale activities. In summer, spot with high mesoscale activity appears at ~12ºN offshore [*Loisel et al.*, 2017], in consistent with the offshore extension of the cold filament and high CHL water, but the relationship between ocean dynamics and productivity was not fully understood. The variation associated with the mesoscale processes may account for up to 35% of the total CHL variance in the central VBUS [*Loisel et al.*, 2017].

Mesoscale eddies play a significant role in shaping the dynamical structure of boundary upwelling system [*Capet et al.*, 2008]. Conceptually, the major mechanisms affecting upper layer CHL responses to mesoscale eddies are eddy pumping, wind/eddy interaction, eddy-Ekman pumping, eddy stirring (i.e., horizontal advection), and submesoscale pumping [*D. A. Siegel et al.*, 2011]. Additionally, in high latitude North Atlantic, mesoscale eddies-induced stratification also favors the spring bloom by providing stabilized water condition [*Mahadevan et al.*, 2012]. With a physical-biological coupled model, *Guo et al.* [2015] found that the ecosystem responses were nonlinear with respect to the eddy lifetime in the SCS. Although nonlinear, the mechanism to the first order can be explained by the conventional eddy pumping theory [*Falkowski and Ziemann*, 1991]. Focus on the western SCS eddies, *F Liu et al.* [2016] revealed an asymmetric pattern of the CHL distribution composited from more than 400 anti-cyclonic eddy individuals. The asymmetry coincided with the non-uniform surface velocity, which induced ageostrophic secondary vertical circulation, thereby increasing phytoplanktonic production [*F Liu et al.*, 2016]. Eddy-Ekman pumping mechanism was also supported by remote sensing and numerical simulation evidences, which was also depended on the shape of mesoscale eddies [*J Li et al.*, 2014]. *He et al.* [2016] and *F Liu et al.* [2013a] highlighted both the eddy pumping and eddy stirring mechanisms. All in one, the linkage between the ecosystem and mesoscale eddies in the SCS were extensively studied.

Chapter 2

OPEN ISSUES

Based on previous literature in Chapter 1, the mechanisms of the blooms in the SCS and their relationship with physical processes are still under hot discussion. While most of these studies invoked statistical methods to analyze the composite-mean property of bio-optical footprints, the dynamical processes underlying the various mechanisms are not yet fully understood. Because time and space limitations exist (e.g., cloud contamination or weather constraints), neither episodic remote sensing images nor relatively static *in-situ* observations will allow us to fully understand the physical-biogeochemical coupling in the SCS. Moreover, previous studies based on remotely sensed satellite images were incapable to distinguish the contributions from the above-mentioned mechanisms. With the approach of numerical simulation, the various mechanisms can be diagnosed and quantified. This is the motivation of this study to investigate and discuss these phenomena.

Chapter 3

OBJECTIVES

The overall hypothesis of this study is: **physical processes, including but not limiting to mesoscale eddies, wind, mean circulation, and oceanic fronts, not only redistribute the surface water with higher biological productivity, but also systematically modify the source-and-sink pattern of the nutrient in the upper ocean of the SCS. Thus, the biogeochemical cycle in the SCS is highly modulated by the physical processes.** To support this hypothesis, two case-studies were conduct, corresponding to the two important ecosystems in the SCS: the LZB and VBUS systems, by using coupled three-dimensional circulation models and analyzing available remote sensing data.

The objectives of the first topic, focusing on the LZB system, are (1) to examine the role of various physical processes (e.g., northeasterly monsoon, coastal current, Kuroshio loop current and eddy activities) on the LZB in a realistic ocean scenario; (2) to provide dynamic interpretation for the conceptual mechanism models in previous studies [*Peñaflor et al.*, 2007; *Wang et al.*, 2010]; (3) to shed lights on the triggering and sustaining factors of the blooms.

The objectives of the second topic, emphasizing on the VBUS system, are (1) to understand the physical mechanisms by which the biological production in the VBUS is modulated; (2) to quantify the contribution of the circulation to the planktonic ecosystem in VBUS, more specifically, to the nutrient input and redistribution; (3) ultimately to gain insights into the understanding of the biogeochemical system in

VBUS as a complex and representative boundary upwelling system modulated by monsoon.

Because time and space limitations exist (e.g., cloud contamination or weather constraints), neither episodic remote sensing images nor relatively static *in-situ* observations will allow us to fully understand the physical-biological coupling. In order to analyze and reveal the complex physical mechanisms from a hydrodynamic perspective, and to further understand the biogeochemical processes, the approach of three-dimensional physical-biological coupled model is employed, combined with the analysis of observational data in this dissertation.

Chapter 4

ON THE WINTER LUZON BLOOM

In this chapter, the winter bloom occurred in the Luzon Strait is chosen to be investigated with particular focus on the mesoscale processes on the week to month time scales. The January 2010 bloom is a typical scenario when compared with those instances from *Wang et al.* [2010] and *Tang et al.* [1999], which will be depicted in the following analysis. This chapter is organized as follows. In Section 4.1, the model configuration and remote sensing data used in this chapter are described. In Section 4.2, model outputs are presented and compared with remote sensing data as validation. In addition, a series of model results are shown, including horizontal distributions, vertical profiles, and wind-induced processes. In Section 4.3, a nutrient diagnostics method is employed to comprehensively analyze the mechanisms that are active in the LZB. To further discuss the mechanisms of subsurface upwelling, the vorticity equation is utilized to diagnose hydrodynamics of the system. At last, the conclusions and prospects are summarized in Section 4.4.

4.1 Model and Methods

4.1.1 Regional Ocean Modeling System (ROMS)

Regional Ocean Model System (ROMS) is a free-surface, hydrostatic ocean model solving the Reynolds-averaged Navier-Stokes (RANS) equations on topography-following coordinates [*Shchepetkin and McWilliams*, 2005]. ROMS solves the three-dimensional RANS equations with the Boussinesq approximation and hydrostatic approximation in Cartesian horizontal coordinates and sigma vertical coordinates. The RANS equations can be written as [*Haidvogel et al.*, 2008]:

$$\frac{\partial(H_z u)}{\partial t}+\frac{\partial(uH_z u)}{\partial x}+\frac{\partial(vH_z u)}{\partial y}+\frac{\partial(\omega H_z u)}{\partial s}-fH_z v=-\frac{H_z}{\rho_0}\frac{\partial p}{\partial x}-H_z g\frac{\partial \eta}{\partial x}-\frac{\partial}{\partial s}(K_M\frac{\partial u}{\partial s})+F_x, \tag{4-1}$$

$$\frac{\partial(H_z v)}{\partial t}+\frac{\partial(uH_z v)}{\partial x}+\frac{\partial(vH_z v)}{\partial y}+\frac{\partial(\omega H_z v)}{\partial s}+fH_z u=-\frac{H_z}{\rho_0}\frac{\partial p}{\partial y}-H_z g\frac{\partial \eta}{\partial y}-\frac{\partial}{\partial s}(K_M\frac{\partial v}{\partial s})+F_y, \tag{4-2}$$

$$0=-\frac{1}{\rho_0}\frac{\partial p}{\partial s}-\frac{g}{\rho_0}H_z\rho, \tag{4-3}$$

with the continuity equation and the nonlinear equation of state:

$$\frac{\partial \eta}{\partial t}+\frac{\partial(H_z u)}{\partial x}+\frac{\partial(H_z v)}{\partial y}+\frac{\partial(H_z \omega)}{\partial s}=0, \tag{4-4}$$

$$\rho=f(T,S,p), \tag{4-5}$$

and tracer equations in the conservative form [*Lu et al.*, 2017; *Shchepetkin and McWilliams*, 2005]:

$$\frac{\partial(H_z C)}{\partial t}+\frac{\partial(uH_z C)}{\partial x}+\frac{\partial(vH_z C)}{\partial y}+\frac{\partial(\omega H_z C)}{\partial s}=-\frac{\partial}{\partial s}(K_H\frac{\partial v}{\partial s})+F_T+S. \tag{4-6}$$

Here u, v and ω are the three components of velocity in x, y and s (vertical) directions. η is the free-surface elevation; H_z is the vertical thickness of each s-layer; p is pressure and ρ is the potential density while ρ_0 denotes reference density; f is the Coriolis parameter; g is the gravity acceleration; K_M and K_H are the eddy viscosity for momentum and eddy diffusivity for tracers, respectively; F_x and F_y are the horizontal viscosity and F_T is the horizontal diffusivity; S in equation (4-6) represents source or sink of the tracer C. The vertical turbulent mixing is closured by the K-profile parameterization (KPP) scheme [*William G Large et al.*, 1994b], the Mellor-Yamada Level 2.5 turbulent closure scheme [*George L. Mellor and Yamada*, 1982], or other integrated schemes.

4.1.2 TFOR-Fennel Model on Curvilinear Grid

The physical model was from the operational Taiwan Strait Nowcast\Forecast system (TFOR), which provides multi-purpose oceanic simulations [*Jiang et al.*, 2011; *Liao et al.*, 2013; *X Lin et al.*, 2016; *Lu et al.*, 2015; *Jia Wang et al.*, 2013]. Based on TFOR model, two SCS model systems are designed, with the emphasis on different physical setting and processes.

The orthogonal curvilinear grid of TFOR (Figure 4-1a) was centered in the Taiwan Strait, with a variable horizontal resolution ranging from 1.5 km in the Taiwan Strait and approximately 45 km at the open boundary. Although the TFOR system was not developed intended for the SCS study, the spatial resolution in the vicinity of LS was finer than 10 km and was adequate for the scope of this study. The model bathymetry was a combination of the ETOPO2v2 dataset and digitized depth data published by the China Maritime Safety Administration. A vertical topography-following S-coordinate was adopted with 30 σ-layers, which was derived by a stretching function of θ_s=3.0, θ_b=0.4 and h_c=10 m. In the open boundary, the boundary currents, surface elevation, temperature, and salinity were derived from the *My Ocean Project* (http://www.myocean.eu/) data. The Flather's boundary condition [*Flather*, 1987] and Chapman's boundary condition [*Chapman*, 1985] were applied for two-dimensional velocity and surface elevation, respectively. At surface, the daily atmospheric forcing data (i.e., wind stress, net heat flux and fresh water flux) used in this chapter were from the Weather Research and Forecasting model (WRF) operated in the Fujian Marine Forecasting Institute (http://www.fjmf.gov.cn/NumPrediction/NumericalPrediction.aspx, in Chinese). The mixing parameterization scheme used was the Mellor-Yamada's level 2.5 turbulence closure scheme [*Mellor and Yamada*, 1982]. Sensitivity tests suggested that tidal effects were not a significant contributor to the LZB, so the tidal forcing was excluded from the model. Monthly mean discharges from the major rivers were added to the domain as point sources of water and tracers, with the Cagayan River input specified by data from the SAGE River Discharge Database (http://www.sage.wisc.edu/riverdata/).

The biological model, on the other hand, was described in *Wang et al.* [2013], which was based on the nitrogen-based, nutrient-phytoplankton-zooplankton-detritus (NPZD) model by *Fennel et al.* [2006]. The model was comprised of nitrate (NO_3), ammonium (NH_4), large detritus, small detritus, phytoplankton, zooplankton and chlorophyll. The initial fields and boundary conditions for the biological tracers were derived from the World Ocean Atlas 2005 (WOA2005) database (http://www.nodc.noaa.gov/OC5/WOA05/pr_woa05.html). The detailed configuration and parameter values as well as the validation and skill assessment were discussed in [*X Lin et al.*, 2016] and *Wang et al.* [2013].

4.1.3 Remote Sensing Data

Daily Aqua MODIS level-3 chlorophyll (9 km resolution) and Terra MODIS level-3 SST (daytime, 4 km resolution) images for 28 January 2010 were obtained from the NASA Distributed Active Archive Center (DAAC, http://oceancolor.gsfc.nasa.gov/). Climatological January SST data (4 km resolution) was also obtained from the Aqua MODIS satellite level-3 products. The Mean

Dynamic Topography (MDT_CNES-CLS09, v1.1 version) altimeter product from 1993 to 2010 was produced by the *CLS* Space Oceanography Division (http://www.aviso.oceanobs.com/), while the gridded Absolute Dynamic Topography (ADT, 1/3° resolution) was from the Jason-2 satellite, which was averaged weekly from January 27 to February 2, 2010, and the climatological Sea Level Anomaly (SLA, 1/4° resolution) was produced by Ssalto/*Duacs* *(*http://www.aviso.oceanobs.com/duacs/*)*. Both categories of data were distributed by *Aviso* with support from the Centre National d'Etudes Spatiales *(Cnes). The climatological January mean ADT (MADT) was computed from MDT and the climatological January SLA was linearly interpolated to eliminate resolution differences. The SeaWinds scatterometer on the Quick Scatterometer (QuikSCAT) which had climatological averaged wind stress data for 2000-2007 (ftp://ftp.remss.com/qscat/bmaps_v04/, 1/4° resolution), was used to derive the wind stress curl near the LS.*

4.2 Results

4.2.1 Horizontal Distribution

The modeled general circulation pattern for January 2010 near the LS is shown in Figure 4-2b. Modeled sea surface temperature (SST) and sea surface chlorophyll (SSC) on January 28, 2010, are presented in Figure 4-2c and Figure 4-2f, respectively, along with the remote sensing data for January, 2010 (Figure 4-2a and Figure 4-2d) and in the climatological January (Figure 4-2b and Figure 4-2e), for comparison. In all scenarios, the Kuroshio bordered the eastern LS, which was characterized by SST over 27°C and was sustained by a high sea surface height (SSH) gradient. Among the three types of Kuroshio intrusion into SCS [*Nan et al.*, 2011], this scenario was likely to be looping path. The Kuroshio clearly veers into the SCS across the middle of the LS and exits the SCS at the northern side of the LS, forming an anti-cyclonic Kuroshio loop. In winter time, the Kuroshio occasionally intrudes into the SCS and forms such typical looping structure [*Wu and Chiang*, 2007; *Caruso et al.*, 2006]. The presence of a warm-core eddy (marked "*W*" in Figure 4-2c) located at ~117°E, 20.5°N in the model can be observed from the high SSH and low SSC. Another significant feature shown in Figure 4-2a and Figure 4-2c was the low SSH, low SST, and high productivity region of western LI. *Shang et al.* [2012] identified this phenomenon as cold-core eddy activity. In the model, the center of this cold-core eddy appeared at 118.6°E, 18.2°N (Labeled "*C*" in Figure 4-2c), with a warmer SST center relative to the observations. To the west of LI, the LCC, with higher temperature waters that were tracked back to the interior of the SCS, flowed northward to ~20°N [*Shaw et al.*, 1996]. Constrained by the cold eddy, the LCC flowed northward and encountered the Kuroshio loop current, where a thermal front was observed on both sides of warm LCC water (Figure 4-2a). The modeled LCC, however, turned westward and penetrated back into the SCS, although a discernible thermal front was still apparent (Figure 4-2c). Excluding the warm-core eddy, the modeled SSC, SST, and SSH patterns, especially the LCC and the cold-core eddy, matched the climatological scenario quite well (Figure 4-2b and Figure 4-2e).

While the model does not completely resolve the precise location and intensity (e.g., modeled SSC values were much higher than the remote sensing values) of the LZB, the key features of the bloom patch were captured. For example, the area with high productivity formed an inverted-V shape, two-wing structure to the northwest of

LI, which was consistent with the patterns found in other studies [*Peñaflor et al.,* 2007; *Shang et al.,* 2012]. The modeled intensity of the bloom was exaggerated, while the near-shore wing (to the north of LI) and the offshore wing (~200 km northwest of LI) were separately discernable. Moreover, the position of the bloom patch was located offshore to the north of the LCC. This feature implied that the LCC may have played a role in the LZB. The underlying implication of this will be discussed in the next section.

4.2.2 Vertical Distribution

Figure 4-3 shows the vertical profiles of temperature, salinity, nitrate nutrient and chlorophyll on a section along 120°E (see Figure 4-2f for location) for validation. The cross marks above the profiles show approximate positions of corresponding stations from *Shang et al.,* [2012]. The vertical temperature structures in observation and in the model were both well stratified, except within the surface mixing layer (~50 m deep). On the southern portion of the section, low salinity (fresher than 34.4) and high temperature (>25°C) water occurred from surface down to 50 m which originated from the interior of the SCS and was advected by the LCC. When comparing the northern and southern portions of the section, the isotherms in the south were uplifted ~50 m relative to the north. This pattern was inconsistent with the observations. In the salinity profile, high salinity water from the intrusive Kuroshio was as deep as 500 m. This signal was also clear in the observation, although the observational position was to the north of station E402. The small portion of high salinity water in the upper 100 m layer near 19.7°N was associated with an offshore jet. *Shang et al.,* [2012] revealed two upward doming isotherms. In the model profiles, two domes were also discernable. One was located to the south of Kuroshio high salinity water, while the other was further south near station E405. The isotherms dome beneath the thermocline extended deeper than 500 m. In summary, the model was not completely resolve the vertical structure of temperature and salinity (e.g., the strong thermocline above 20°C isotherm), partially because of the limited vertical resolution; however, the model did capture the north-south contrast pattern in the LS and the two upward motions.

The vertical structure of NO_3 along the section (dot line in Figure 4-2f) near the LS was compared to that from *Chen et al.* [2006] (their figure 7). The modeled regression curve of temperature versus nitrate showed almost identical slopes and intercepts values (Figure 4-3e) with the observation. The modeled and observed high correlation coefficient (0.98 and 0.93) means that the variation of nitrate was highly related to that of temperature, therefore the physical modeling performance could almost decide the biological modeling nutrient estimation. At the two doming sites, the nitrate isolines showed significant uplift (Figure 4-3c). High productivity appeared on the north side of the jet at ~19.7° N (Figure 4-3d). The bloom patch was found at upper ~100 m layer and had a horizontal width of ~100 km. Generally, modeled nitrate, which is an essential biological parameter in nitrate-based system, agreed with the observations reported by *Chen et al.* [2006] reasonably.

4.2.3 Wind and Mixing

Figure 4-4a and Figure 4-4b are time series of spatially averaged wind stress. As seen from the expanded time series of wind stress magnitude, from the 14th to the 31st of January, the wind strengthened and reached a peak value of approximately 0.37 Pa and persisted for more than half a month. Historical documents showed that the wind speed during the winter northeast monsoon in the SCS averaged approximately 9 m s^{-1}

(~0.26 Pa) [*Wyrtki*, 1961]. The wind stress peak on January 17th was approximately 1.4 times the mean value. Leading up to the January 17th peak, the local winds shifted to a primarily northerly direction as it strengthened (see Figure 4-4c). From January 31st onwards, the wind weakened and switched to an easterly wind (Figure 4-4d). Northerly winds were upwelling-favorable to the west of LI. The multiple cores of wind curl (e.g., the two positive centers near the south cape of Taiwan and west of LI, Figure 4-2e), were caused by the orographic blocking effect of the mountains [*Wang et al.*, 2008]. Such oscillations of the local wind will inevitably drive short temporal scale processes, e.g., intensification of wind-induced mixing or wind-induced upwelling, especially within a Rossby radius of deformation of LI and the Taiwan coast, which was approximately 50 km in the first baroclinic mode [*Chelton et al.*, 1998].

In order to analyze the time variations of wind-induced processes, a 5-day moving average of the wind stress (Pa), mixed layer depth (MLD, unit: m), surface NO_3 (mmol m^{-3}) and SSC concentration (mg m^{-3}) were spatially averaged within Box M (see Figure 4-2f). Box M was deliberately selected to cover the dynamic core of the bloom patch, especially during its rapid growth. The time series are presented in Figure 4-5. Meanwhile, Figure 4-6 shows the time-depth maps of temperature, salinity, vertical velocity, NO_3 and phytoplankton, also averaged within Box M, as well as the time series of spatially averaged wind stress, vectors and surface phytoplankton concentration. In this section, the variability from January to mid-February was focused on.

Following the wind intensification, MLD deepened from 40 m to a maximum of ~73 m (Figure 4-5). The deepened MLD could also be inferred from the temperature and salinity profiles (Figure 4-6a and Figure 4-6b). Output from the NASA Ocean Biogeochemical Model (NOBM) showed that the MLD was deeper than 80 m in winters from 1998 to 2007 (http://gdata1.sci.gsfc.nasa.gov/daac-bin/G3/gui.cgi?instance_id=ocean_model_day, *Acker and Leptoukh* [2007]). Forced by strong winds, chlorophyll concentration levels slightly depressed to approximately 0.25 mg m^{-3} (Figure 4-5). After peaking on the 23rd of January, NO_3 concentration started to decrease while it was taken up by the phytoplankton. Phytoplankton peaked on the 2nd of February with a maximum of ~0.7 mmol N m^{-3} (Figure 4-6e). Temperature, salinity, and nutrient profiles also showed isoline uplift after the wind intensification. For example, the 34.45 isohaline rose approximately 50 m between the 25th and the 31st of January (Figure 4-6b).

In addition to the mixing, it was clear that strong, positive vertical motion appeared after the 22nd of January, reaching a high value of ~1.5×10^{-5} m s^{-1} (equivalent to 1.3 m d^{-1}, see Figure 4-6c). This indicated that vertical motion also played a positive role in the nutrient isoline uplift. The generating mechanism of vertical velocity is discussed in next section.

4.3 Analysis and Discussion

From the results in Section 3, the occurrence of the LZB in the simulation in January 2010 could be identified from high SSC (Figure 4-2f) distributions, which was consistence with both remote sensing results and the literature [*Shang et al.*, 2012]. In general, the bloom patch had an inverted-V structure that extended for approximately 200 kilometers. The location of the offshore bloom patch was among several major mesoscale processes, i.e., the Kuroshio loop current, a warm-core eddy, a cold-core eddy, and the LCC. Vertically, high phytoplankton extended down as deep as ~50 m, reaching its maximum average value of ~0.2 mmol N m^{-3} (Figure 4-6e).

The eddy pumping mechanism was employed to explain this phenomenon [*Shang et al.*, 2012]; however, the extent of the bloom patch was much larger than the eddy center region and located further north beyond the eddy center. This implied that mechanisms other than eddy pumping might play essential roles in the dynamics of the bloom patch.

4.3.1 Ecosystem Responses to the Wind

From the model outputs within the upper 50 m layer of Box M (Figure 4-2f), phytoplankton was majorly (~77%) a result of local growth rather than from exterior inputs via horizontal advection. To achieve a better understanding of the nutrient sources sustaining the bloom patch, the nutrient balance in the tracer equation was diagnosed from the model outputs. Diagnostically, the temporal variation of nutrient concentration was decomposed into the terms presented in equation (4-7) [*Shchepetkin and McWilliams*, 2005; *Wang et al.*, 2013]:

$$\frac{\partial[NO_3]}{\partial t} = \underbrace{\underbrace{-\left[\frac{\partial(u\cdot[NO_3])}{\partial x}+\frac{\partial(v\cdot[NO_3])}{\partial y}\right]}_{\text{HAdv}}\underbrace{-\left[\frac{\partial(w\cdot[NO_3])}{\partial z}\right]}_{\text{VAdv}}\underbrace{+(k_v\cdot\frac{\partial[NO_3]^2}{\partial z^2})}_{\text{VDif}}}_{\textbf{Physical Terms}}\underbrace{+\underbrace{(-L_{NO3}\cdot[PHYTO])}_{\text{uptake}}+\underbrace{(L_{nitri}\cdot[NH_4])}_{\text{nitrification}}}_{\textbf{Biological/Chemical Terms}} \tag{4-7}$$

where u, v, w are velocity components in x-, y- and z-direction of Cartesian coordinates, and k_v is the vertical diffusion coefficient. L_{NO3} is uptake rate and L_{nitri} is nitrification rate. [$PHYTO$] and [NH_4] represent the concentration of phytoplankton and ammonia, respectively. The first three right-hand side terms are physical terms and last two are biological/chemical terms. The physical terms included the horizontal advection term (HAdv), vertical advection term (VAdv), and vertical diffusion term

(VDif). The horizontal diffusion term is two-orders of magnitude smaller than these other terms, and therefore was neglected in equation (4-7). The biological/chemical terms included phytoplankton uptake and ammonia nitrification. Time-depth maps of the spatially averaged (within Box M) nitrate budgets terms are presented in Figure 4-7. The net biological/chemical change (Figure 4-7b) showed negative values in the upper euphotic layer (~50 m), which was principally dominated by the phytoplankton uptake term. VDif was dominant within surface 40 m layer, with a large value exceeding 2 mmol m^{-3}. A noticeable subsurface VAdv center was seen in Figure 4-7e, with a maximum at ~45 m. The VDif effect was enhanced and confined to the shallow surface layer (~40 m, >2.0 mmol m^{-3}). The HAdv was relatively small (<0.7 mmol m^{-3}) over the entire 100 m layer. In summary, the biological/chemical processes exhausted nutrients in the upper euphotic layer, especially after 28th January. Vertical diffusion replenished the nutrients in the upper layer, while vertical advection tended to supply nutrients to the subsurface layer. From the simulations, it was found that the LZB occurred in the relaxation period just after the wind intensification. The onset of the bloom followed the weakening of the wind. It was shown that the onset of phytoplankton bloom occurred when MLD depth started to shallow, because weakening mixing allowed phytoplankton to accumulate in the surface water [*Townsend et al.*, 1992; *Shiozaki et al.*, 2013]. Notably, as seen in Figure 4-7f, wind-induced vertical mixing was the major contributor of nutrients to the upper 40 m of the water column. Vertical mixing in the surface layer began to intensify on January 15th as seen in Figure 4-5 and Figure 4-7f. The positive contribution from VDif intensified because of the strengthening of the wind stress (Figure 4-7f). Both of above evidence suggested that wind-induced mixing variability in the upper layer was responsible for the bloom.

The wind-induced processes can only explain the onset time of the LZB. Because intensified wind was at larger spatial scales than the LZB, it failed to predict the distinctive spatial structure of the LZB. If strengthened mixing was the only mechanism controlling the LZB, the extent of the bloom patch would be larger. Without deep compensation, nutrients in the shallow layer would be rapidly depleted; therefore, nutrients were most likely upwelled from the deeper layer (~90 m) into the upper ~30 m layer, where the VDif came into play. Hence, the important role of subsurface upwelling on the LZB was highlighted. The mechanism of the LZB was a two-stage model in which both wind-induced mixing and subsurface upwelling played a significant role.

In order to examine the practicality of the method in other bloom cases, the depth-time maps beyond January were also presented (Figure 4-6). Three bloom cases were identified (marked a, b and c in Figure 4-6e). Each bloom occurred during the relaxation time of the wind and initiate when wind stress starts to weaken (Figure 4-6f). Case a was the bloom case discussed above. The contrasts among the three cases further support the two-stage mechanism. In Case b, strengthened wind (middle February, Figure 4-6f) was not sustained by subsurface upwelling, so the intensity of Case b was relatively weak. From mid-February to mid-March, because of negative vertical velocity, nutrients in the upper water were limited and did not allow for a strong bloom. In contrast, although the wind stress was not as strong in Case c as that in Case a and the wind duration was shorter, the intensity of the phytoplankton bloom was stronger than that in Case a because of intense subsurface upwelling.

4.3.2 Mechanisms of Vertical Velocity

Positive vertical velocity persisted from January 22nd to the end of January, with a maximum value of 1.5×10^{-5} m s^{-1} (or 1.3 m d^{-1}, Figure 4-6c). In regard to the mechanism of subsurface nutrient resupply, Ekman pumping by wind stress curl may have worked to upwell water from deeper layers into the mixed layer [*Wang et al.*, 2010]. The magnitude of the vertical velocity, w_e, derived from the Ekman pumping was only ~5 m d^{-1} [$w_e = -curl(\tau)/\rho_w f$, where $curl(\tau)$ is the wind stress curl, ρ_w is the density of sea water and f is Coriolis parameter]; however, a snapshot of the modeled vertical velocity field at 50 m depth showed that the magnitude could be as large as ~10 m d^{-1} (Figure 4-8a). Moreover, the wind-induced frictional effects were expected to be confined to the shallower Ekman layer. In addition, the LZB presented a distinct spatial pattern, which did not coincide with the positive Ekman pumping center (Figure 4-2e and Figure 4-2f).

The dynamics in the vicinity of the LS were characterized by high relative vorticity (RV, shown in Figure 4-9). The magnitude of the local Coriolis parameter was ~4×10^{-5} s^{-1}, which gave a Rossby number (RV/f) of ~0.25; therefore, the dynamics may have been in the nonlinear regime. To fully analyze the dynamic mechanisms of vertical velocity, the equation described by *Arthur* [1965] was also employed, which combined the vorticity equation with the continuity equation. Assuming the vertical velocity at the free surface was zero, the vertically integrated equation could be written as equation (4-8), which gave the vertical velocity at depth z when neglecting the beta effect term, baroclinic term and vortex tilting term:

$$w(z) = \underbrace{-\int_z^{\eta} \frac{1}{(\zeta+f)} \frac{\partial \zeta}{\partial t} dz}_{\text{WT}} \underbrace{- \int_z^{\eta} \frac{1}{(\zeta+f)} \vec{v} \cdot \nabla \zeta dz}_{\text{WA}} + \underbrace{\int_z^{\eta} \frac{1}{(\zeta+f)} A_v \frac{\partial^2 \zeta}{\partial z^2} dz}_{\text{WF}}, \qquad (4\text{-}8)$$

where ζ is the vertical component of RV:

$$\zeta = \frac{\partial v}{\partial x} - \frac{\partial u}{\partial y}, \tag{4-9}$$

In equation (4-8), the vertical velocity can be decomposed into three terms: the temporal derivative vorticity term (WT), vorticity advection term (WA, and when in combination with WT, total derivative term, WAT) and frictional term (WF). In the calculation, a temporal backward difference (one hour backward) and spatial central difference were utilized, and linear interpolation was used to make a rectilinear grid with a spatial resolution of 0.05° from the model's curved grid. In the vertical, linear interpolation was also used to compute vorticity and all other variables to the depth points with a vertical resolution of 5 m.

Figure 4-8 depicts a comparison between the vertical velocity derived from model outputs and calculated from equation (4-8). This comparison showed that the modeled and theoretical vertical velocities were very similar in spatial pattern. At 50 m, the maximum (~10 m d^{-1}) appeared outside the warm-core eddy with a filament-like, submesoscale structure. Observational and modeling studies, such as those in *Klein and Lapeyre* [2009], found similar spatial structures.

In order to present more general temporal variations, using the same technique, each term of the vertical velocity was averaged within Box S in Figure 4-2f. Box S was chosen because the vertical velocity field within Box S was largely responsible for the subsurface VAdv center. The time-series from January 25th to the 31st are shown in Figure 4-10. In Figure 4-10, the modeled and theoretical vertical velocities agreed well with each other (temporal variability, mean value, and standard deviation). The peak value of 4 m d^{-1} appeared on January 30th. In equation (4-8), WA was the most important contributor to the vertical velocity, as seen in Figure 4-10, while averaged WF and WT are lower in magnitude.

The vorticity advection induced strong vertical motion in the northern and northwestern portion of the cold eddy (labeled "*C*" in Figure 4-9). High lateral RV gradient regions coincided with large vertical velocity, implying that there were contributions from the WA. Along a stream function line of the offshore LCC, the RV changed from large positive values to negative values, which resulted in positive vertical velocity, and vice versa.

When spatially averaged, the WT possessed large variability. Calculation of the WT term was sensitive to the temporal interval. When calculated from daily output data, the contribution of WT was completely different (not shown in figures). In the de-tided model, the only daily varying forcing was the surface wind forcing; hence, the temporal variability of the RV field could be explained by adjustments driven by variable winds. Literature also shows that time varying wind will induce time-dependent motions [*D'Asaro*, 1985].

In summary, studying the hydrodynamics from equation (4-8) showed that vorticity advection played a dominant role in the vertical velocity, while WT and WF had less impact. Although vertical velocity calculated from equation (4-8) agreed well with the vertical velocity from the model, inconsistencies occurred in the vertical velocity time series (Figure 4-10). The reasons for the inconsistencies may be because of the following reasons: (1) Computational bias. In the calculation, numerical interpolation methods were applied, which can degrade the signal; (2) Ignored terms, i.e., the vortex tiling term, beta effect term, and baroclinic term, might be important in certain conditions. These may have resulted in an accumulation of computational error.

From the results discussed above, the WA term, which arose from the nonlinear terms in the primitive equations, played the dominant role in driving vertical velocity. Thus, the dynamics of the RV field and flow patterns were the key mechanism of subsurface upwelling. The plane view of the RV presented a complex structure (Figure 4-9). In the north, interaction of the Kuroshio and the warm-core eddy resulted in a filamentary structure. The warm-core eddy deformed into a narrow filament, which generates another smaller eddy. Meanwhile, high RV differences emerged across the strong Kuroshio front. In the south, a negative RV region existed on the north periphery of the cold-core eddy, which resulted from flow shear. An offshore jet, although smaller in scale, interacted with the ambient circulation and modified the local circulation when flowing offshore. This offshore jet penetrated from the positive RV to the negative RV region and generated high vertical velocity. In summary, vorticity advection resulted from the interaction between the offshore jet and the ambient circulation.

4.4 Summary

The dynamic mechanism of the LZB was studied with a 3-dimensional coupled physical-biological model. The mechanism of the LZB was a two-stage process. Wind-induced mixing stirred subsurface nutrients to surface, while subsurface upwelling maintained nutrient levels from below. Nutrient supply from vertical mixing was confined to the ~40 m surface layer, while subsurface upwelling advected nutrients from below the mixed layer, which was centered at ~45 m and below. From the hydrodynamic diagnostics, it was found that the main contribution to subsurface upwelling was from vorticity advection (WA), while the temporal variability of vorticity (WT) and the friction term (WF) were smaller. The magnitude of the vertical velocity could be as large as ~10 m d^{-1}. When a spatial average was taken, the magnitude of the vertical velocity, which resulted from the vorticity advection term (WA), was on the order of ~2 m d^{-1}, which approximated the value of modeled vertical velocity. The vorticity advection resulted from an offshore jet's interaction with the RV field determined from the ambient circulation.

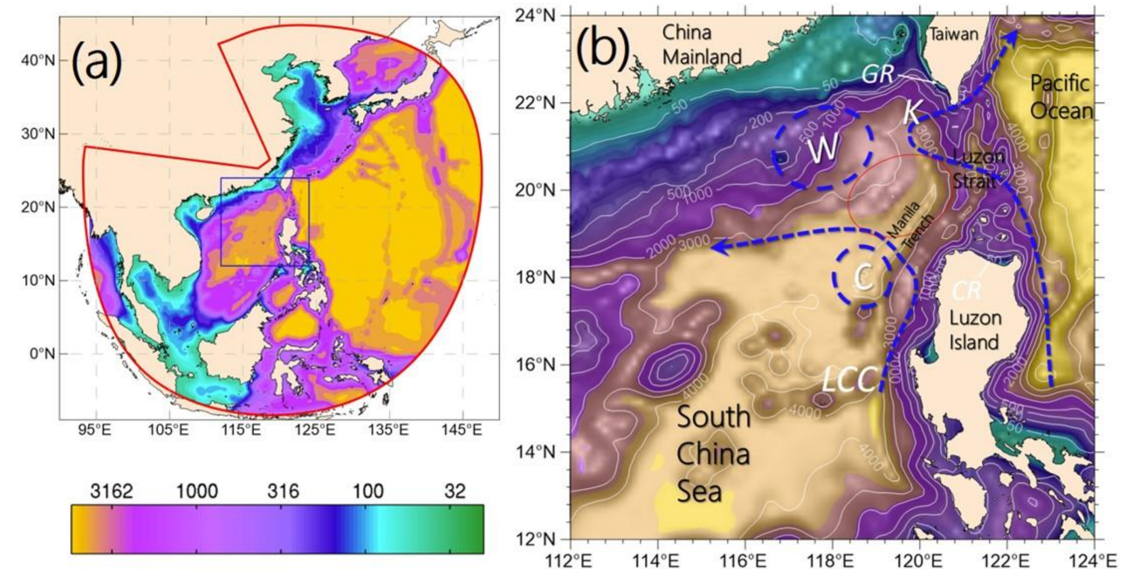

Figure 4-1 (a) Model domain within bold red lines. Blue box is the region of subfigure (b). (b) The model bathymetry (shading map, unit: meter) of Northern South China Sea in the vicinity of Luzon Strait. White contours indicate the isobaths of 50, 200, 500, 1000, 2000, 3000 and 4000 m. Blue bold dash lines show the major dynamic processes near Luzon Strait in January 2010, while white italic abbreviations mean: W: warm-core eddy; K: Kuroshio; CR: Mouth of Cagayan River; GR: Mouth of Gaoping River; LCC: Luzon Coastal Current; C: Cold-core eddy. Red circle denotes the approximate extent of the Luzon Bloom found in previous studies.

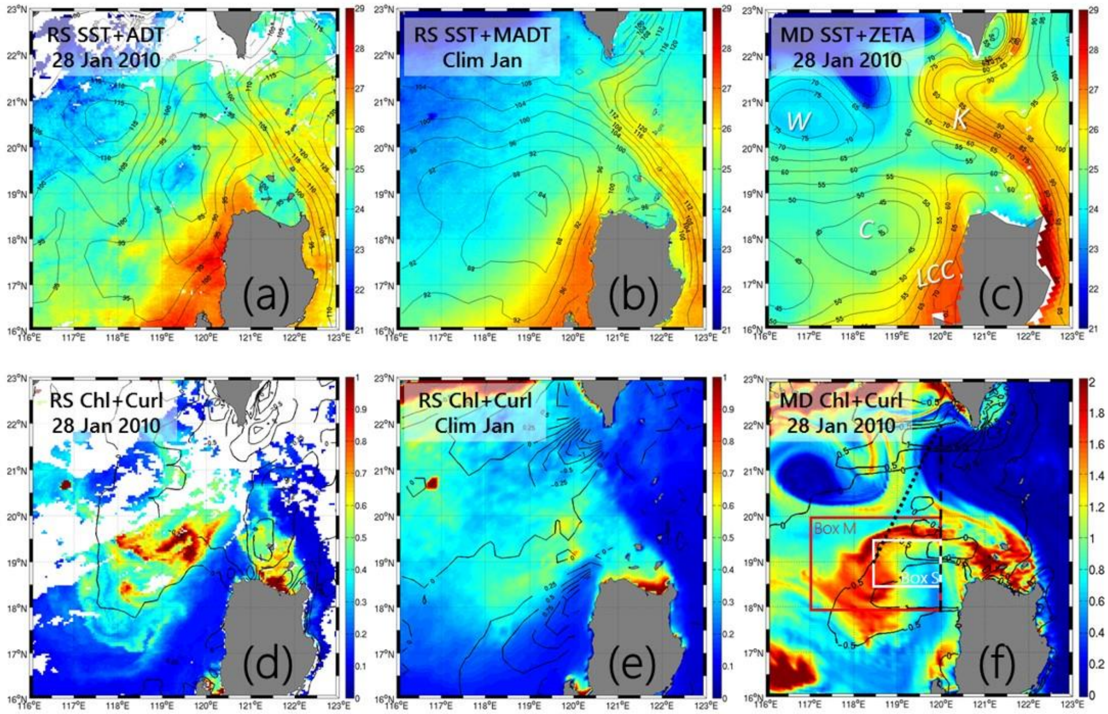

Figure 4-2 Upper row: (a-c): plane view of SST (color, unit: °C) with contours of the associated sea surface height (ADT from remote sensing data and surface elevation from the model). Lower row (d-f): SSC concentration (color, unit: mg m^{-3}) with contours of the associated wind curl (unit: $\times 10^{-6}$ s^{-1}). (a) SST on January 28th with weekly mean ADT contours (unit: cm) from 27th January to 2nd February, 2010. (b) SST and mean ADT contours from climatological January. (c) Model SST with contours of SSH (unit: cm); (d) MODIS SSC concentration and contours of QuikSCAT wind curl on January 28th, 2010. (e) Same as d, but for climatological January. (f) Modeled SSC and contours of wind stress curl on January 28th. Box M (in red) and Box S (in white) are the areas over which spatial averaging is performed in the following figures, while the dashed line denotes the position of the section presented in Figure 3. Dotted line is the location of the section from *Chen et al.* [2006]. White italic abbreviations in (c) have the same meaning with those in Figure 1b.

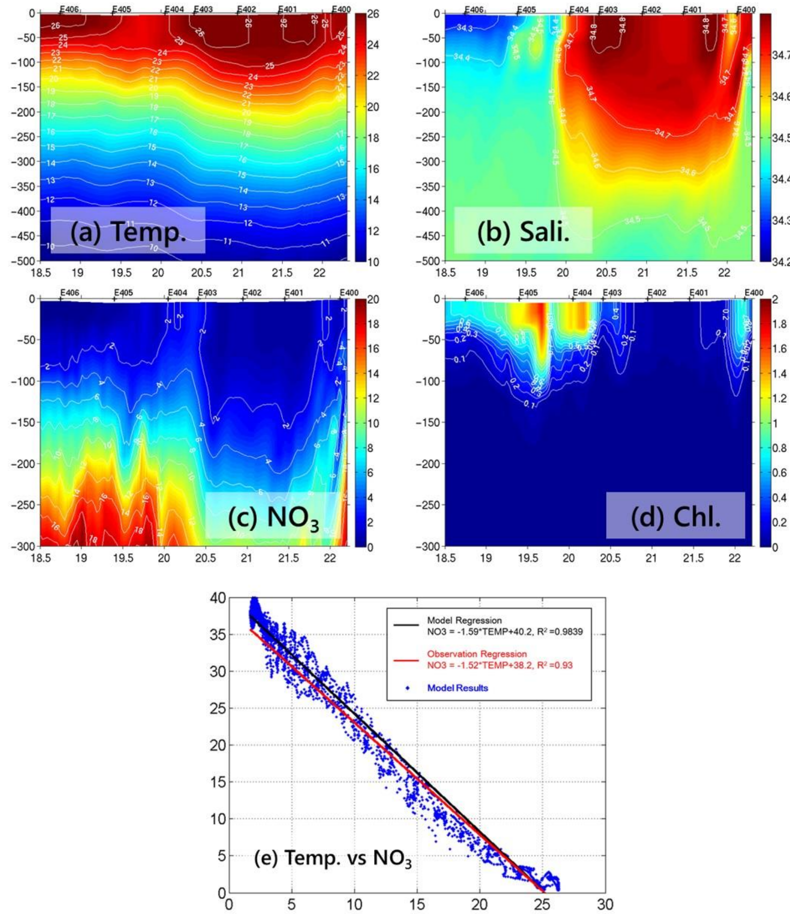

Figure 4-3 Model validation: Modeled daily-averaged temperature (a, unit: °C), salinity (b), nitrate concentration (c, unit: mmol m^{-3}) and chlorophyll concentration (d, unit: mg m^{-3}) profiles for the along transect 120°E (refer to dash line in Figure 4-2f) on January 28th, 2010. The cross marks above indicate the observation stations of *Shang et al.*, [2012] (see their figure 6c for observed profile plots). (e) Blue dots show modeled temperature versus NO_3 plot at section near LS (see dot line in Figure 4-2f) in January. Black line is the regression curve of modeled data, while red line shows the observed relation from *Chen et al.* [2006] (see their figure 7).

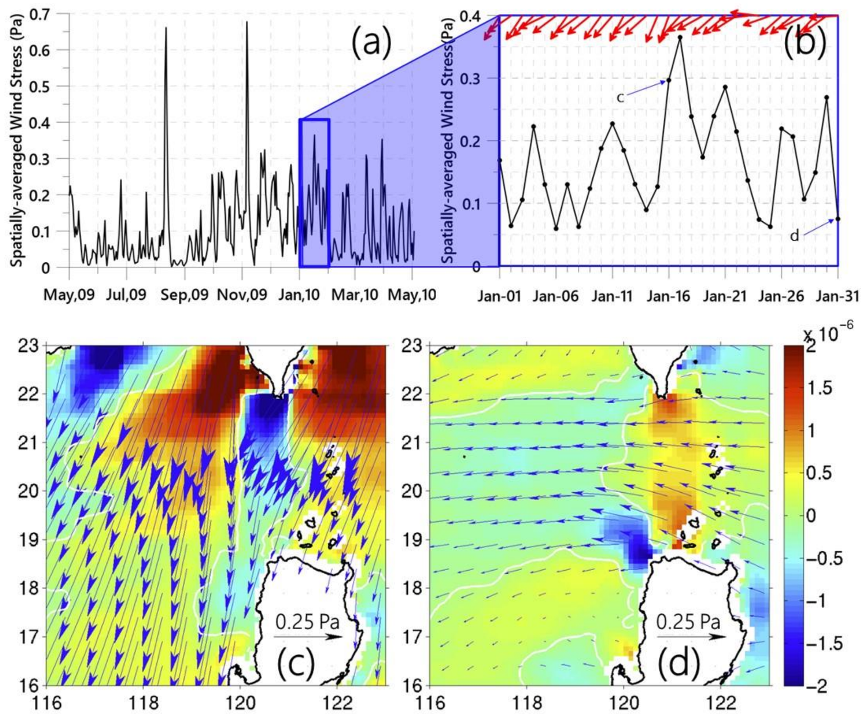

Figure 4-4 Winds near the LS. (a) Wind stress spatially averaged within the region in (c) and (d). (b) expanded time series of wind stress for January, 2010. Red vectors above are corresponding unit vectors of wind stress showing wind direction. In (c) and (d), two distinctive wind patterns near the LS for 16th January and 31st January, respectively. Color shading in these maps is the wind stress curl (Pa m^{-1}) with the white contours showing the zero values.

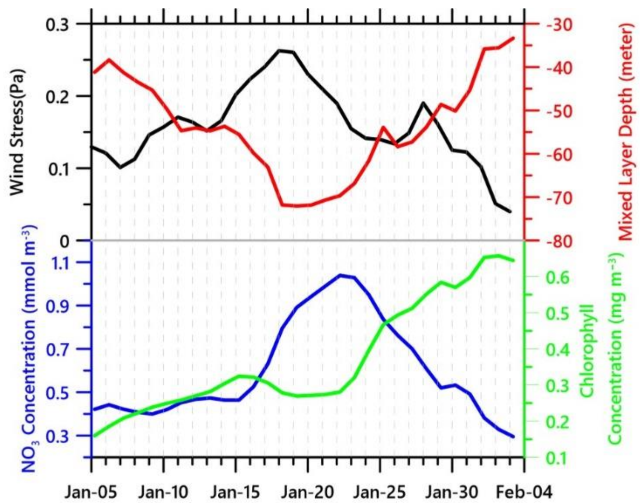

Figure 4-5 Time series, which are spatial averaged over Box M (shown in Figure 4-2f) in 2010, of: Black: 5-day moving averaged wind stress (Pa); Red: Mixed Layer Depth (meter); Blue: Surface NO_3 concentration (mmol m^{-3}); Green: SSC concentration (mg m^{-3}).

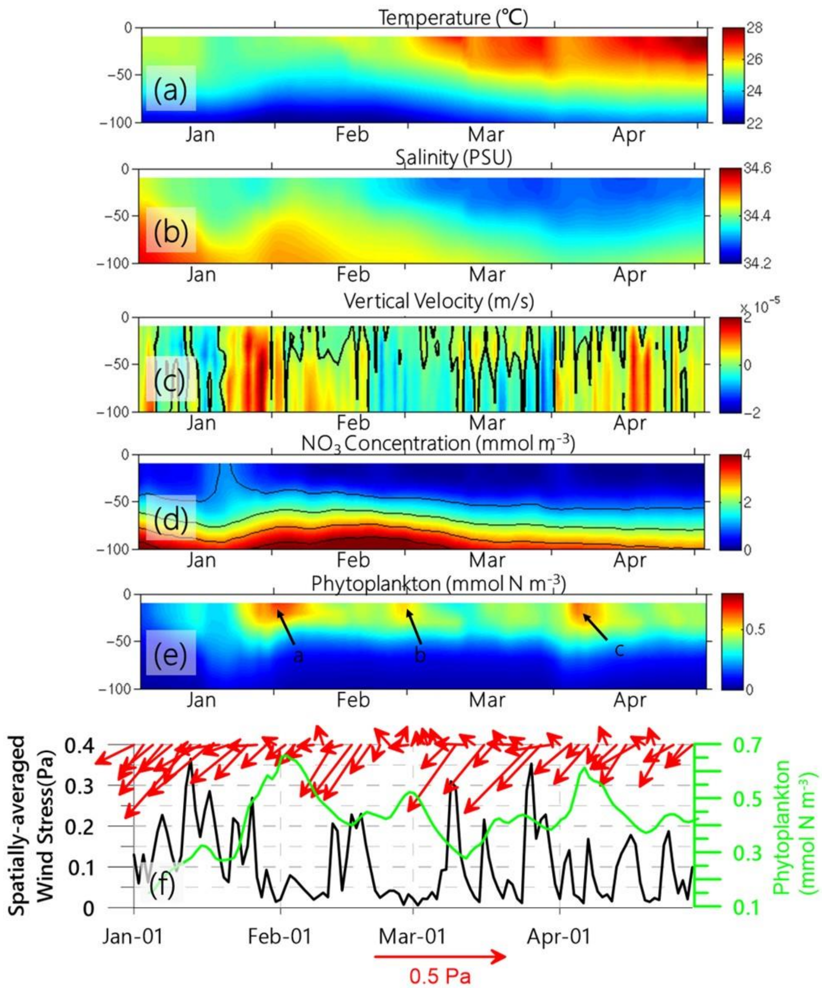

Figure 4-6 Vertical time-depth series averaged over Box M. From top to bottom the panels are temperature, salinity, vertical velocity, NO_3 (in which the contours are values with an interval of 1 mmol m^{-3}) and phytoplankton, respectively. (f) Spatially-averaged wind stress (Pa, black curve), surface phytoplankton concentration (mmol N m^{-3}, green curve) and wind vectors (red arrows).

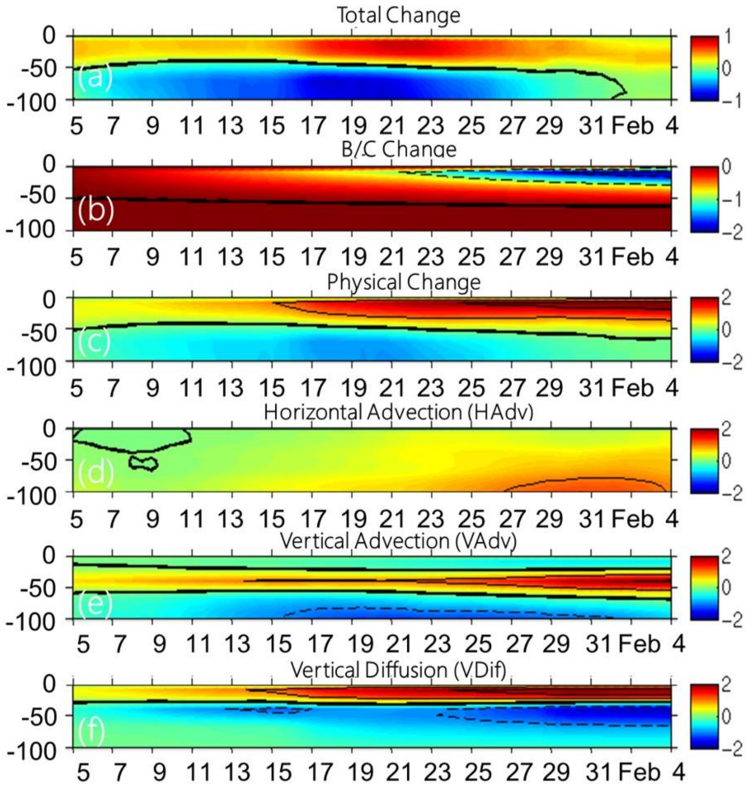

Figure 4-7 Spatially averaged (over Box M) diagnostic profiles of the terms cumulatively contributing to NO_3 in the upper 100 m of the water column. All terms are integrated over time. Black bold lines indicate zero values. The solid (positive value) and dash (negative value) lines in each subfigure are with an interval of 1.0. Unit for all terms is mmol m^{-3}. (a) Total change rate of NO_3; (b) Contribution from the biological/chemical processes in model (i.e. uptake and nitrification); (c) Total contribution from the physical processes (i.e. vertical and horizontal advection, vertical and horizontal diffusion, while the horizontal diffusion is significantly lower than other three); (d), (e) and (f) horizontal advection, vertical advection and vertical diffusion, respectively.

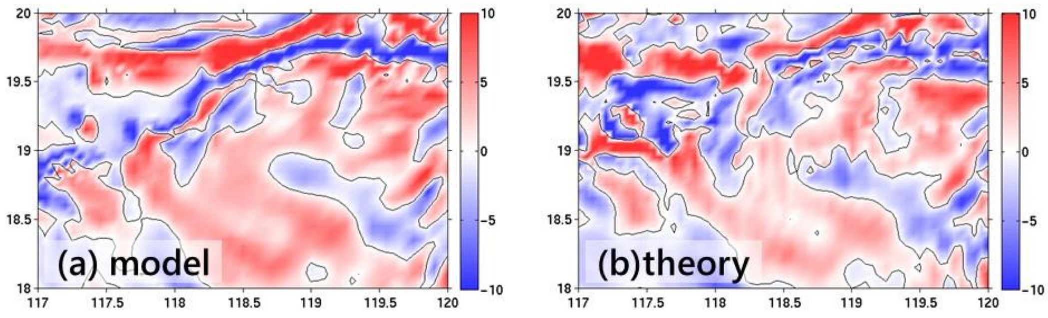

Figure 4-8 Vertical velocity (unit: m d^{-1}) at 50 m depth from (a): model outputs and (b): that calculated from equation (4-8). Both are snapshots at 9:00, January 28th, 2010. Black contours are zero values.

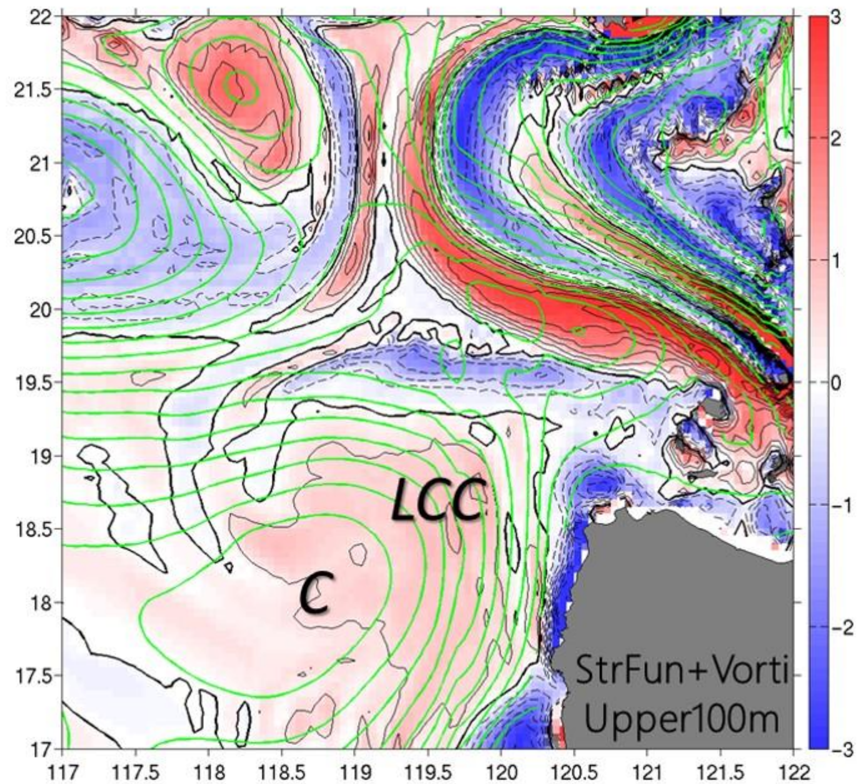

Figure 4-9 Daily mean upper 100 m averaged relative vorticity (RV) near the LS on January 28th, 2010 (shading map, unit: 10^{-5} s^{-1}). The black contours indicate isolines of zero RV and the green contours are the stream function integrated over the upper 100 m (unit: m^2 s^{-1}, with a contour interval of 1.0 m^2 s^{-1}). Black italic abbreviations have the same meaning as those in Figure 4-1b.

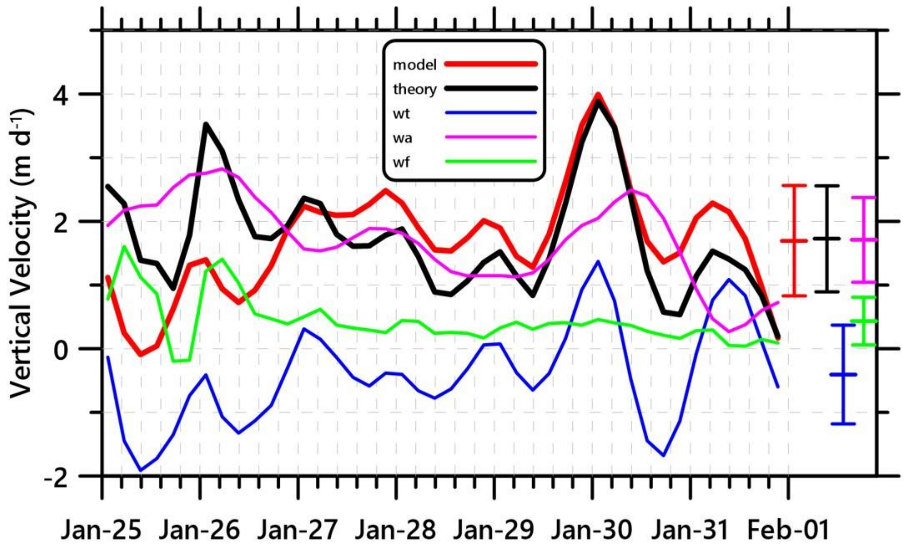

Figure 4-10 Time-series of spatial averaged vertical velocity at 50 m depth within Box S from the model output (red bold) and calculated from equation (4-8) (black bold). The other curves are the contributions to the vertical velocity from: the temporal derivative of vorticity (WT, blue line), vorticity advection (WA, magenta) and friction (WF, green). Corresponding averaged values and error bars (± one standard deviation) are shown on the right.

Chapter 5

ON THE VERTICAL MOTION AT SEATS STATION

Before the case study of the VBUS system, a one-dimensional (1D) model was applied in an additional case study to investigate the diffusion-advection control of the vertical variability in the northern SCS. The 1D model also functioned as a simplified model to tune various parameters of the biological module which will be detailed in Section 6.1.3. With a 3D model, the tuning process could be computationally unaffordable. The objective of this chapter is to study the behavior of the upper ocean thermal structure above intermediate layer (1000 m) in a 1D context. Especially, focuses are on the processes which can induce vertical motion, i.e., Ekman pumping, eddy pumping and background circulation. The ultimate goal is to achieve better understanding of the processes that control the vertical thermal variability at the SEATS station, which can be further applied in 1D physical-biological coupled model to tune tens of parameters in ecosystem module.

This chapter is organized as follows. The environmental background of SEATS station (which will be defined later) and the historical application of 1D model are introduced in Section 5.1. The 1D-model configuration, utilized observation data and sensitivity experiments design are outlined in Section 5.2. And in Section 5.3, analysis of the observation data, as well as model results are shown. Furthermore, the model results are interpreted, and the underlying physics are discussed. At last, summaries are given in Section 5.4.

5.1 Introduction

At the SouthEast Asian Time-series Study (SEATS, diamond in Figure 5-1) station, where the properties are representative for the sea water of the central SCS within the basin interior [*Wong et al.*, 2007]. Previously, multiple oceanic variables have been studied, including temperature, salinity, nutrients [*Wong et al.*, 2007], chlorophyll [*K K Liu et al.*, 2013b], and primary production [*C M Tseng et al.*, 2009].

One-dimensional (1D) oceanic models are implemental to study the vertical thermal structure. *Munk* [1966] fitted the vertical profiles of temperature and salinity based on a simple advection-diffusion balance, suggesting the practicability of a 1D model. Recently, although the advances in computer technology have been making three-dimensional ocean modeling more and more affordable, 1D models still show its merits in planktonic ecosystem modeling attributing to its simpler physics and shorter computational time [*Q P Li et al.*, 2015; *Sasai et al.*, 2016; *Shigemitsu et al.*, 2012], specifically in parameter-tuning process. Given the relatively weak horizontal advection condition at SEATS, the application of 1D model was justified by *Q P Li et al.* [2015].

Conventional 1D models simulate the vertical turbulent mixing in the oceanic mixed layer(s) [*George L Mellor*, 2001]. However, in 1D context, due to the absence of horizontal divergence, no vertical motions can be resolved essentially. Practically, the effects from vertical advection were generally omitted [*Hood et al.*, 2001; *Jin et al.*, 2006; *Lévy et al.*, 1998; *Sasai et al.*, 2016]. The omitted advection resulted in building up of near-surface momentum, and hence exaggeratively deepened the mixed layer and cooled the surface temperature [*George L Mellor*, 2001]. To balance the over-mixed ocean structure, additional numerical methods, e.g., relaxation toward observational data [*Chifflet et al.*, 2001], or adding sink terms in the momentum equations [*George L Mellor*, 2001], are required. Actually, the intensive upwelling at the SEATS station suppresses the mixed layer [*Wong et al.*, 2007], resulting in shallower mixed layer depth. Following the work of *Chifflet et al.* [2001], *Li et al.* [2015] artificially incorporated the vertical velocity driven by Ekman pumping, demonstrating that vertical motion can be prescribed and included in 1D model. However, it is arguable that whether Ekman pumping is the major contributor to the vertical motion, especially beneath the upper mixed layer [*Wong et al.*, 2007]. At depth, other processes may dominate the vertical motion, e.g., eddy pumping or quasi-geostrophic [*Pascual et al.*, 2015]. Thus, in this chapter, aside from Ekman pumping, vertical motion induced by mesoscale eddy activity and the background upwelling-are also considered.

5.2 Model Configuration and Data

5.2.1 1D Physical Model

The 1D model was also modified from the ROMS. The governing equation of 1D ROMS model can be written as:

$$\frac{\partial u}{\partial t}+\frac{\partial (w_{pre}u)}{\partial z}-u\frac{\partial w_{pre}}{\partial z}= fv+\frac{\partial}{\partial z}(A_{kv}\frac{\partial u}{\partial z})+\tau_x \tag{5-1}$$

$$\frac{\partial v}{\partial t}+\frac{\partial (w_{pre}v)}{\partial z}-v\frac{\partial w_{pre}}{\partial z}=- fu+\frac{\partial}{\partial z}(A_{kv}\frac{\partial v}{\partial z})+\tau_y \tag{5-2}$$

$$\frac{\partial p}{\partial z}=-\rho g \tag{5-3}$$

$$\frac{\partial T}{\partial t}+\frac{\partial (w_{pre}T)}{\partial z}-T\frac{\partial w_{pre}}{\partial z}=\frac{\partial}{\partial z}(A_{kt}\frac{\partial T}{\partial z})+F_T \tag{5-4}$$

$$\frac{\partial S}{\partial t} + \frac{\partial (w_{pre} S)}{\partial z} - S\frac{\partial w_{pre}}{\partial z} = \frac{\partial}{\partial z}(A_{ks}\frac{\partial S}{\partial z}) + F_S \tag{5-5}$$

where u, v, w_{pre} are the three components of velocity; T and S are temperature and salinity; and A_{kv}, A_{kt}, and A_{ks} are the eddy viscosity coefficients for momentum, temperature and salinity, respectively; ρ and p are the density and pressure. τ_x, τ_y, F_T, and F_S are the surface x-momentum, y-momentum (i.e., wind stress), net heat flux, and net fresh water flux, respectively. Notice that the 1D tracer equation for any tracer q should be in advective form, which can be written as:

$$\frac{\partial q}{\partial t} + \frac{\partial (w_{pre} q)}{\partial z} - q\frac{\partial w_{pre}}{\partial z} = \frac{\partial}{\partial z}(A_{kq}\frac{\partial q}{\partial z}) + F_q \tag{5-6}$$

where w_{pre} is the prescribed vertical velocity, and A_{kq} is the eddy viscosity coefficient for q, while F_q is the surface flux. It is noticeable that the vertical velocity introduced non-conservation in the continuity equation, as a result the tracer equations should be discretized in the advective form as in Eq (5-6), in which the third term was added in the ROMS codes. Details about the tracer equation will be shown in Section 5.2.2.

The model solved the top 1000 m layer of SEATS station, with 25 S-layers at vertical. Daily atmospheric fluxes, which was calculated from the bulk formulations [*W T Liu et al.*, 1979], was applied at surface. The forcing includes wind stress, downward shortwave radiation, downward longwave radiation, air temperature, air pressure, precipitation rate and relative humidity, acquired from the National Centers for Environmental Prediction/National Center for Atmospheric Research (NCEP) Reanalysis data (http://www.esrl.noaa.gov/psd/data/gridded/data.ncep.reanalysis.html, Kalnay et al. 1996) distributed by the NOAA/OAR/ESRL PSD, Boulder, Colorado, USA (http://www.esrl.noaa.gov/psd/). The original data has a resolution of quarter degree. The vertical turbulent mixing was closured by a K-profile parameterization

(KPP) scheme [*W G Large et al.*, 1994a]. The KPP scheme estimates eddy viscosity within boundary layer as the production of the boundary layer depth (h_{sbl}), a turbulent velocity scale (w_x) and a dimensionless third-order polynomial shape function G as Eq (5-7).

$$A_{kv} = h_{sbl} w_x G \tag{5-7}$$

Beyond the surface boundary layer, KPP scheme includes vertical mixing collectively contributed by shear mixing, double diffusive process and internal waves.

The Mellor-Yamada Level 2.5 turbulent closure scheme was also tested [*George L. Mellor and Yamada*, 1982]. There is no significant difference between the temperature in two models, hence the discussion here are based on the KPP runs. The temperature and salinity were relaxed toward the climatological states from the WOA 2013 (https://www.nodc.noaa.gov/OC5/woa13/) with a nudging time (t=4+16e$^{z/100}$ in years) following *Li et al.* [2015], and t=7 days at -1000 m. The model was initialized with the temperature and salinity profiles of climatological July, which was interpolated from WOA2013 data. The model was cycled from 2002 to 2014. From the simulating experience, due to its simple physics, quasi-steady state can be achieved within five years, hence it is adequate to analysis the outputs with the data from second cycle.

5.2.2 Implement of the Vertical Advection

For an arbitrary tracer q (e.g., momentum, temperature or salinity), considering only the nonlinear terms, the tracer equation is:

$$\frac{\partial q}{\partial t} + u\frac{\partial q}{\partial x} + v\frac{\partial q}{\partial y} + w\frac{\partial q}{\partial z} = 0 \, . \tag{5-8}$$

Combining Eq (5-8) with the continuity equation:

$$\frac{\partial u}{\partial x}+\frac{\partial v}{\partial y}+\frac{\partial w}{\partial z}=0 , \tag{5-9}$$

yields:

$$\frac{\partial q}{\partial t}+\frac{\partial (uq)}{\partial x}+\frac{\partial (vq)}{\partial y}+\frac{\partial (wq)}{\partial z}=0 . \tag{5-10}$$

Eq (5-8) is in advective form while Eq (5-10) is so-called conservative form of tracer equation. In ROMS, conservative form was applied in order to conserve the tracer mass within any grid [*Shchepetkin and McWilliams*, 2005]. Here, however, due to the vertical velocity and the absence of horizontal divergence in 1D model, the continuity equation Eq (5-9) is invalid. For the sake of consistency with original ROMS code, 1D tracer equation was modified by

$$\frac{\partial q}{\partial t}+\frac{\partial (w_{pre} q)}{\partial z}-q\frac{\partial w_{pre}}{\partial z}=0 , \tag{5-11}$$

in which w_{pre} is the vertical velocity. The third term was added in the ROMS subroutines **step3d_t.F** and **step3d_uv.F**.

5.2.3 Observation Data

Potential temperature and salinity profiles from Argo are acquired from the World Ocean Database 2013 (https://www.nodc.noaa.gov/OC5/WOD/pr_wod.html). The data within the 2° by 2° box centered with the SEATS station was chosen to represent the state of SEATS. In total, 526 profiles were archived from 2007 to 2015 (Figure 5-1, blue dots). The potential density (ρ) profiles (Figure 5-2a) were re-constructed with Argo observed temperature, salinity and depth. At SEATS, the pycnocline (maximum density gradient, ~0.042 kg m^{-4}) is at ~-50 m, and has a maximum depth of ~-200 m (Figure 5-2a).

Delay-time monthly mean sea level anomaly (SLA) was merged from multiple satellites, and distributed by AVISO (http://www.aviso.altimetry.fr/en/data/products/sea-surface-height-products/global/msla.html). This data is on a Cartesian grid with a resolution of 1/4 degree while the temporal range is from 1993 to 2014. The SLA at SEATS station (Figure 5-3b) was obtained by a linear interpolation method.

5.2.4 Vertical Velocities

To take vertical advection into consideration, the vertical velocity (*w*) from three mechanisms was considered: Ekman pumping (WEK), eddy pumping (WEP), and background upwelling (WBK).

First of all, the quantification of WEK follows the work of *Q P Li et al.* [2015]. The distribution of WEK was described as a function of time, depth and the Ekman pumping vertical velocity [*Cushman-Roisin and Beckers*, 2011]. The Ekman pumping vertical velocity (w_e) can be calculated from the wind stress curl:

$$w_e = \frac{1}{\rho_w f} \nabla \times \vec{\tau} \quad , \qquad (5\text{-}12)$$

where ρ_w is the density of sea water, *f* is the local Coriolis parameter, and the curl was discretized with the NCEP reanalysis wind stress, τ, with a spatial resolution of quarter degree. Since NCEP reanalysis was already coupled with an ocean model, it can provide optimal estimation of the surface stress, as well as sufficient temporal coverage. The w_e has a magnitude of 10^{-6}~10^{-5} m s^{-1} (Figure 5-3c).

The Ekman depth, d_{ek}, was given by:

$$d_{ek} = 0.4\frac{u_*}{f} = 0.4\sqrt{\frac{|\vec{\tau}|}{\rho_w f^2}}, \tag{5-13}$$

where u_* is the friction velocity. The prescribed WEK equals to the w_e at the Ekman depth (seasonally approximates from -30 to -160 m), and sinusoidally decays to zero at surface and at -200 m depth, which is the bottom of pycnocline.

Secondly, the WEP is defined as the w resulted from the vertical displacement of isopycnals due to the intensification or decaying of mesoscale eddies. For the WEP, the eddy pumping mechanism proposed by *David A. Siegel et al.* [1999] was followed. Assuming the balance between the time derivative of ρ and its vertical advection (without vertical mixing and horizontal processes), the displacement of isopycnals (hereafter, DoI) can be estimated:

$$\mathrm{DoI}_\rho(z,t) = \frac{\rho(z,t) - \langle\rho(z)\rangle}{\frac{\partial\langle\rho(z)\rangle}{\partial z}} \tag{5-14}$$

Above-mentioned Argo-reconstructed $\rho(z,t)$ was applied to estimate DoI. The temporal variability of DoI is well correlated with the SLA. The correlation coefficients (CCs) between DoI and SLA are shown in Figure 5-2b as a function of depth. The top 100 m, where the variation is dominated by mixing processes and Ekman pumping, was removed from the plot. Below -100 m, the CC increases gradually, peaks at ~-500 m, and then remains relatively steady to at least -1000 m. At all depths, the regression is over 99% significance.

Hence, the relation between WEP and SLA can be written as:

$$\mathrm{WEP}(z,t) = \frac{\partial[\mathrm{DoI}(z,t)]}{\partial t} \approx \frac{\partial[\alpha(z)\cdot\mathrm{SLA}(t) + \beta(z)]}{\partial t} = \alpha(z)\frac{\partial\,\mathrm{SLA}(t)}{\partial t}, \tag{5-15}$$

where the coefficient α and β can be yielded by performing a least-square linear regression between SLA and DoI at each depth. The profile of α can be seen in Figure 5-2b.

At last, the WBK is specified as the vertical motion due to the horizontal divergence of background current, which can be deduced from long-term heat balance in vertical direction. The net heat input at SEATS station suggests that upwelling is necessary to maintain the thermal structure [*Wyrtki*, 1965]. The surface net heat flux is balanced by the cold water upwelling, the mean vertical velocity can thereby be estimated by [*Wyrtki*, 1965; *Haijun Yang et al.*, 1999]:

$$\mathrm{WBK} \sim \frac{1}{\Delta T}\frac{Q}{\rho_w C}, \tag{5-16}$$

where ΔT is the temperature difference between SST and bottom temperature (roughly 28 $^{\mathrm{o}}$C, [*Qu*, 2002]), Q is the surface net heat flux with an annual mean value of ~15 W m^{-2} [*Haijun Yang et al.*, 1999], and C is the specific heat capacity (4200 J kg^{-1} $^{\mathrm{o}}$C^{-1}). These give an estimated WBK of 1.4×10^{-7} m s^{-1}.

Alternatively, WBK can be estimated from the counterbalance of constant eddy viscosity and vertical velocity,

$$w\frac{\partial C}{\partial z} = A_k\frac{\partial^2 C}{\partial z^2}, \tag{5-17}$$

for any conservative tracer C [*Munk*, 1966; *Joe Wang*, 1986]. Eq (5-17) has an analytical solution of

$$C = C_b + (C_0 - C_b)\exp\left(\frac{wz}{A_k}\right), \tag{5-18}$$

where C_b and C_0 are the value at bottom and at surface, respectively. This model is applicable when potential temperature-nutrient relation is linear [*Dai et al.*, 2009; *Munk*, 1966], which is the case below the surface at the SEATS station [*C-C Chen et al.*, 2006; *Lu et al.*, 2015]. By fitting the Argo temperature profiles, w/A_k can be estimated as 0.0027 m^{-1}, which yields an upwelling rate of 1.0×10^{-6} m s^{-1} given the eddy viscosity of 3.98×10^{-4} m^2 s^{-1} observed in the intermediate layer near SEATS [*Q Yang et al.*, 2016]. The two upwelling rates are both tested in model cases.

The WBK is consistent with the upwelling in the intermediate layer (above -1000 m) of the northern SCS reported by *Qu et al.* [2000] and *Isobe and Namba* [2001]. Hence, it is presumed to act only when depth<-200 m beneath the pycnocline, while the WEK and WEP dominate the above layer.

Altogether, the total vertical velocity, w_{all}, is a combination of three components:

$$w_{all} = \begin{cases} \mathrm{WEK}(z \ge -100\mathrm{m}) \\ \mathrm{WEK} - \mathrm{WEP} \cdot \dfrac{z+100}{100} (-200 \le z \le -100\mathrm{m}) \\ \mathrm{WEP} + \mathrm{WBK}(z \le -200\mathrm{m}) \end{cases} \tag{5-19}$$

Sensitivity tests were designed in Table 5-1, to test whether the incorporation of the vertical velocity can improve the 1D model results, and to compare the relative importance of the three vertical motion components. The results are demonstrated in the next section.

5.3 Results and Discussion

5.3.1 Model Results

The Taylor diagram in Figure 5-4 summarizes the normalized standard deviations (STDs), CCs and normalized centered root-mean-square differences (RMSDs) of the model cases in the simulation of the observed temperature variation (also refer to Table 5-1 for the statistics). In general, the simulation of SST (-5 m) in all cases are closely excellent, because the heat flux budget dominates the temperature variation near the air-sea interface, and the modeled SST are less affected by subsurface vertical motion. All model cases presented STDs of ~0.7, CCs of >0.96 and RMSDs of ~0.40 (A5~G5 in Figure 5-4) at surface. At other depths, all cases cannot perform as well as at the surface. Without any vertical velocity, Case A presents poor agreements with observation. For instance, CCs at -150 m and -300 m are even negative. For Case B with WBK (1.4×10^{-7} m s^{-1}) only, slightly amended CC and smaller RMSD is achieved at -50 m; while at -150 m and -300 m, the temperature variation is even underestimated compared with Case A. In Case C including both WBK and WEP, the performance at -50 m is the best among all the cases (Table 5-1). However, Case A to C present large bias from the observation (3.13, 2.92 and 2.91 ^{o}C for 0-300 m, respectively). Case D, incorporating WBK and WEK, generally improves the model performance compared with the former three cases. Most of the statistics in Case E present best values (e.g., RMSD and CC for 0-300 m, Table 5-1) among Case A to F. In particular, when the WBK of 1.0×10^{-6} m s^{-1} is incorporated, Case G shows better overall performance compared with Case E (best statistics for all 0-300 m).

In Case G, the temperature variation from 2007 to 2014 at SEATS are reproduced reasonable (Figure 5-5a and Figure 5-5b). On the other hand, the Argo-observed (Figure 5-5d) and modeled salinity (Figure 5-5c) also show comparable variation. The vertical heaving of 34.3 isohaline suggests that the vertical advection of saltier water is well simulated, while the subsurface salinity maximum is retained reasonably.

5.3.2 Discussion

The spatio-temporal distribution of DoI was re-constructed from Argo observation (Figure 5-3d). Then the spatio-temporal variability of DoI was decomposed by utilizing an empirical orthogonal function (EOF) analysis (Figure 5-2c and Figure 5-3a). The three leading modes count for 95.5% of the total variance. The variation of DoI is dominated by EOF1 (82.2% of the total variance) at the SEATS station below the mixed layer [*Wong et al.*, 2007]. The corresponding principal components (PCs) can be seen in Figure 5-3a, in comparison with the time series of SLA in Figure 5-3b. In terms of temporal variability, the PC1 correlates well with the altimetry observed SLA (CC=-0.78, over 99% significance). It was previous revealed that the thermocline oscillation in the northern SCS was correlated well (CC=-0.462) with sea level height [*Q Liu et al.*, 2001]. Their conclusion presents consistency with current study.

The magnitude of DoI presents monotonic increase with respect to depth (Figure 5-2c). This is due to the monotonously diminished density gradient below -100 m (Figure 5-2a), which amplifies the signal of displacement at depth [Eq (5-14)]. The vertical distribution of the amplitude of DoI (Figure 5-3d) is consistent with the larger EOF1 value at depth (Figure 5-2b). The underlying physics of the DoI variation are baroclinic modes. The vertical structures of the EOF modes correspond with the three leading baroclinic modes of vertical displacement, where the first mode dominates [*David A. Siegel et al.*, 1999]. The first baroclinic mode can be diagnosed from a free-surface, immiscible and two-layered water column [*Cushman-Roisin and Beckers*, 2011; *Gill*, 1982], where the fluctuation of isopycnic can be estimated with:

$$\mathrm{DoI} \approx -\frac{gH}{g'H_2}\mathrm{SLA} \approx -\frac{\rho_w H}{\Delta\rho H_2}\mathrm{SLA}, \qquad (5\text{-}20)$$

where the density difference between two layers, $\Delta\rho$, is ~4 kg m^{-3}; ρ_w is a reference density of 1024 kg m^{-3}, while H and H_2 are the thickness of the whole water column (3800 m) and the depth of lower layer (3500 m), respectively. Given these values, Eq (5-20) provides a coefficient of ~278 which is consistent with the magnitude of α (Figure 5-2b). It is noticeable that the estimated $\frac{\mathrm{DoI}}{\mathrm{SLA}}$ ratio in Eq (5-20) is proportional to $-\frac{1}{\Delta\rho H_2}$. As the depth going deep, Eq (5-20) predicts an amplifying ratio of DoI to SLA, which is also consistent with the profile of α in Figure 5-2b.

Generally, the first baroclinic mode reveals the vertical heaving of the main thermocline [*Q Liu et al.*, 2001; *David A. Siegel et al.*, 1999]. At intraseasonal time scale, the first baroclinic mode is majorly controlled by mesoscale eddy activities [*Q Liu et al.*, 2001]. Hence, the estimation of WEP from SLA, which is showing in Eq (5-15), provides a statistical method to incorporate the vertical motion due to mesoscale eddies with high significance. Since SLA has better temporal coverage compared with Argo data, the time-series of WEP can be extended to pre-Argo era. In addition, this method can also partially overcome the limitation of *in-situ* data in the SCS.

By comparing Case C (with WEP) with Case B (without WEP), or Case E (with WEP) with Case D (without WEP), the former cases generally show better skills in reproducing the temperature variability pattern (higher CCs and STDs closer to unity) below the surface. This indicates that the mesoscale eddy activity, which can be well represented by WEP, is the major process driving the temporal fluctuation of temperature at SEATS.

On the other hand, the incorporation of WEK generally improves the model (Table 5-1, Case B vs Case D), except at -50 m. However, the negative bias (Case D, Table 5-1) near the surface suggests that the WEK may be is stronger than that required for vertical advection, resulting in the over-cooling. By comparing Case E with Case D, it is suggested that the Ekman pumping alone may not be responsible for the variability of temperature at the SEATS station.

Considering all the three processes, Case E presents outstanding performance amongst the first six model cases. Moreover, Case G shows best model skills in all cases, characterized with best STD, CC, RMSD, and overall bias for 0-300 m (Figure 5-4, also can be seen from those in magenta in Table 5-1). In particular, Case G largely reduces the overall bias compared with Case E (0.6403 vs. 0.8812 ^{o}C). All of these indicate that the method applied here is appropriate to quantify the vertical motion at the SEATS station.

In terms of WBK, with an assimilated model, *Xu and Oey* [2014] estimated a basin-wide upwelling of 1.0 Sv (1.0×10^{6} m^{3} s^{-1}) from the water mass imbalance (i.e., more input, 3.4 Sv, than output of 2.4 Sv) in the intermediate layer. The corresponding upwelling rate is ~0.6×10^{-6} m s^{-1} if divided by the area of SCS at 500 m depth (~1.57×10^{12} m^{2}). *C-T A Chen et al.* [2001] deduced an upwelling rate of 1.7×10^{-6} m s^{-1} (55 m per year) from water mass age evidence in the intermediate layer, which was also adopted by *Dai et al.* [2009]. Overall, WBK in Case G (1.0×10^{-6} m s^{-1}) falls within the values in previous studies. Case G suggests that this value better represents the intensity of the intermediate layer upwelling. Nevertheless, the circulation in the intermediate layer is unclear yet and merits further study [*Xu and Oey*, 2014].

It is noticeable that the model underestimated the mixed layer depth, especially in winter (Figure 5-5a and Figure 5-5b). Possible reasons are: first, due to the simple physics in 1D model, the vertical shear from the circulation is absent, which also contributes to turbulent mixing. Secondly, other sophisticated processes, such as wind-eddy interaction, nonlinear Ekman pumping or submesoscale activities, may also play a role in vertical mixing. Last, the turbulent closure scheme was generally tuned in the condition where vertical advection is absent [*W G Large et al.*, 1994a], which may also result in underestimation of mixed layer depth, as well as the temperature variance.

The comparisons between modeled and Argo-observed salinity (Figure 5-5c and Figure 5-5d) also support the capability of current methods in simulating the 1D vertical processes. The salinity profiles are characterized with subsurface salinity maximum water saltier than 34.6 PSU. The source of this water can be tracked back to the high-salinity North Pacific Tropical Water [*Qu et al.*, 2000]. Moreover, the vertical heaving of isohalines, as well as the relative stability of high salinity water, suggests a quasi-equilibrium state counterbalanced by advection and diffusion processes.

5.4 Summary

In order to apply 1D model in parameter-tuning process in 3D ecosystem model, a case study at SEATS station in the SCS was conducted. Three types of vertical velocities are included in 1D simulation. The vertical velocities considered here are WEK, WEP and WBK. The WEK was determined from classical Ekman pumping vertical velocity and a presumed profile. The WEP component was yielded from the time change rate of DoI, while the DoI was determined by the least-squared regression between SLA and Argo-based DoI. The underlying physics are reconciled with the first baroclinic mode of vertical displacement. The WBK was estimated from the long-term heat balance. The sensitivity experiments suggest that the case with all three vertical velocities presents the best performance in modeling the temperature variation. The quantification of the three vertical velocities is universal, and hence can be applied in the simulation of other stations.

Indeed, all the model cases underestimate the variance at all depths, which may be due to the additional variation of the reconstructed Argo data in 2^{o} by 2^{o} area compared with stationary data. This also implies the temperature fluctuation in association with other processes, such as wind-eddy interaction, quasi-geostrophic, and nonlinear Ekman pumping, can incontrovertible induce large variability. Neglecting these processes might also contribute to the underestimation of temperature variability. However, incorporation of these processes is out-of-scope of this study, which can be considered in 3D model.

Table 5-1 Summary of the statistics for seven model cases

		Case A	Case B	Case C	Case D	Case E	Case F	Case G
WBK, (unit: m s^{-1})		×	1.4×10^{-7}	1.4×10^{-7}	1.4×10^{-7}	1.4×10^{-7}	×	1.0×10^{-6}
WEP		×	×	○	×	○	○	○
WEK		×	×	×	○	○	○	○
Normalized STD	**5m**	**0.7094***	**0.7105**	**0.7091**	**0.7402**	**0.7389**	**0.7383**	**0.6898**
	50m	**0.5392**	**0.5352**	**0.5402**	**0.5007**	**0.5110**	**0.5029**	**0.5170**
	150m	**0.1480**	**0.1384**	**0.1766**	**0.2497**	**0.3291**	**0.3145**	**0.3498**
	300m	**0.2560**	**0.2167**	**0.5133**	**0.0948**	**0.3192**	**0.3084**	**0.3499**
	0-300m	**0.7414**	**0.7619**	**0.7619**	**0.8243**	**0.8196**	**0.8072**	**0.8304**
Normalized RMSD	**5m**	**0.3755**	**0.3749**	**0.3758**	**0.3544**	**0.3544**	**0.3552**	**0.3912**
	50m	**0.7872**	**0.7867**	**0.7843**	**0.8367**	**0.8253**	**0.8283**	**0.8132**
	150m	**1.0404**	**1.0362**	**0.9645**	**0.9066**	**0.8676**	**0.8719**	**0.8671**
	300m	**1.0764**	**1.0607**	**0.8963**	**1.0053**	**0.8489**	**0.8543**	**0.8362**
	0-300m	**0.3585**	**0.3466**	**0.3425**	**0.2825**	**0.2774**	**0.2878**	**0.2680**
Correlation coefficient	**5m**	**0.9625**	**0.9625**	**0.9624**	**0.9671**	**0.9671**	**0.9671**	**0.9656**
	50m	**0.6207**	**0.6222**	**0.6248**	**0.5482**	**0.5660**	**0.5619**	**0.5844**
	150m	**-0.2141**	**-0.2071**	**0.2793**	**0.4774**	**0.5373**	**0.5355**	**0.5267**
	300m	**-0.1883**	**-0.1879**	**0.4456**	**-0.0267**	**0.5928**	**0.5878**	**0.6010**
	0-300m	**0.9541**	**0.9544**	**0.9564**	**0.9688**	**0.9713**	**0.9701**	**0.9724**
Overall bias (unit: °C)#	**5m**	**0.7254**	**0.7060**	**0.7057**	**-0.2387**	**-0.1536**	**-0.1958**	**-0.6511**
	50m	**1.5426**	**1.4864**	**1.4788**	**-1.3812**	**-1.1180**	**-1.2406**	**-1.4321**
	150m	**4.2954**	**4.0761**	**4.0221**	**0.2030**	**0.4763**	**0.4587**	**0.1648**
	300m	**3.0294**	**2.6719**	**2.7081**	**1.2098**	**1.3569**	**1.5487**	**0.4797**
	0-300m	**3.1334**	**2.9232**	**2.9131**	**0.8812**	**0.8824**	**0.9752**	**0.6403**

* Color of each row indicates the rank of model performance, from best to worst (best, 2nd, 3rd, 4th, 5th, 6th and worst), among the seven cases.
\# Rank here is based on absolute value.

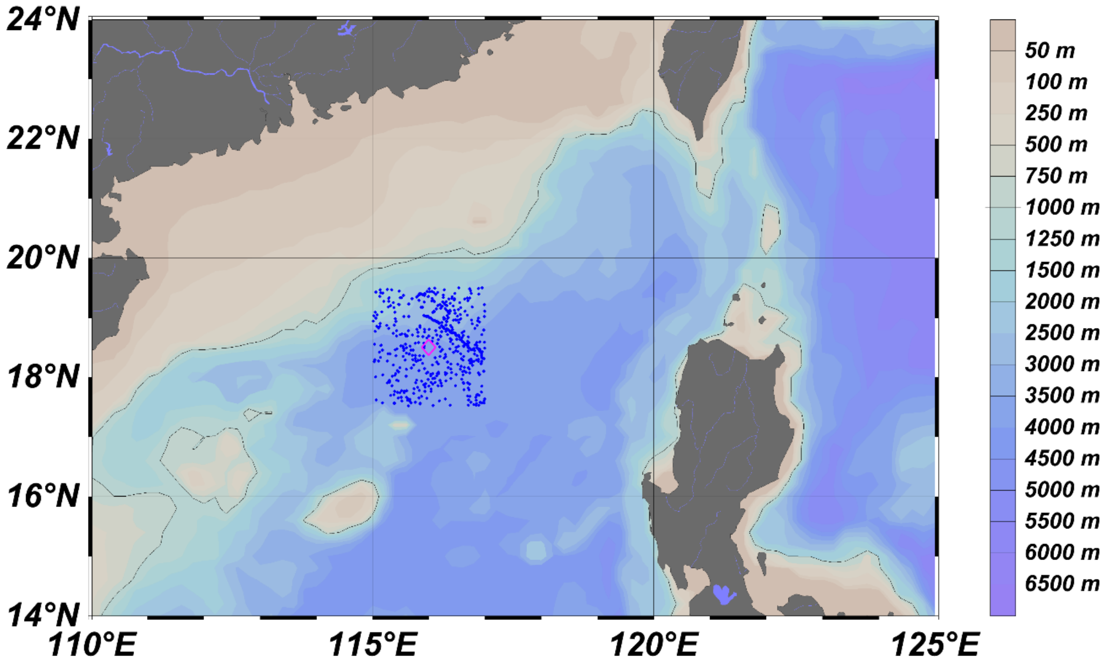

Figure 5-1 Location of SEATS station (red diamond) and all Argo observational profiles (blue dots), over the bathymetry of northern SCS (unit: meter). Black contour indicates 1000 m isobath.

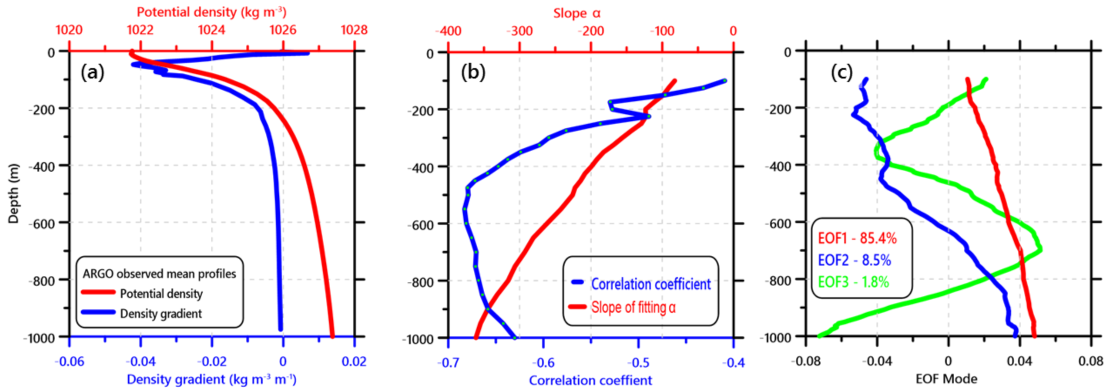

Figure 5-2 (a) Argo observational potential density (red, unit: kg m^{-3}) and its vertical gradient (blue, unit: kg m^{-3} m^{-1}); (b) The correlation coefficient (blue) and slope (red), i.e., α in equation (5-15) of the linear regression between SLA and DoI at each depth, with green dots indicating the significance level is over 99%; (c) The first three EOF modes of DoI with the legend showing the explained percentage of the total variance in each mode. In (b) and (c), the parameters above -100 m are omitted.

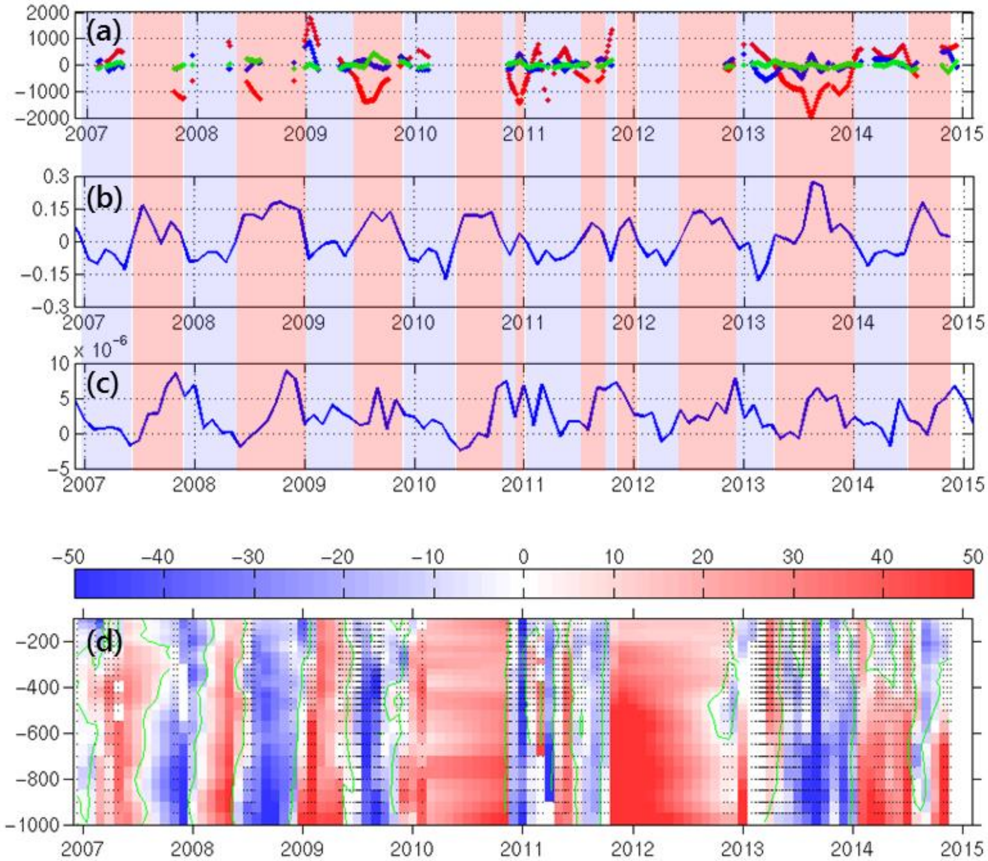

Figure 5-3 (a) Three leading (1st: red; 2nd: blue; and 3rd: green) principal components (PCs) from EOF analysis of DoI. (b) Sea level anomaly (SLA, unit: meter) at the SEATS station; (c) Ekman pumping vertical velocity (w_e, unit: m s^{-1}). Color shading is based on positive (in red) and negative (in blue) value of SLA. (d) Hovmöller diagram of the DoI (unit: meter), with green contours indicating the zero values, and the black dots denoting the Argo data location.

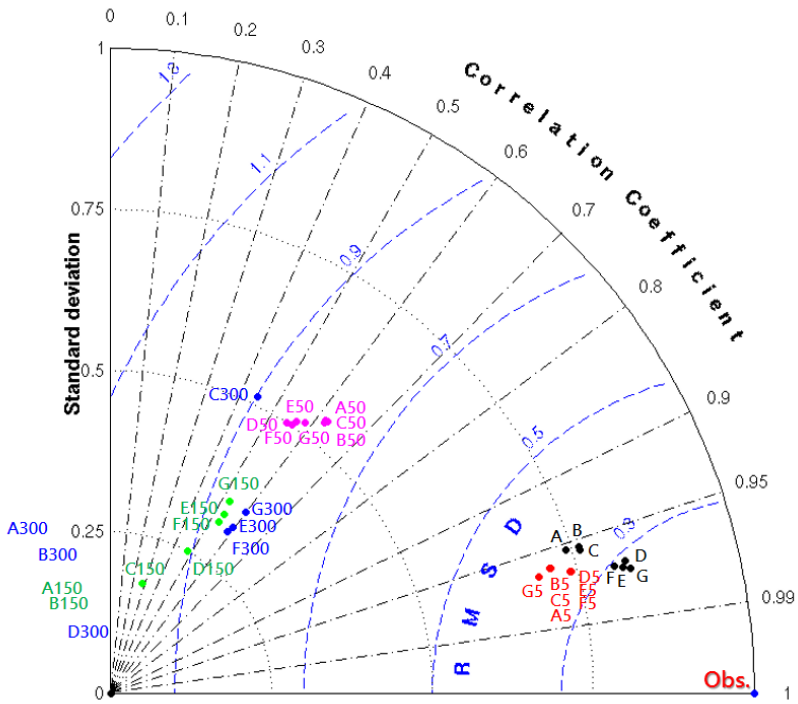

Figure 5-4 Taylor diagram summarizing the performance of temperature simulations (labeled with different letters) at -5 m (red dots), -50 m (magenta dots), -150 m (green dots), -300 m (blue dots) and those for all depths above -300 m (black dots). All RMSDs and STDs were normalized by dividing the STD of Argo observational temperature at each depth. The A150, A300, B150, B300 and D300 points are out of the figure domain since they have negative CCs.

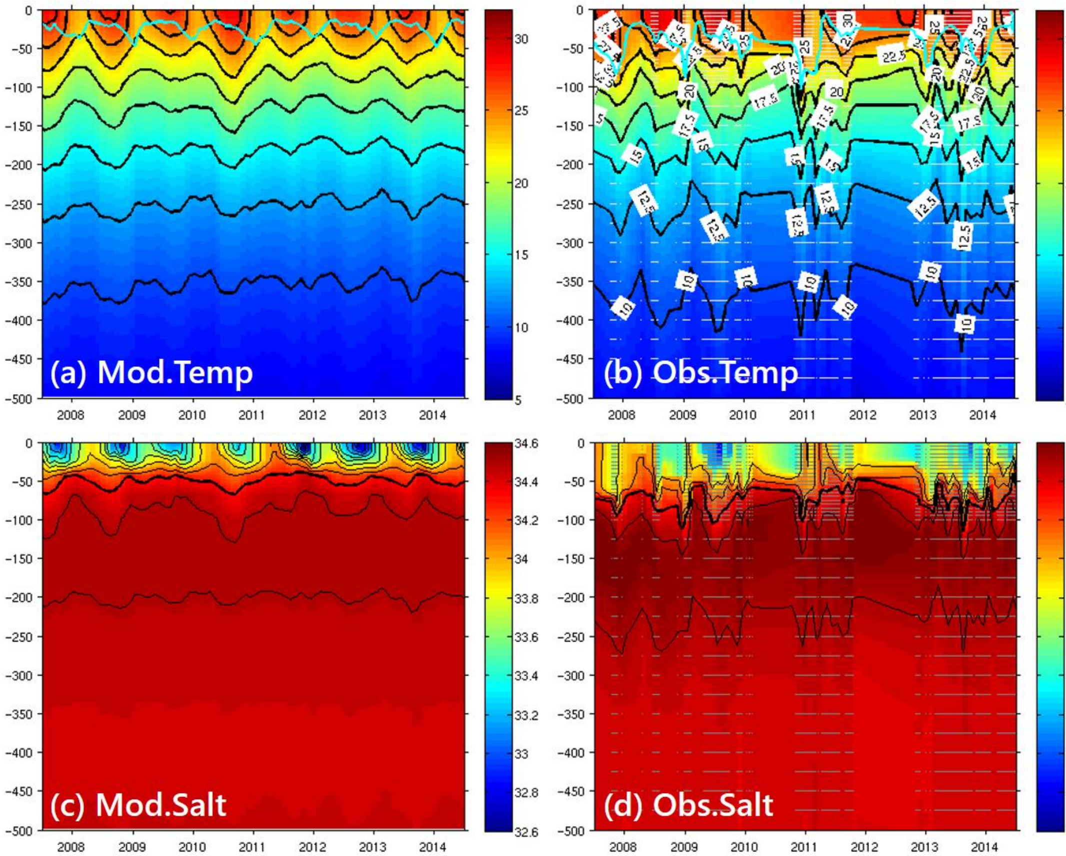

Figure 5-5 Time-depth maps of Case G (a, c) and Argo observed (b, d) temperature (unit: ^{o}C) and salinity (unit: PSU). Cyan contours in a and b indicate the mixed layer depth (defined by the depth of -0.5 ^{o}C from surface temperature). Grey dots show the Argo stations, while the data was resampled to regular monthly points. In c and d, bold contours are 34.3 PSU isohaline, while the interval is 0.2 PSU.

Chapter 6

ON THE SUMMER VIETNAM UPWELLING SYSTEM

This chapter is organized as follows. In Section 6.1, model configuration, numerical experiment, observed data, and statistical method used in this chapter are respectively described. In Section 6.2, following the analysis of the statistical results of remote sensing data, are the validation of the model system. A series of modeled spatio-temporal distribution of prognostic variables, from both the standard run and the sensitivity experiment, are also presented. In Section 6.3, the dynamic processes are comprehensively examined and analyzed. At last, the findings and conclusions are summarized in Section 6.4.

6.1 Data, Methods and Model

6.1.1 Data

Several datasets were adopted for the analysis. The surface wind vectors were from the Cross-Calibrated Multi-Platform (CCMP) gridded data, which is a long-term (25-year), six-hour, and high-resolution (1/4º) product fused from several microwave radiometers and scatterometers using a variational analysis method [*Atlas et al.*, 2011]. Monthly Aqua Moderate Resolution Imaging Spectroradiometer (MODIS) level-3 CHL (4 km resolution) was obtained from the NASA Distributed Active Archive Center (DAAC, http://oceancolor.gsfc.nasa.gov/). The estimated monthly net primary production (NPP) was derived from MODIS CHL data via the standard chlorophyll-based Vertically Generalized Production Model (VGPM) algorithm

[*Behrenfeld and Falkowski*, 1997] (available at http://www.science.oregonstate.edu/ocean.productivity/). The VGPM NPP products had a resolution of 1/10 degree, covering the period from July 2002 to October 2016. Gridded monthly-mean Absolute Dynamic Topography (ADT, available at http://www.aviso.altimetry.fr/en/data/products/sea-surface-height-products/global/) at 1/4^o resolution was produced by Ssalto/*Duacs* *(*http://www.aviso.oceanobs.com/duacs/*)*, and was distributed by *Aviso* with support from the Centre National d'Etudes Spatiales (*Cnes*)*. The 1/4^o Optimum Interpolation Sea Surface Temperature (OISST, also known as Reynolds 0.25v.2) was constructed by combining the Advanced Very High Resolution Radiometer satellite and other observation data (ships and buoys), which was obtained from the National Climatic Data Center of NOAA (https://www.ncdc.noaa.gov/oisst/data-access). In-situ observed nitrate and CHL profiles from the western SCS stations (*Figure 6-1*b) were adopted, which were detailed in Jiao et al. [2014]*.

6.1.2 Methods

6.1.2.1 Upwelling Intensity (UI) and Kinetic Energy (KE)

In wind-driven coastal upwelling system, the upwelling intensity (UI) was extensively used as a proxy to reflect the strength of upwelling e.g., [*Z Chen et al.*, 2012; *Gruber et al.*, 2011]. UI can be expressed by Eq (6-1) as the along-shore component of wind stress τ_y divided by the Coriolis parameter f and sea water density ρ_0 (constant, 1025 kg m^{-3}). The wind stress was estimated from the CCMP winds using the bulk formula where ρ_a is the air density (constant, 1.2 kg m^{-3}); C_D is the drag coefficient and U_y is the alongshore wind speed. The CCMP data, which satisfied both criteria: (1) with 100% data coverage, and (2) closest to the coastline among the points satisfying first criterion, was first decomposed locally into cross-shore and along-shore coordinate. Then the along-shore component was used to calculate UI.

$$\mathbf{UI} = -\frac{\tau_y}{\rho_0 f} = -\frac{\rho_a C_D U_y |U_y|}{\rho_0 f}, \tag{6-1}$$

On the other hand, the kinetic energy (KE) of the near-surface geostrophic current was employed as an indicator of the circulation intensity. The near-surface absolute geostrophic current was firstly derived from ADT per the geostrophic balance. Then KE can be estimated as:

$$\mathbf{KE} = \frac{1}{2}\left(u_g^2 + v_g^2\right) = \frac{1}{2\rho_0^2 f^2}\left[\left(\frac{\partial \mathbf{ADT}}{\partial x}\right)^2 + \left(\frac{\partial \mathbf{ADT}}{\partial y}\right)^2\right], \tag{6-2}$$

6.1.2.2 Multivariable Linear Regression

In order to understand the statistical relations among biological productivity, circulation and wind variability, a multivariable linear regression analysis (MLR) was conducted to fit the equation:

$$\mathbf{NPP} = b_1 \mathbf{UI} + b_2 \mathbf{KE} + b_3, \tag{6-3}$$

where b_1 to b_3 are the parameters to be determined. Data from the summer months (MJJAS) were chosen to be analyzed since the monsoon during this period is upwelling-favorable. Monthly-basis VGPM NPP was used as an estimation of biological productivity in the upwelling system. Contributions from other variables, such as SST, day length and the photosynthetically active radiation, were implicitly considered during processing the VGPM NPP [*Behrenfeld and Falkowski*, 1997].

Box VB region was predefined, following the coastline of VBUS between 8°N and 14°N, and extending 3° offshore (Figure 6-2b). Both NPP and KE were averaged over VB, while only the data in their overlapping period from 2002 to 2012 were analyzed. The results are shown in Section 6.2.

6.1.3 TFOR-CoSINE Model on Rectangle Grid

For the VBUS system and vast SCS interior, the resolution of the TFOR grid is too coarse to be eddy-resolving. Hence, another model system was developed based on TFOR. The model grid covers the whole SCS domain, and a substantial part of the North-Western Pacific, with a grid resolution of 1/10 degree (Figure 6-1a). The number of nodes in *x* and *y* direction are 382 and 500, respectively. At vertical, 25 σ-levels was derived with θ_s=3.0, θ_b=0.8 and h_c=10 m. Following the bulk formulation scheme [*W T Liu et al.*, 1979], daily atmospheric fluxes were applied at surface. The atmospheric forcing includes downward shortwave radiation, downward longwave radiation, air temperature, air pressure, precipitation rate and relative humidity, acquired from the National Centers for Environmental Prediction/National Center for Atmospheric Research (NCEP/NCAR) Reanalysis data (http://www.esrl.noaa.gov/psd/data/gridded/data.ncep.reanalysis.html, [*Kalnay et al.*, 1996]) distributed by the NOAA/OAR/ESRL PSD, Boulder, Colorado, USA (http://www.esrl.noaa.gov/psd/). The surface wind vectors were from the Cross-Calibrated Multi-Platform (CCMP) gridded data, which is high-resolution (1/4 degree) product fused from several microwave radiometers and scatterometers (Wentz, F.J., J. Scott, R. Hoffman, M. Leidner, R. Atlas, J. Ardizzone, 2015: Remote Sensing Systems CCMP 6-hourly ocean vector wind analysis product, Version 2.0, Available online at www.remss.com/measurements/ccmp). The original data has a resolution of quarter degree, and was interpolated to the model grid. The vertical turbulent mixing was closured by KPP scheme [*William G Large et al.*, 1994b], as detailed in Section 5.2.1. Biharmonic horizontal mixing scheme [*Griffies and Hallberg*, 2000] with an eddy viscosity coefficient of 2.7×10^{10} m^4 s^{-1} was applied, following the value of *Bryan et al.* [2007] used in circulation models with same horizontal resolution.

The BGC module is the Carbon, Silicon, Nitrogen Ecosystem (CoSINE) model [*Xiu and Chai*, 2014], which consists of 31 state variables, including four nutrients [nitrate (NO_3), ammonium (NH_4), silicate ($SiOH_4$), and phosphate (PO_4)], three phytoplankton functional groups (representing picoplankton, diatoms and coccolithophorids), two zooplankton classes (i.e., microzooplankton and mesozooplankton), four detritus pools [particulate organic nitrogen (PON), particulate organic carbon (POC), particulate inorganic carbon (PIC) and biogenic silica ($bSiO_2$)], two dissolved organic matters [labile (LDOM) and semi-labile (SDOM) for both carbon and nitrate], dissolved oxygen (DO), total alkalinity (TALK), total CO_2 (TCO_2), and bacteria nitrogen (BAC). The CoSINE model was successfully applied in the study on the primary production [*G Liu and Chai*, 2009], mesoscale eddies and their impacts [*Guo et al.*, 2015], and the phytoplankton community structure [*Ma et al.*, 2013; 2014]. Due the high complexity of the CoSINE module, the parameter-tuning process with a 3D model was computational inefficient. In order to solve this problem, previous 1D model was applied to tune various parameters in the CoSINE module. The final parameters applied in the 3D model are shown in Table 6-1.

The physical modeled was initialized from resting state and the WOA climatological temperature and salinity distribution. The initial distribution of nutrients was also interpolated from WOA climatological data. Small values were analytically assigned to other ecosystem variables since the ecosystem module is insensitive to the initial conditions, except for nutrients. After being spun up for 13 years with climatological forcing, the model was restarted with the ecosystem module driven by high resolution forcing (i.e., CCMP and NCEP) from 2002 to 2011. The model outputs from 2005 to 2011 are analyzed.

6.1.4 Sensitivity Experiment

To quantify the contribution from the coastal jet, we seek the modeling approach that suppresses the generation of the coastal jet separation, while retains the regional properties in summer VBUS. For the VBUS system, changing the wind-forcing might be an intuitive candidate to suppress the jet separation. However, per our experience and test, the response of the upwelling system is rather sensitive to the direct wind changes. In contrast, the response of the jet separation is less sensitive the wind [*Gan and Qu*, 2008]. Alternatively, considering that the nonlinear advection is of essence in the formation and separation processes of the coastal jet [*Gan and Qu*, 2008; *G Wang et al.*, 2006], modifying the physics of the model may be a reasonable option. Considering the fundamental physics of jet separation, a numerical experiment was accordingly conduct that runs without the nonlinear advection terms in the momentum equations following *Gruber et al.* [2011]. It is noted that in the experiment the advection terms in the tracer equations are still enabled, which allows for transport of active and passive (ecosystem) tracers. Hereafter, the experiment is referred as NO_ADV run.

6.2 Results

In this section, the analysis of satellite-based observational data is first presented focusing on the spatio-temporal covariance of wind, the jet, and the biological production. After assessing the performance by validating against observation, the model outputs are analyzed with the same MLR. The distributions of modeled quantities are also depicted and discussed in this section.

6.2.1 Spatio-temporal Analysis of Satellite Data

Figure 6-2 presents the geographical distribution of the mean (Figure 6-2a) and the standard derivation (with emphasis on the VBUS, Figure 6-2b) of MODIS surface CHL (unit: mg m^{-3}), overlapped with the information of the surface currents (mean ADT and KE). During summer months, the surface CHL presents extremely low concentration of <0.1 mg m^{-3} in the central SCS basin. In contrast for the VBUS, mean CHL concentration is more than fivefold (>0.5 mg m^{-3}) along the southern Vietnamese coast. The high CHL water also extends offshore to the interior of SCS, in conjunction with the direction of the boundary jet. The jet overshoots towards northeast, and then bifurcates into a further northeastern current and a quasi-stationary anti-cyclonic eddy (AE, Figure 6-2a). Centered at ~ 11ºN near the tip of Vietnamese coast, high KE (>1.0 m^2 s^{-2}) appears near the coast. The high variability of CHL in summer coincides with KE, implying the contribution from the jet (Figure 6-2b).

To analyze the temporal co-variation of NPP, UI and KE, these quantities were first averaged over box VB (Figure 6-2b). The averaged time-series of monthly UI, KE and NPP are shown in Figure 3a-c, which are characterized by regulated seasonal cycles and substantial interannual variability. KE peaks in summer months, while delays with respect to UI with a phase lag. Meanwhile, NPP is dominated by a biannually signal, as well as complex non-seasonal signals. The MLR analysis summarized in Figure 3c and Figure 3d shows clear positive contributions to the biological production from UI and KE. Unsurprisingly, UI dominates more than half (R^2=0.6120 for UI solely) of the total variability in NPP, which is consistent with studies in other wind-driven upwelling systems [*Gruber et al.*, 2011]. When KE is considered, additional variability in NPP is explained (R^2=0.7311, $p<0.01$). Although a significant correlation (p=0.0468) between UI and KE can also be found, only 12.54% variation in KE is explained by UI, suggesting that wind and the circulation can be regarded as two independent variables in controlling the productivity in the VBUS. Further investigation with corresponding 8-day data also shows a similar and significant relationship even after 60-day high pass filter (despite the correlation is lower, R^2=0.1873, $p<0.01$, not presented in figures), demonstrating that this robust co-variation is valid not only for time scale longer than one month, but also for subseasonal scale.

To further illustrate the modulation of the local circulation to the ecosystem, with an emphasis on different regimes of the coastal current, the high-NPP-anomaly (HNA) and low-NPP-anomaly (LNA) scenarios of the currents were composited according to the non-seasonal NPP anomaly. The climatological signal was firstly removed from the summertime NPP (Figure 6-3c), yielding the non-seasonal NPP anomaly. The thresholds for HNA and LNA scenarios were defined as (above) 75% and (below) 25% percentile of the NPP anomaly, respectively. The velocity and direction for LNA, HNA and the normal state (i.e., neither LNA nor HNA) are respectively depicted in Figure 6-4a to c, as well as the ADT difference between HNA and LNA (Figure 6-4d). Distinct from the familiar separation and offshore jet pattern (Figure 6-2a and Figure

6-4c), the circulation in LNA tends to flow northward along the isobath of central Vietnam coast (Figure 6-4a). On the other hand, compared with that during normal years (Figure 6-4c), the circulation in HNA shows very similar AE pattern in the southern SCS with the flow speed ~20% larger than the normal state. As part of AE, a recirculation is discernable at ~8.5ºN, which will be shown critical in the local BGC cycle (Section 6.3). In HNA, the jet is more dissipated and slightly weakened at the separation tip compared with LNA. In box-VB average, the KE in HNA is 0.0827 $m^2 s^{-2}$, ~65% larger than that in LNA (0.0502 $m^2 s^{-2}$). The discrimination of flow pattern is consistent with a dipolar ADT difference, by which a northwestward (inverse to the jet) pressure gradient force anomaly is imparted to the flow (Figure 6-4d), which is responsible for the jet separation process [*Batchelor*, 1967; *Gan and Qu*, 2008].

The along-coast circulation pattern in LNA can be largely ascribed to El Niño events. During the summer after El Niño, the jet separation pattern disappeared, which was associated with the abnormally weak summer monsoon [*S P Xie et al.*, 2003]. Besides of the remarkable impacts of ENSO on the SCS summer monsoon, it is still unclear whether and how the coastal jet modulates the productivity here, and how much the associated processes contribute to the production. The above questions, especially the internal physical-BGC coupling, cannot be answered via simply investigating the remote sensing data.

6.2.2 Model Validation

By virtue of numerical simulation, the detailed dynamic processes could be better illustrated with the emphasis on the effects of oceanic internal adjustments. Here, the numerical model is first validated against observation data.

In Figure 6-5, the simulated SST and NPP are compared with the observations. The model results reasonably reproduce the observed OISST and VGPM NPP patterns in summer. In particular, model captures the SST gradient from south (~28ºC) to north (>29ºC). The offshore cold filament overshooting from VBUS to the interior of SCS is also clearly represented in the model. However, the modeled SST shows a systematic cold bias of ~1ºC. On the other hand, the modeled NPP do not well simulated the extreme high values (>1000 mg C m^{-2} d^{-1}) along the Vietnamese coast, which is partially attributed to the nearshore overestimation of the retrieved NPP (which can be traced to the uncertainty in remote sensing CHL) widely reported e.g., [*Loisel et al.*, 2017]. Beyond the coasts, the model well reflects the shoreward gradient of productivity, which is generally high where influenced by the jet.

The time series of modeled SST, surface KE and NPP, which were averaged over box VB, are shown respectively in Figure 6-6, in comparison with the corresponding observations. Thanks to the realistic surface forcing with high temporal resolution, and the well-tuned CoSiNE module, the physical and biological properties in the VBUS are successfully reflected. The biannual signals in all three quantities agree well with the observations, implying the cold filament's role in accordance with the finding of *S P Xie et al.* [2003]. In terms of interannual variability, for instance, the 2010 El Niño event, characterized with weaker monsoon (Figure 6-3a), warmer SST, and reduced KE, is simulated consistently with previous studies e.g., [*S P Xie et al.*, 2003], although the production drawdown is slightly weaker than the observation. Flaw in the simulated SST exists during peak and trough months, which leads to the underestimated amplitude of SST annual cycle by ~1.0 ºC. For the surface current and productivity, our model exhibits excessive KE and insufficient production during winter, but the model-observation discrepancy is much less in other seasons. The overestimated KE is partially contributed by the ageostrophic (e.g., Ekman) components in our modeled surface current. Nevertheless, one can conclude that the model well reproduced the temporal variability in the VBUS system.

In addition, the vertical profiles of simulated nitrate and CHL, as two fundamental components in marine ecosystem, are compared with observations (Figure 6-7). Modeled nitrate generally captures the oligotrophic state near surface and the nutricline approximately at 100 m. Below the nutricline, the vertical gradient of nitrate experiences moderate slope to the deep. The largest uncertainty which occurs at ~200 m is acceptable, since the major concerns are the production processes in the euphotic zone (~100 m thick). For the CHL, model well simulates the concentration, not only at surface (not shown in figures) but also in subsurface layer. The subsurface CHL maxima appears at ~20 m, which is shallower than that in the observation. This could be explained by the overestimated nitrate concentration, since the enhanced nutrient condition prompts the phytoplankton to grow better in well-lighted shallower water.

In summary of the previous validation, one can found that the model performs reasonably in reproducing the key spatio-temporal features in the hydrodynamic and biological system of VBUS. Inevitably, some discrepancies exist. Possible reasons for these discrepancies include insufficient horizontal resolution, unrealistic parameterizations (e.g., turbulent mixing), inaccuracy in the atmospheric forcing, or uncertainties in the ecosystem parameters. However, considering current scope and focus, these shortcomings are accepted.

6.2.3 Spatio-temporal Analysis of Model

Following the analysis in Section 6.2.1, MLR analysis on the model outputs were conduct. The modeled NPP presents a phase lag with respect to the UI and KE variation. When NPP is lagged for one month, the correlation is 75.2% with a p-value of 0.0214, suggesting a strong regulation of the physical forcing to the production. The NPP response is especially sensitive when the KE is low (the steeper slope when KE<0.05 m^2 s^{-2} in Figure 6-8a). The nonlinear relationship between UI-normalized NPP and KE implies that very high KE instead limits the production.

From the modeled multiyear summer-averaged outputs, the three-dimensional distribution of the 3D circulation and potential density in VBUS is presented in Figure 6-9a to d, with the corresponding sea surface height. Consistent with the features in previous studies, the coastal current flows northward along the shelf [*Hein et al.*, 2013]. The current also dissipates the freshwater from the Mekong River, but the latter seldom spreads away from the coast. Consistent with previous studies, the coastal current veers at ~11ºN, directs offshore and then separates, forming the quasi-stationary AE centered at ~110ºE, 9ºN. Near the core of AE, vigorous vertical motion near surface can be found, implying submesoscale processes in play. West to 108ºE, intensive onshore flow ascends in the bottom Ekman layer. The high-density bottom water outcrops at 107 ºE, rejoining the coastal water and directing north, thus forming a circuit.

The distribution of the BGC state variables reveals that the ecosystem is largely controlled by the circulation (Figure 6-9e to h). Lateral nutrient gradient appears at the periphery of AE, which is characterized with depressed nitrate isosurface in the core and domed isosurface due to the upwelling and river injection near the coast (Figure 6-9e). Sustained by the river-injected and locally upwelled nutrient near the coast, primary production (PP) is stimulated with a surface maximum of > 30 mg C m^{-3} d^{-1} (Figure 6-9g). The enriched organic matter is then advected offshore by the jet (Figure 6-9h), leading to the offshore phytoplankton bloom in inversed-U shape which is familiar during summer VBUS (e.g., Figure 6-5d). The jet also conveys the water with high particulate organic carbon (POC, which includes "dead" particulate organic carbon and all planktonic carbon) offshore. The distribution of POC is somewhat deeper and more dissipated than that of high PP water, suggesting the vertical sinking and lateral transport processes [*Nagai et al.*, 2015]. Meanwhile, the remineralization of POC results in subsurface ammonium maximum at ~50 m (Figure 6-9f) consistent with the previous modeling study in SCS [*Q P Li et al.*, 2015]. Part of the high-ammonium water is nitrified, while the rest portion rejoins the circulation with the upwelling water in the bottom Ekman layer.

In summary, the summer-mean state from the model outputs clearly reveals circuiting circulation and cycled ecosystem, which will be further discussed in Section 6.3.

6.2.4 Reynolds Fluxes

To further identify the transport of the mean circulation from other processes (e.g., mesoscale eddy), a Reynolds decomposition was conduct following the conventional manner [*Colas et al.*, 2011; *Gruber et al.*, 2011; *McWilliams*, 2008; *Nagai et al.*, 2015]. The quadratic expression of the product *uX* in the advection terms can be decomposed into a mean flux and a perturbated flux [*Cushman-Roisin and Beckers*, 2011]:

$$\langle uX \rangle = \langle u \rangle \langle X \rangle + \langle u'X' \rangle \tag{6-4}$$

Since it is modulated by the East Asian Monsoon, the mean circulation in VBUS also presents strong seasonality. Therefore, climatological mean is here defined as the mean terms by averaging the model results from multiyear run, while the departure from the climatology as the fluctuated terms. The tracer equation for *C* can be written as:

$$\frac{\partial C}{\partial t} = -\frac{\partial(\langle u_j \rangle \langle C \rangle)}{\partial x_j} - \frac{\partial(\langle u'_j C' \rangle)}{\partial x_j} + \frac{\partial}{\partial x_j}\left(K_j \frac{\partial C}{\partial x_j} \right) + S \quad , \tag{6-5}$$

where u_j is the velocity tensor, x_j is the coordinate tensor, K_v is the eddy diffusivity, and *S* represents the source and sink terms due to biological activities.

It is informative to investigate the 3D distribution of the fluxes of nitrate transport (Figure 6-10). In the summer VBUS, the advection fluxes are dominated by the mean flux, which follows the mean circulation pattern. The most intensive offshore transport occurs near the separation point contributed also by the river input nutrient. Then the nutrient advection clearly bifurcates into a northward and a southward part. The nutrient in the northern part leaks to the interior of SCS, while the recirculation in the south recycles nutrient back near the slope (~108ºE, 8ºN), where the bottom water ascends (also see Figure 6-9c).

On the other hand, the eddy fluxes should be attributed to a mixture of at least mesoscale signal and the interannual signal of the mean current. Although it is difficult to differentiate the two processes, the eddy fluxes are much weaker than that from the mean fluxes. It was suggested that the propagation of the mesoscale signals in the wester SCS is rather noisy because of the complexity of the VBUS system [*Zhuang et al.*, 2010a], which is also the case here (Figure 6-10b and Figure 6-10d). Generally, the eddy fluxes tend to transport nutrient westward, adverse to the mean fluxes, especially in the north periphery of the anticyclone AE. Hence, the eddy flux may be interpreted as the eddy-trapping mechanism, which trapped the interior water and propagated westward [*F Liu et al.*, 2016].

6.2.5 Experiment Results

With a similar manner, the 3D distribution of quantities in NO_ADV experiment is illustrated (Figure 6-11). The sea surface height in experiment NO_ADV is characterized with small-scale meanders (contours in Figure 6-11), in contrast with the compact shape in the standard run. The northward component is intensified while with a weak tendency of separation. Over the shelf, the circulation can be identified largely isobath-following due to the absence of nonlinear effects in NO_ADV run. On the other hand, the 3D distributions of the BGC quantities shown in Figure 6-11 are essentially quasi-equilibrium states when the VBUS system is controlled by the linear dynamics. The inorganic nutrients present a considerable reduction in the VBUS. Specifically, the extremely low nitrate water in the surface layer of AE expands to the north, while the nutricline is deepened slightly. It is also noticeable that the upwelled dense and high-nutrient water are suppressed compared with those in Figure 6-9, although the vertical velocity magnitude over the slope is visually unchanged. The near surface concentration of ammonium reduces from ~0.25 mmol m^{-3} to ~0.15 mmol m^{-3}, while the subsurface maximum is also vague. In accordance, the PP in the experiment shows a weaker tendency of offshore injection, while leakage with the alongshore circulation to the north is discernable (Figure 6-11g). The underlying dynamics will be discussed in the next section.

6.3 Discussion

6.3.1 Biogeochemical Cycle in VBUS

Via the satellite-based and simulation-based statistical analysis, robust and consistent positive contribution from the coastal jet to the biological production was revealed, in addition to the contribution from the wind, in the summer VBUS system. The contribution of the mean current is distinct from some other coastal upwelling systems, where the offshore transport by the mean current appears to suppress the production by reducing the nearshore nutrient inventory [*Gruber et al.*, 2011; *Nagai et al.*, 2015].

From the modeled mean state of summer ecosystem (Figure 6-9), the following cycle can be deduced occurring in the VBUS: (1) The locally upwelled and riverine input nutrient (majorly in inorganic form) stimulates high production near the south Vietnam coast. (2) After being produced, the organic matters are transported offshore by the jet, with the water characterized with high CHL (e.g., Figure 6-2a) and high POC in the euphotic zone; (3) A significant portion of the nutrient (majorly in organic form) is transported back to the south of VBUS by the westward recirculation of AE. The quasi-stationary rotating AE impedes further offshore leakage of the nutrients. (4) Locally, the organic matters are remineralized, forming the subsurface maxima of ammonium and replenishing the nitrate by nitrification. Afterwards, the nutrients are upwelled by bottom Ekman pumping and wind-induced upwelling, and finally rejoin in the local BGC cycle.

6.3.2 Dynamic Analysis

The speed of the BGC cycle (Section 6.3.1) in the VBUS plays a significant role in controlling the productivity. By controlling the available nutrients, the circulation regime largely determines the speed of the BGC cycle in the VBUS. The influence of the circulation is further elucidated by the following arguments comparing the difference of the ecosystems in the standard run and NO_ADV experiment as summarized in Table 6-2. The horizontal and vertical fluxes of nitrate in three scenarios are also depicted in Figure 6-12.

In the VBUS, the availability of nutrients principally controls the productivity [*Hein et al.*, 2013]. Considering a steady state of total nitrogen in a coastal box region, river-injected and upwelled nutrient should be counter-balanced by vertical export production and lateral exchanges. The lateral exchanges include both advection and diffusion, while it was pointed out that horizontal mixing is one or two order-of-magnitude lower than that of horizontal advection [*Lu et al.*, 2015]. Hence, the lateral exchanges are determined mostly by the advective fluxes normal to the boundary of the predefined box. Given the fact the standard run and NO_ADV experiment have the same riverine input and similar export flux (Figure 6-9 and Figure 6-11), one can infer that the difference between two model cases is largely in consequence of the lateral transports and upwelled fluxes of nutrients.

In the LNA (Figure 6-4a) and also in the NO_ADV experiment (Figure 6-11), the circulation pattern shifts from the jet and separation pattern to an along-isobath pattern, which modifies the local BGC cycle. As revealed from NO_ADV, more nutrient is transported northward and offshore out of VBUS and never comes back, leading to a dramatic reduction of the nutrient concentration (Figure 6-12). The effect by the recirculation can be quantified by the cross-section nutrient flux across 109ºE section. In the NO_ADV run, the westward flux of nitrate is significantly reduced by 38.2% (Table 6-2). The reduction of nutrient is also accompanied with suppresses the upward nutrient flux (-46.5%) near the shelf edge (~100 m). As a consequence of more leakage outflux and less upwelling influx, the nitrate reservoir and new production are significantly reduced by 20.6% and 21.9%, significantly inhibiting the primary production process (15.7%, Table 6-2). Other ecosystem constituents decrease to a limit degree, such as -2.87 % for ammonium, and -3.25% for DOC. This interpretation is further supported by the post-El Niño scenario in 2010, where the most significant suppression occurs in the vertical nutrient flux (-99.6%), while the horizontal fluxes also respond to decrease. Due to the drawdown in the wind-induced upwelling and the recirculation (Table 6-2), the production is extremely low in summer 2010 (Figure 6-3c).

The more intensive separation, the larger KE in box VB, and vice versa. The accelerated coastal current is associated with intensified cross-isobath transport by bottom Ekman [*Gan et al.*, 2009]. Hence, high KE is linked to accelerated BGC cycle, which modulates the VBUS in accordance with previous analysis. In addition, the regime with intensive KE is favorable for eddy genesis. When the coastal jet is intensified, the upstream nutrient transport from the eddy flux (see Section 6.2.4) can also be expected to increase. This effect further hinders the lateral leakage, thereby should be considered contributing affirmatively to the production, although the magnitude is secondary compared with those from mean fluxes (Figure 6-10).

Combining all the effects, the intensified circulation is a condition favorable for the nutrient inventory in VBUS, especially during relatively low KE scenarios (e.g., Figure 6-3d). However, as the KE increases (i.e., >0.075 $m^2 s^{-2}$ in remote sensing and >0.1 $m^2 s^{-2}$ in model), direct offshore transport from the jet exceeds the effect of recirculation, leading to the stable, even decreasing tendency of NPP (Figure 6-3d and Figure 6-8a).

6.4 Summary

Via analyzing the summertime remote sensing data in the VBUS, a tight spatio-temporal covariation of ecosystem and near surface circulation was revealed. The water with high KE appeared to coincide with high CHL variability. Over monthly scale, statistical analysis suggested that high level of productivity was associated with high level of surface current intensity, which accounted for ~12% of the variability in productivity. Especially, the very low-level scenarios were related with a local circulation pattern shifting from the intensive separation pattern to a moderate alongshore non-separated pattern, which is largely due to the interannual monsoon variability.

To further investigate the linkage between the circulation and the productivity in VBUS, a regional physical-biological coupled model system was configurated. Numerical experiment was also designed to reproduce the non-separated circulation pattern, while retaining the monsoon forcing. The modeled result was validated favorably compared with the remote sensing and *in situ* observation data. In particular, model reproduced the positive contribution from the nonlinear recirculation intensity to the production.

Inspection into the model results highlighted the circulation's role in local BGC cycle. As schematic diagram in Figure 6-13, the separation and resultant quasi-stationary anticyclone were favorable for the onshore recirculation of nutrients. During non-separation scenarios, the nutrients northward transported by the alongshore current would never come back to VBUS, leading to a net loss in organic nutrients.

The nutrient loss further induced the feedback summarized in Figure 6-13b, which could reduce the nitrate inventory by ~25% and the NPP by ~16% in the experiment with weak separation. The weakened coastal current is also associated with reduced bottom Ekman transport, hence further reducing the vertical flux of nutrient. As the KE increasing, the BGC cycle in the VBUS was accelerated, resulting in the positive correlation to the production. During high KE scenarios (e.g., >0.075 $m^2 s^{-2}$ in remote sensing and >0.1 $m^2 s^{-2}$ in model), the direct offshore transport exceeded the contribution of recirculation, hence resulting in the stable even decrease tendency of NPP.

Table 6-1 Ecosystem parameters for CoSINE module

Parameter	Symbol	Value
NH_4 inhibition for P1	ψ_1	**1.5**
NH_4 inhibition for P2	ψ_2	1.5
NH_4 inhibition for P3	ψ_3	**1.5**
Half-saturation for NO_3 uptake by P1	K_{P1_NO3}	1.0
Half-saturation for NH_4 uptake by P1	K_{P1_NH4}	0.1
Half-saturation for NO_3 uptake by P2	K_{P2_NO3}	3.0
Half-saturation for SiO_4 uptake by P2	K_{P2_SiO4}	4.5
Half-saturation for NO_3 uptake by P3	K_{P3_NO3}	1.0
Half-saturation for NH_4 uptake by P3	K_{P3_NH4}	1.0
P1 mortality(d^{-1})	γ_3	0.02
P2 mortality(d^{-1})	γ_4	0.05
P3 mortality(d^{-1})	γ_{10}	0.05
P1, P2, P3 exudation	$\varepsilon_1, \varepsilon_2, \varepsilon_3$	0.2, 0.2, 0.2
P1, P2, P3 excretion	$\varepsilon_4, \varepsilon_5, \varepsilon_6$	0.3, 0.2, 0.3
P2 sinking speed (m d^{-1})	W_2	1.0
P3 sinking speed (m d^{-1})	W_3	1.0
Z1 assimilation efficiency for N and C	γ_1	0.9
Z2 assimilation efficiency for N	γ_2	0.7
Z2 assimilation efficiency for C	γ_{22}	0.65
Z1 messy feeding fraction	Φ_1	0.1
Z2 messy feeding fraction	Φ_2	0.2
Z1 excretion	reg_1	0.1

Z2 excretion	reg_2	0.1
Z2 loss rate	λ	0.05
Z1 maximum specific grazing rate	$G1_{max}$	**1.55**
Z2 maximum specific grazing rate	$G2_{max}$	**0.56**
Half-saturation for Z1 ingestion	$K1_{gr}$	0.5
Half-saturation for Z2 ingestion	$K2_{gr}$	0.25
Z1 grazing preference for P1	ρ_5	0.9
Z1 grazing preference for BAC	ρ_6	0.1
Z2 grazing preference for P2	ρ_1	0.6
Z2 grazing preference for Z1	ρ_2	0.2
Z2 grazing preference for PON	ρ_3	0.1
Z2 grazing preference for P3	ρ_4	0.1
Chlorophyll-specific initial slope of P vs. I curve for phytoplankton	α	**0.5**
Maximum P1 carbon-specific nitrogen-uptake rate	P_{ref}^{C1}	1.5
Maximum P2 carbon-specific nitrogen-uptake rate	P_{ref}^{C2}	**6.0**
Maximum P3 carbon-specific nitrogen-uptake rate	P_{ref}^{C3}	**1.5**
Minimum phytoplankton N:C ratio	Q_{min}	0.06
Maximum phyroplankton N:C ratio	Q_{max}	0.17
Maximum value of $\boldsymbol{\theta^N}$	θ_{max}^N	1.5
$bSiO_2$ sinking speed (m d^{-1})	W_4	20
PIC sinking speed (m d^{-1})	W_5	15
PON sinking speed (m d^{-1})	W_6	10
POC sinking speed (m d^{-1})	W_7	15
Labile fraction of produced DOM	β_1	0.8
Labile fraction of phyto-excreted DOC	β_2	0.6

Fraction uptake of LDOC by BAC	β_3	0.96
Nitrification rate	γ_7	0.05
Cost of biosynthesis	ξ_{NO3}	2.33
Color fraction of LDOC	colorFR1	0.1
Color fraction of SDOC	colorFR2	0.2
PON dissolution rate	D_{PON}	0.01
PIC dissolution rate	D_{PIC}	0.01
DOM fraction P1, P2, P3 mortality	$\delta_1, \delta_2, \delta_3$	0.5, 0.5, 0.5
BAC C:N ratio	R_B	5.1
BAC mortality	γ_{12}	0.05
Phosphorus to nitrogen ratio	R_{PN}	0.0625
PIC to organic carbon ratio in P3	R_{CaC}	1.0
Maximum labile DOC or NH_4 uptake	μB_{max}	0.8
Maximum SDOC hydrolysis	γ_{13}	0.7
Half-saturation for NH_4 uptake	K_B	0.5
Half-saturation for LDOC uptake	K_L	25
Half-saturation for SDOC uptake	K_{SDOC}	417
Half-saturation for SDON uptake	K_{SDON}	35.3
Respired fraction of BAC growth	r_b	0.5
Oxygen to nitrate ratio	R_{O2NO3}	8.625
Oxygen to ammonium ratio	R_{O2NH4}	6.625

Table 6-2 Summery of the ecosystems in three model scenarios

Quantities integrated **over top 100 m of box VB**	**Standard**	**NO_ADV**	**2010 post-El Niño**
NO_3 ($\times10^9$ mol)	11.3	8.96 **(-20.6%)**	10.71 (-5.13%)
NH_4 ($\times10^9$ mol)	1.52	1.48 (-2.87%)	1.51 (-1.12%)
DOC ($\times10^9$ mol C)	234	227 (-3.25%)	236 (+0.615%)
POC ($\times10^9$ mol C)	22.7	22.4 (-1.07%)	19.9 (-12.4%)
PP (mmol N m^{-2} d^{-1})	4.65	3.92 (-15.7%)	3.57 (-23.2%)
NP+RP (mmol N m^{-2} d^{-1})	2.83+1.82	2.21+1.71 (**-21.9%**, -6.04%)	1.82+1.75 (-35.6%, -3.79%)
Fluxes			
Vertical NO_3 flux across 100 m level ($\times10^9$ mol d^{-1}, positive upward)	0.2454	0.1313 (-46.5%)	0.0011 (-99.6%)
Top 100 m integrated zonal NO_3 flux across 109ºE section* ($\times10^9$ mol d^{-1}, positive westward)	0.4156	0.2652 (-36.2%)	0.2013 (-51.6%)
Vertical volume flux across 100 m level (Sv, positive upward)	0.22	0.14 (-38.2%)	0.04 (-82.3%)
Zonal volume flux across 109ºE section* (Sv, positive westward)	0.44	0.01 (-98.8%)	0.28 (-35.3%)

* See Figure 6-12a for the location.

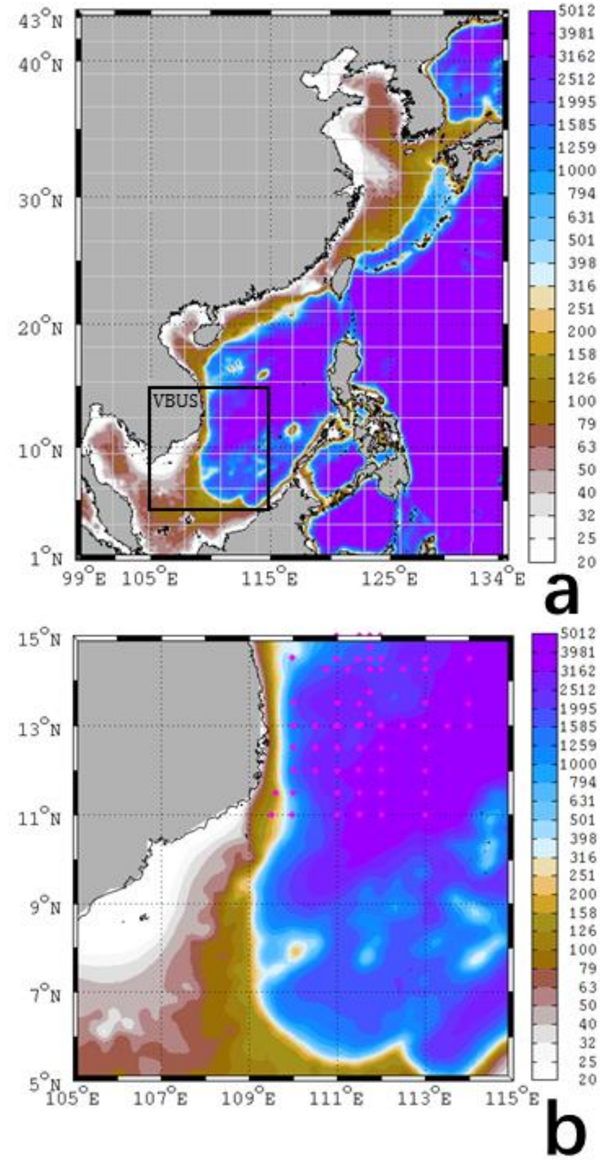

Figure 6-1 (a) Model domain and the bathymetry (unit: meter) for the TFOR-CoSiNE model. Model grid nodes are shown every 25 points. The study area VBUS is boxed. (b) Zoom-in area of VBUS. Magenta diamonds are the observation stations (see text).

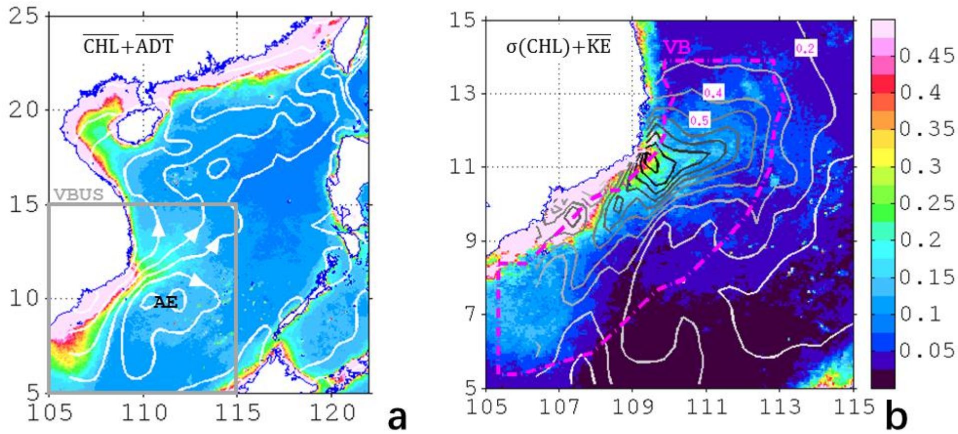

Figure 6-2 (a) Summertime average of surface CHL concentration (color shading, unit: mg m^{-3}), overlapped white contours are mean ADT with the arrows showing the directions of geostrophic currents. Gray box is the region of interest (VBUS), while AE shows the center of the anticyclone. (b) Standard derivation of surface CHL (color shading, unit: mg m^{-3}) overlapped with the contours of surface KE with an interval of 0.1 from 0.1 to 1.0 (unit: m^2 s^{-2}). Magenta box is the box VB region (see text).

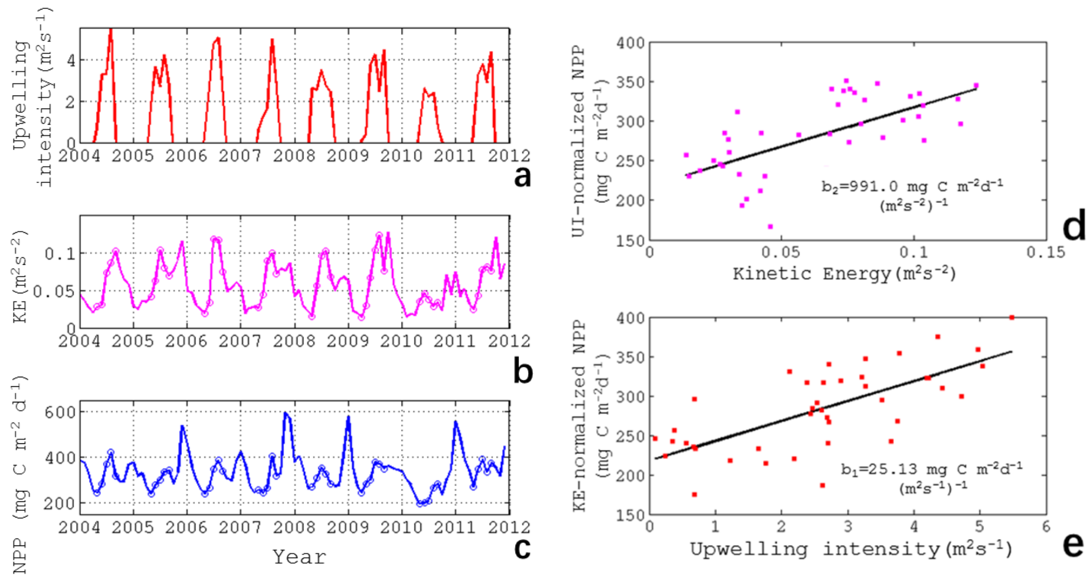

Figure 6-3 Time series of (a) UI in m^2 s^{-1}, (b) KE in m^2 s^{-2} and (c) NPP in mg C m^{-2} d^{-1}. In (a), only the positive (upwelling-favorable) values are shown. In (b) and (c), months with positive UI are marked with open circles. (d) Relationship of UI-normalized NPP to KE. (e) Relationship of KE-normalized NPP to UI. b_1 and b_2 in subplots are the coefficients of MLR.

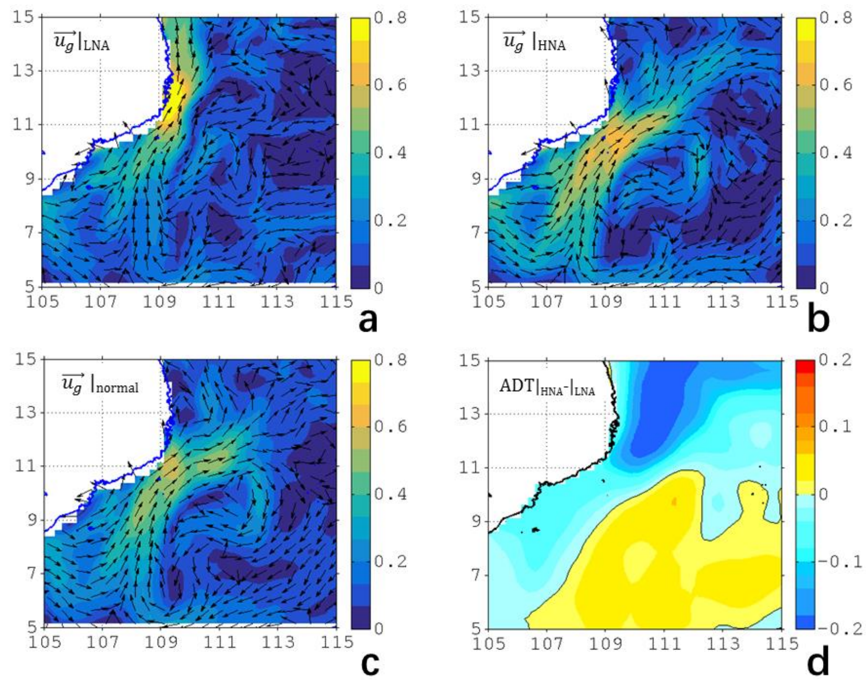

Figure 6-4 The surface geostrophic current velocity (color shading, unit: m s^{-1}) and direction (vectors) in LNA (a), HNA (b), and normal months (i.e., neither LNA nor HNA, c) scenarios (see text for criteria). (d) The differences of ADT (unit: meter) between HNA and LNA.

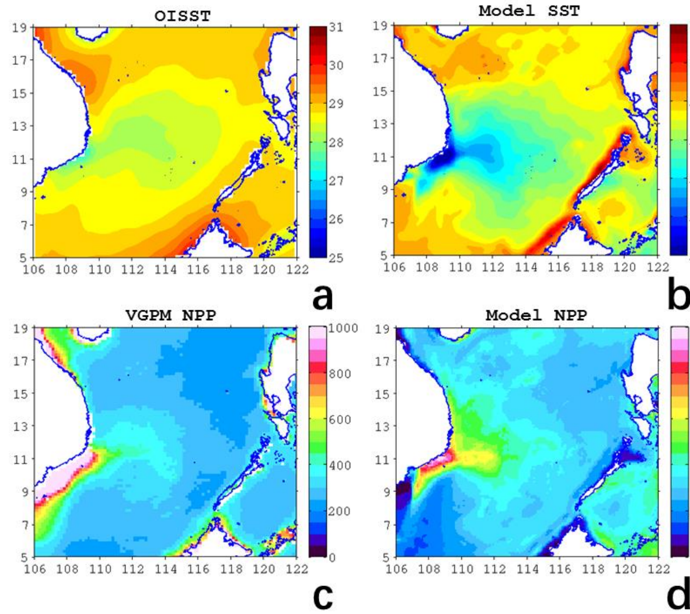

Figure 6-5 (a) OISST and (b) model SST (unit: ºC), (c) VGPM NPP and (d) modeled NPP (unit: mg C m^{-2} d^{-1}) in climatological August.

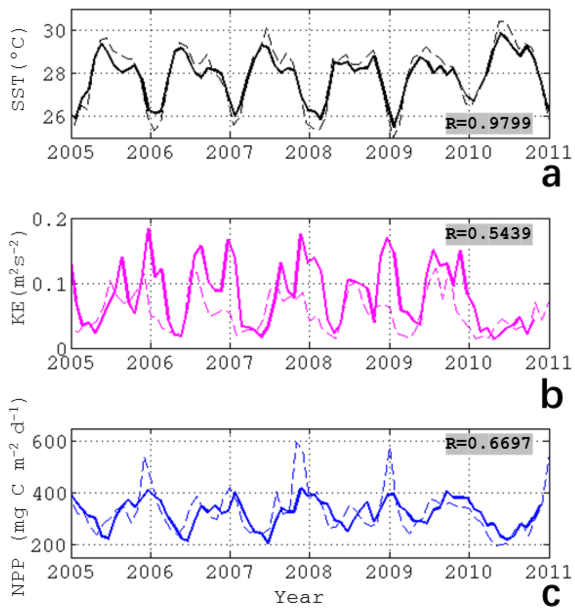

Figure 6-6 Thick lines: modeled (a) SST in ºC, (b) KE in m^2 s^{-2}, and (c) NPP in mg C m^{-2} d^{-1} averaged over box VB (see Figure 6-2b), with respective observation data (thin dashed lines).

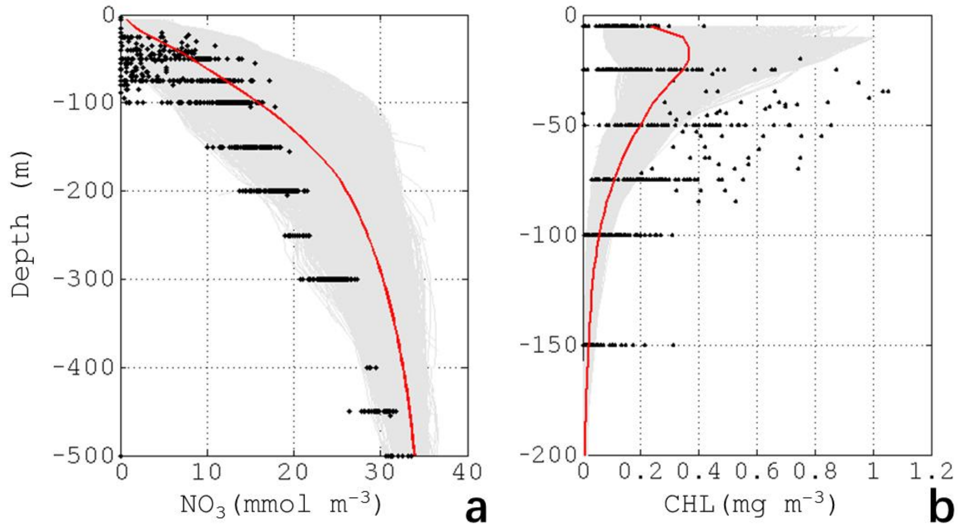

Figure 6-7 The vertical profiles of (a) nitrate concentration (unit: mmol m^{-3}) and (b) CHL concentration (unit:mg m^{-3}). In both plots, the black dots are the observation values (see Figure 6-1b for stations). The gray area are the envelop for all model stations in the same area and month, while the red lines are the area-mean profiles.

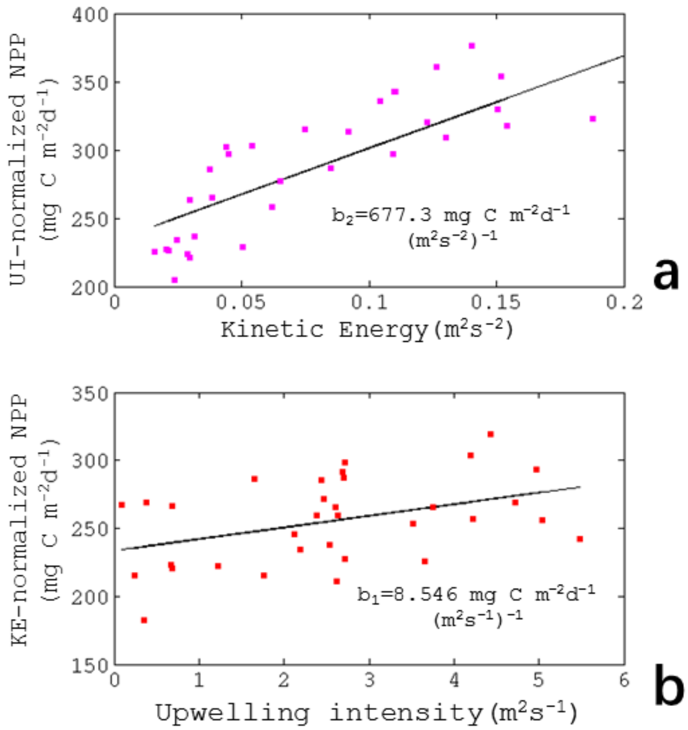

Figure 6-8 MLR analysis with modeled outputs. Same with Figure 6-3c and d.

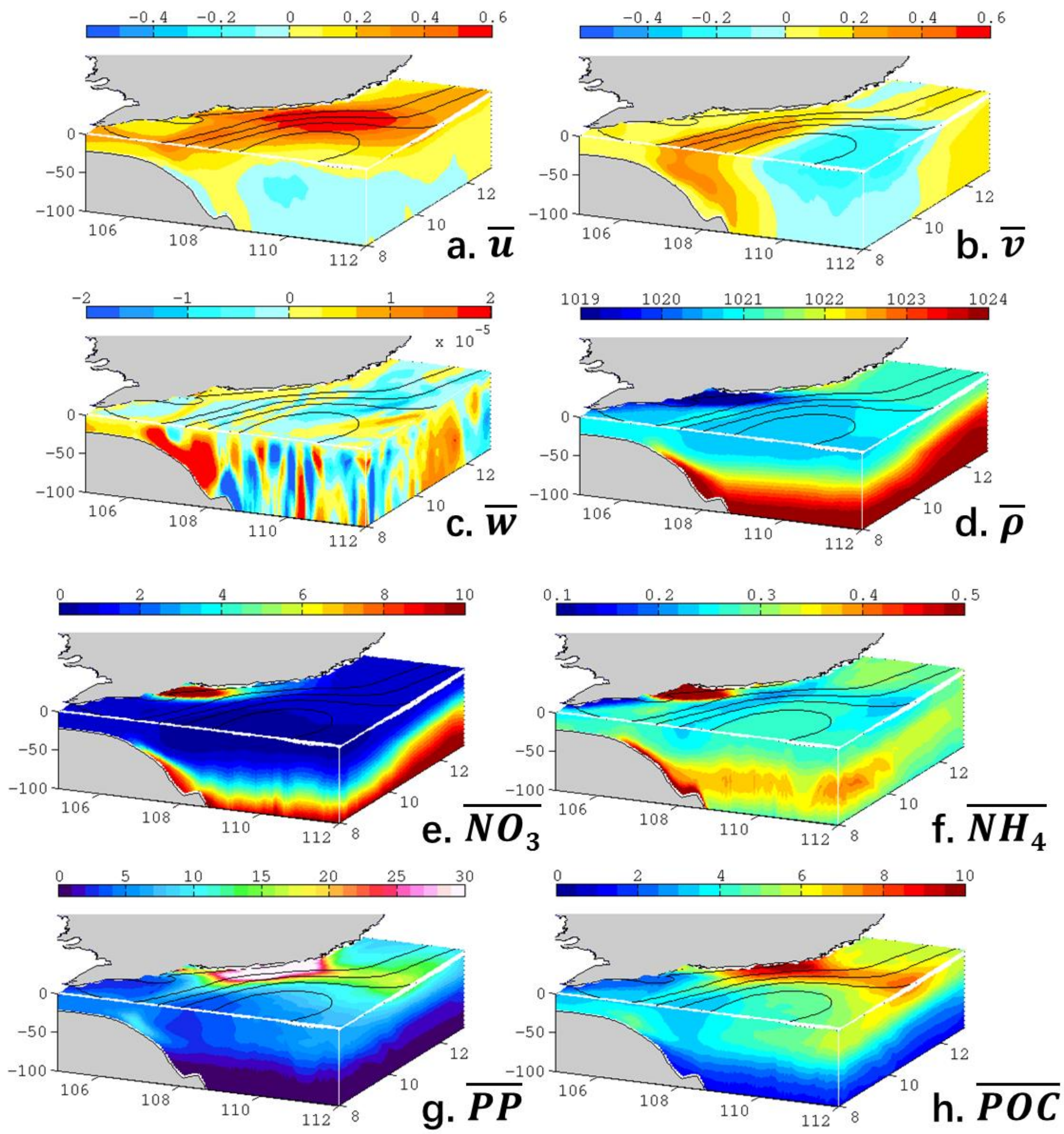

Figure 6-9 3D distribution (standard run) of the summer mean (a) zonal velocity in m s^{-1}, (b) meridional velocity in m s^{-1}, (c) vertical velocity in m s^{-1}, (d) potential density in kg m^{-3}, (e) nitrate in mmol m^{-3}, (f) ammonium in mmol m^{-3}, (g) primary production in mg C m^{-3} d^{-1}, and particulate organic carbon in mmol C m^{-3}. Overlapped contours are the mean sea level (every 0.1 m).

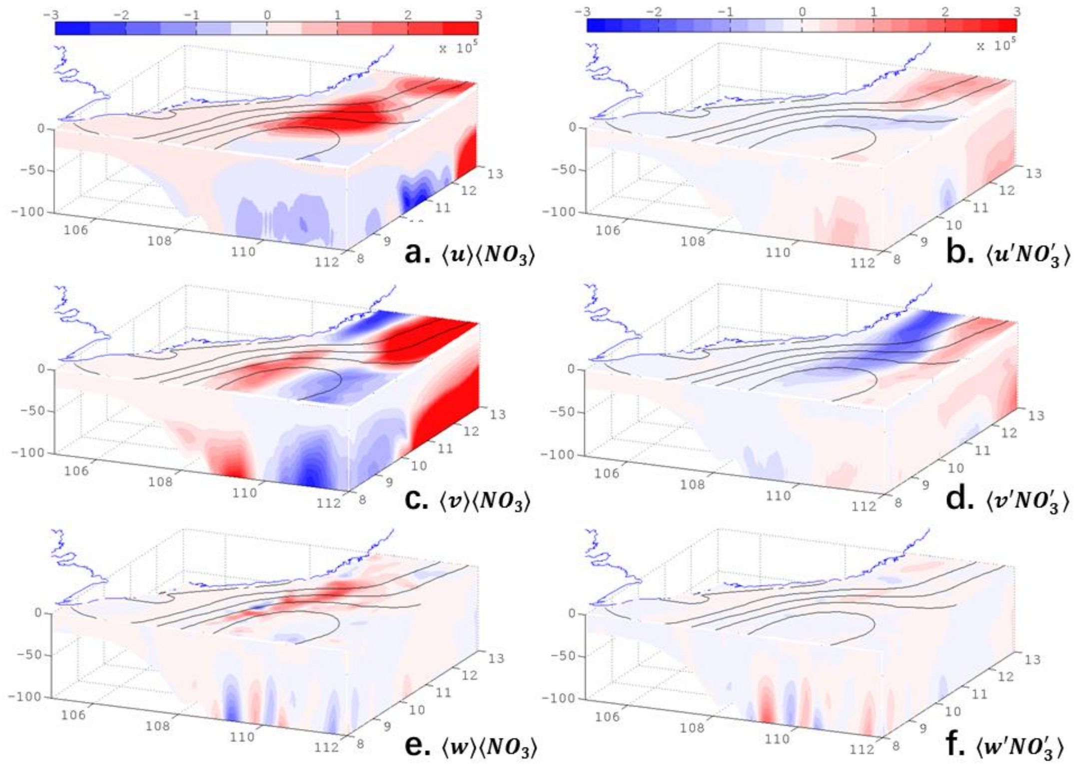

Figure 6-10 Modeled 3D mean fluxes (a, c and e) and eddy fluxes (b, d and f) in zonal (a, b), meridional (c, d) and vertical (e, f) directions for nitrate. The unit is mmol s^{-1}. For top plane, vertical averaged fluxes over 0-100 m are shown overlapped with sea level (every 0.1 m).

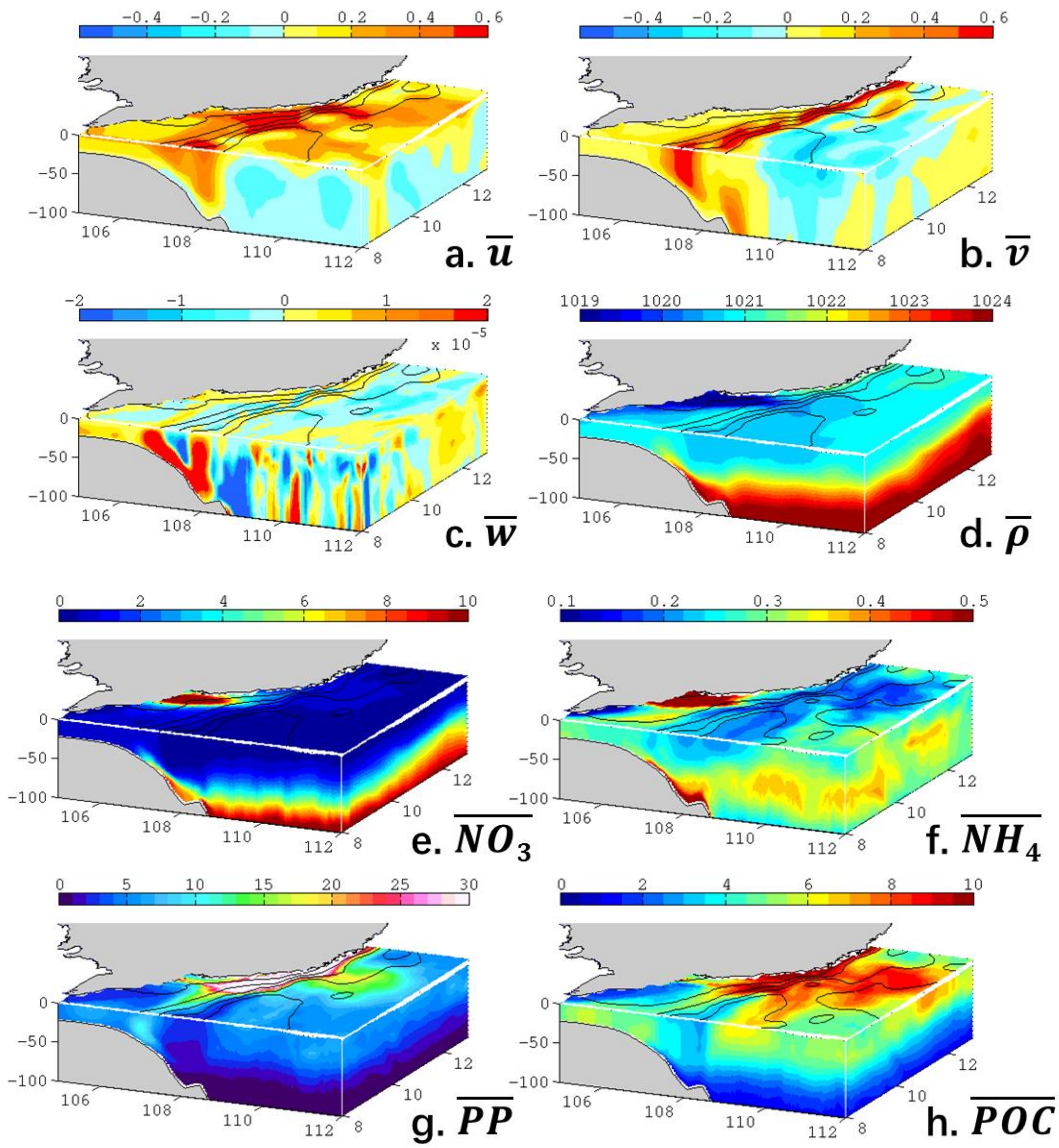

Figure 6-11 Same with Figure 6-9, but for NO_ADV model run.

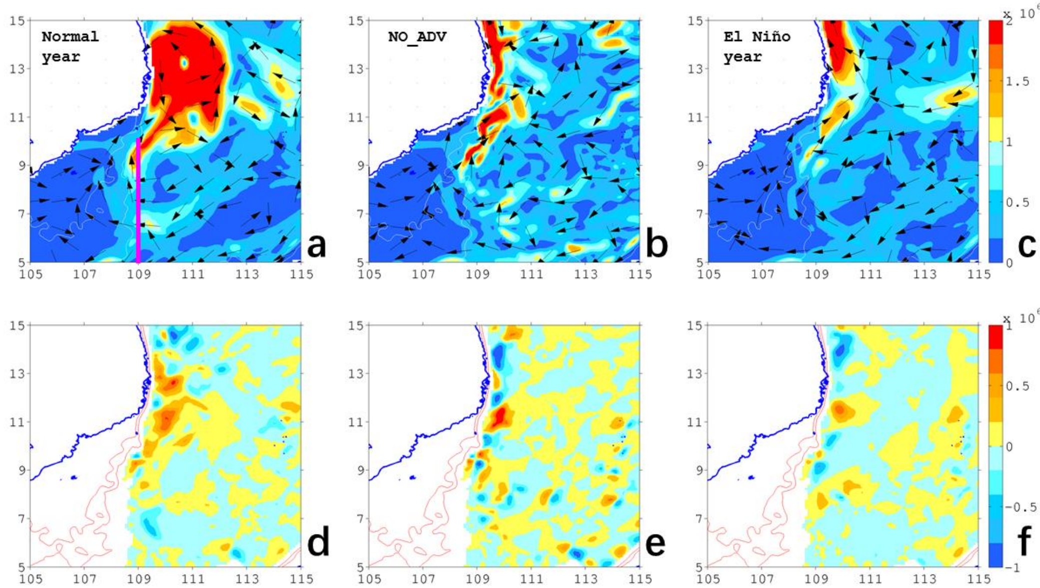

Figure 6-12 (a, b and c) Modeled 0-100 m integrated nitrate fluxes (unit: mmol s^{-1}) in horizontal plane. Color shading is the magnitude while vectors denote the direction. (d, e and f) Vertical flux across 100 m level for normal year (a and d), post-El Niño (c and f) and NO_ADV case (b and e). Overlapped contours are the 50 m and 75 m isobath. In (a), the magenta line is the 109ºE section (see Table 6-2).

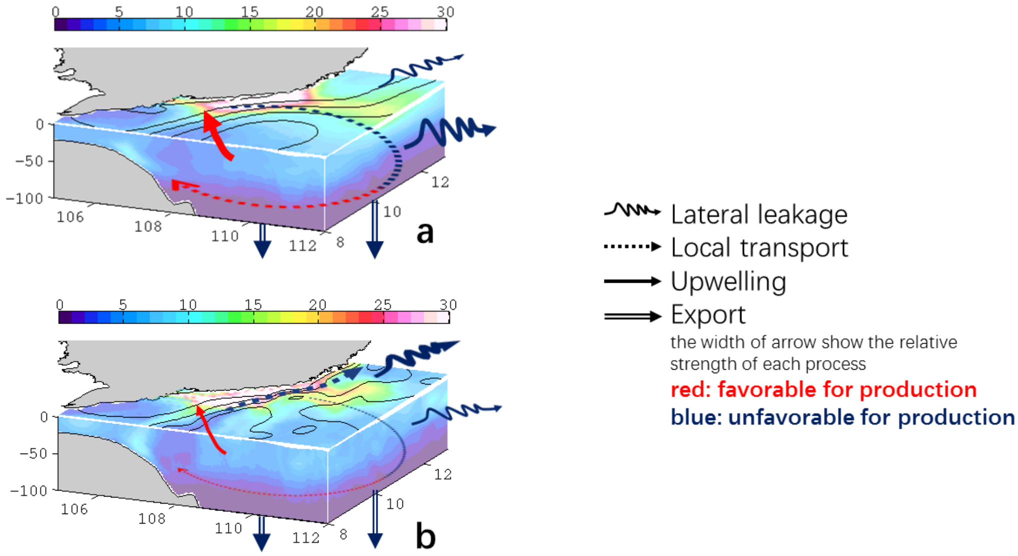

Figure 6-13 Schematic diagram summarizing the dynamics in different scenarios of distinct circulation pattern in the VBUS as diagnosed by our model simulation, overlapped with the 3D distribution of PP (unit: mg C m^{-3} d^{-1}). (a) Normal state: The separated jet transports the upwelled nutrient and produced organic matter offshore. While a substantial portion of the offshore transported organic matter leaks into the interior of SCS and never comes back, the recirculation and stationary anticyclonic eddy trap the organic matters locally, and hinder further leakage of available nutrients in VBUS. The locally recirculated nutrient is then upwelled in the bottom Ekman layer, rejoining the production process over the shelf. (b) Non-separation state: During the non-separated circulation, the along isobath circulation transports the organic matter northward. The leakage of organic matter reduces the nutrient inventory in the VBUS. The loss of nutrients diminishes the organic nutrient available for remineralization and upwelling, further inducing a reduction in the production process.

Chapter 7

CONCLUSIONS

7.1 Conclusions

For the LZB case, the two-stage mechanism can be summarized as follows. Nutrient supply from the wind-induced vertical mixing was confined to the ~40 m surface layer, while subsurface upwelling advected nutrients from below the mixed layer, which was centered at ~45 m and below. The wind-induced mixing was related with the synoptic intensification of the northeast winter monsoon, which fluctuated over weekly scale. The depth contrast between the two processes suggested that neither effect can be solely responsible for the genesis of LZB. It also explained the occasional occurrence of LZB, since the combined contribution from the two processes were necessary for LZB to be flouring, which might not be the case for every winter. This framework was in consist with the results of *J J Wang et al.* [2010], although the Ekman pumping theory invoked by *J J Wang et al.* [2010] failed to explain the mismatching centers of wind curl and LZB, i.e., failed to explain the mechanism of subsurface upwelling. In addition, the mechanism proposed in this dissertation was a new theory which successfully explained the onset time, intensity and spatial structure of LZB. This is one of the key highlights of this study.

Via the hydrodynamic diagnostics, it was found that the main contribution to subsurface upwelling was from the RV advection (WA term), while the temporal variability of vorticity (WT) and the friction term (WF) were smaller. When a spatial average was taken, the magnitude of the vertical velocity, which resulted majorly from the RV advection, was on the order of ~2 m d^{-1}, which approximated the value of modeled vertical velocity. The RV advection resulted from an offshore jet's interaction with the RV field determined from the ambient circulation. Since the wind-induced mixing possessed a larger spatial scale (for instance, >100 km), the spatial structure of the offshore jet, and hence the subsurface upwelling, largely determined the extent and distinct inversed-V shape of the offshore wing of LZB.

For the case study at the SEATS station, it revealed that various processes, including those considered in this dissertation, i.e., Ekman pumping, eddy pumping and the divergence of the background circulation, and not considered. e.g., wind-eddy interaction, quasi-geostrophic and nonlinear Ekman pumping, would inevitably induce intense vertical motion in the ocean interior or in the boundary layers. The results of the numerical simulation suggested that the case with all three vertical velocities best quantified the vertical thermal structure. For other oceanic stations, the calculation and quantification are universal, and therefore, capable to further generalize to a broad application. In addition, using 1D model as a simplified model case to conduct the parameter-tuning process was proven to be a viable and efficient way, which could also be applied in other studies.

For the case study of VBUS system, both remote sensing and numerical simulation evidences revealed a tight spatio-temporal covariation of ecosystem and near surface circulation was revealed. In space, the water with high KE appeared to coincide with high CHL variability. In time, statistical analysis suggested that high level of productivity was associated with high level of surface current intensity, which accounted for ~12% of the variability in productivity. Especially, the very low-level scenarios were related with a local circulation pattern shifting from the intensive separation pattern to a moderate alongshore non-separated pattern.

To further investigate the linkage between the circulation and the productivity in VBUS, a regional physical-biological coupled model system, i.e., the TFOR-CoSINE model system, was configurated. Numerical experiment was also designed to reproduce the non-separated circulation pattern, while retaining the monsoon forcing. The modeled result was validated favorably compared with the remote sensing and *in situ* observation data. In particular, model reproduced the positive contribution from the nonlinear recirculation intensity to the production.

Analysis on the model results highlighted the role from the local circulation in BGC cycle. As schematic diagram in Figure 6-13, the separation and resultant quasi-stationary anticyclone were favorable for the onshore recirculation of nutrients. During non-separation scenarios, the nutrients northward transported by the alongshore current would never come back to VBUS, leading to a net loss in organic nutrients. The nutrient loss further induced the feedback summarized in Figure 6-13b, which could reduce the nitrate inventory by ~25% and the NPP by ~16% in the experiment with weak separation. The weakened coastal current is also associated with reduced bottom Ekman transport, hence further reducing the vertical flux of nutrient. As the KE increasing, the BGC cycle in the VBUS was accelerated, resulting in the positive correlation to the production. During very high KE scenarios, the direct offshore transport exceeded the contribution of recirculation, hence resulting in the stable even decrease tendency of NPP.

7.2 Perspectives

As previous conclusions, for the LZB case, the mechanism can be summarized as a two-stage process, where both wind-induced mixing near the surface and nonlinearity-associated upwelling in the subsurface. However, the RV advection upwelling mechanism proposed in this study required further verification, especially with more *in-situ* data. While the linkage between RV advection and vertical motion in the meteorology had long been known [*Holton and Hakim*, 2012], this mechanism was less applied in the oceanographic researches, partially due to the difficulty in *in-situ* observation.

In addition, the vertical motion in Figure 4-8 (~19.8°N) presented a finer spatial scale than mesoscale structure, implying that submesoscale processes came into play. Intriguing submesoscale structures, e.g., intensive vertical motion, were observed when applying the nonlinear Ekman effect [*Niiler*, 1969] on the dynamics of a vortex [*Stern*, 1965] and of a submesoscale ocean front [*Mahadevan and Tandon*, 2006]. Submesoscale activities also worked efficiently to horizontally dissipate material and energy. Comparing the spatial structure in Figure 4-2d and Figure 4-2f, one could find that the high CHL water in the model was more compact and concentrated while the observed one was more dissipated. It could be hypothesized that the incapability in resolving submesoscale activities leaded to the underestimation of horizontal dissipation. However, the model resolution (~10 km) in this region in the hydrostatic regime was not capable of fully resolving the submesoscale processes. Nevertheless, submesoscale processes would drastically modify the upwelling process, which is beyond the scope of this study. Abundant eddy and frontal activities in the SCS provide many scenarios for in-depth discussion about the effects of submesoscale processes and their role in the biogeochemical system, which are deserving of future simulation and exploration.

On the other hand, for the VBUS study, the findings provide new insights into the complex physical-biological coupling in the coastal upwelling system VBUS. Moreover, this understanding may help to predict the future reaction of productivity in the SCS. As revealed by *Haiyuan Yang and Wu* [2012], the summertime near surface circulation of SCS has experienced a long-term trend of being more energetic, characterized with intensified separation and recirculation in the VBUS (see their figure 9). Whether this long-term trend of circulation will also induce potential trend in ecosystem in response to future climate changes is a topic of common interests, which merits further investigation.

REFERENCES

Atlas, R., R. N. Hoffman, J. Ardizzone, S. M. Leidner, J. C. Jusem, D. K. Smith, and D. Gombos (2011), A cross-calibrated, multiplatform ocean surface wind velocity product for meteorological and oceanographic applications, *Bull. Am. Meteorol. Soc.*, *92*(2), 157-174.

Batchelor, G. K. (1967), *An Introduction to Fluid Dynamics*, Cambridge University Press, New York.

Behrenfeld, M. J., and P. G. Falkowski (1997), Photosynthetic rates derived from satellite-based chlorophyll concentration, *Limnol. Oceanogr.*, *42*(1), 1-20.

Bryan, F. O., M. W. Hecht, and R. D. Smith (2007), Resolution convergence and sensitivity studies with North Atlantic circulation models. Part I: The western boundary current system, *Ocean Model*, *16*(3-4), 141-159, doi:10.1016/j.ocemod.2006.08.005.

Capet, X., F. Colas, J. McWilliams, P. Penven, and P. Marchesiello (2008), Eddies in eastern boundary subtropical upwelling systems, *Ocean Modeling in an Eddying Regime*, 131-147.

Chai, F., G. M. Liu, H. J. Xue, L. Shi, Y. Chao, C. M. Tseng, W. C. Chou, and K. K. Liu (2009), Seasonal and Interannual Variability of Carbon Cycle in South China Sea: A Three-Dimensional Physical-Biogeochemical Modeling Study, *J. Oceanogr.*, *65*(5), 703-720.

Chapman, D. C. (1985), Numerical treatment of cross-shelf open boundaries in a barotropic coastal ocean model, *J. Phys. Oceanogr.*, *15*(8), 1060-1075, doi:10.1175/1520-0485(1985)015<1060:ntocso>2.0.co;2.

Chen, C.-C., F.-K. Shiah, S.-W. Chung, and K.-K. Liu (2006), Winter phytoplankton blooms in the shallow mixed layer of the South China Sea enhanced by upwelling, *J. Mar. Syst.*, *59*(1–2), 97-110, doi:http://dx.doi.org/10.1016/j.jmarsys.2005.09.002.

Chen, C.-T. A., S.-L. Wang, B.-J. Wang, and S.-C. Pai (2001), Nutrient budgets for the South China Sea basin, *Mar. Chem.*, *75*(4), 281-300, doi:http://dx.doi.org/10.1016/S0304-4203(01)00041-X.

Chen, Y.-L. L., H.-Y. Chen, I.-I. Lin, M.-A. Lee, and J. Chang (2007), Effects of cold eddy on phytoplankton production and assemblages in Luzon Strait bordering the South China Sea, *J. Oceanogr.*, *63*(4), 671-683.

Chen, Z., X.-H. Yan, Y.-H. Jo, L. Jiang, and Y. Jiang (2012), A study of Benguela upwelling system using different upwelling indices derived from remotely sensed data, *Cont. Shelf Res.*, *45*, 27-33, doi:10.1016/j.csr.2012.05.013.

Chifflet, M., V. Andersen, L. Prieur, and I. Dekeyser (2001), One-dimensional model of short-term dynamics of the pelagic ecosystem in the NW Mediterranean Sea: effects of wind events, *J. Mar. Syst.*, *30*(1–2), 89-114, doi:http://dx.doi.org/10.1016/S0924-7963(01)00040-9.

Colas, F., J. C. McWilliams, X. Capet, and J. Kurian (2011), Heat balance and eddies in the Peru-Chile current system, *Clim. Dyn.*, *39*(1-2), 509-529, doi:10.1007/s00382-011-1170-6.

Cushman-Roisin, B., and J. M. Beckers (2011), *Introduction to Geophysical Fuild Dynamic*, 828 pp.

Dai, M., Z. Cao, X. Guo, W. Zhai, Z. Liu, Z. Yin, Y. Xu, J. Gan, J. Hu, and C. Du (2013), Why are some marginal seas sources of atmospheric CO2?, *Geophys. Res. Lett.*, *40*(10), 2154-2158, doi:10.1002/grl.50390.

Dai, M., F. Meng, T. Tang, S.-J. Kao, J. Lin, J. Chen, J.-C. Huang, J. Tian, J. Gan, and S. Yang (2009), Excess total organic carbon in the intermediate water of the South China Sea and its export to the North Pacific, *Geochemistry Geophysics Geosystems*, *10*(12), doi:10.1029/2009gc002752.

Dippner, J. W., K. V. Nguyen, H. Hein, T. Ohde, and N. Loick (2006), Monsoon-induced upwelling off the Vietnamese coast, *Ocean Dyn.*, *57*(1), 46-62, doi:10.1007/s10236-006-0091-0.

Falkowski, P. G., and D. Ziemann (1991), Role of eddy pumping in enhancing primary production in the ocean, *Nature*, *352*(6330), 55.

Fang, G., W.-d. Fang, Y. Fang, and K. Wang (1998), A survey of studies on the South China Sea upper ocean circulation, *Acta Oceanographica Taiwanica*, *37*, 1-16.

Flather, R. A. (1987), A Tidal Model of the Northeast Pacific, *Atmos. Ocean*, *25*(1), 22-45.

Gan, J., A. Cheung, X. Guo, and L. Li (2009), Intensified upwelling over a widened shelf in the northeastern South China Sea, *J. Geophys. Res.*, *114*(C9), doi:10.1029/2007jc004660.

Gan, J., Z. Liu, and C. R. Hui (2016), A Three-Layer Alternating Spinning Circulation in the South China Sea, *J. Phys. Oceanogr.*, *46*(8), 2309-2315, doi:10.1175/jpo-d-16-0044.1.

Gan, J., and T. Qu (2008), Coastal jet separation and associated flow variability in the southwest South China Sea, *Deep Sea Res. Part I*, *55*(1), 1-19, doi:10.1016/j.dsr.2007.09.008.

Gill, A. E. (1982), *Atmosphere-ocean dynamics*, Academic press.

Griffies, S. M., and R. W. Hallberg (2000), Biharmonic Friction with a Smagorinsky-Like Viscosity for Use in Large-Scale Eddy-Permitting Ocean Models, *Monthly Weather Review*, *128*(8), 2935-2946, doi:10.1175/1520-0493(2000)128<2935:BFWASL>2.0.CO;2.

Gruber, N., Z. Lachkar, H. Frenzel, P. Marchesiello, M. Munnich, J. C. McWilliams, T. Nagai, and G.-K. Plattner (2011), Eddy-induced reduction of biological production in eastern boundary upwelling systems, *Nature Geosci*, *4*(11), 787-792, doi:http://www.nature.com/ngeo/journal/v4/n11/abs/ngeo1273.html#supplementary-information.

Guo, M., F. Chai, P. Xiu, S. Li, and S. Rao (2015), Impacts of mesoscale eddies in the South China Sea on biogeochemical cycles, *Ocean Dyn.*, doi:10.1007/s10236-015-0867-1.

Haidvogel, D. B., et al. (2008), Ocean forecasting in terrain-following coordinates: Formulation and skill assessment of the Regional Ocean Modeling System, *Journal of Computational Physics*, *227*(7), 3595-3624, doi:10.1016/j.jcp.2007.06.016.

He, Q., H. Zhan, S. Cai, and Z. Li (2016), Eddy effects on surface chlorophyll in the northern South China Sea: Mechanism investigation and temporal variability analysis, *Deep Sea Res. Part I*, *112*, 25-36, doi:10.1016/j.dsr.2016.03.004.

Hein, H., B. Hein, T. Pohlmann, and B. H. Long (2013), Inter-annual variability of upwelling off the South-Vietnamese coast and its relation to nutrient dynamics, *Global Planet. Change*, *110*, 170-182, doi:10.1016/j.gloplacha.2013.09.009.

Holton, J. R., and G. J. Hakim (2012), *An introduction to dynamic meteorology*, Academic press.

Hood, R. R., N. R. Bates, D. G. Capone, and D. B. Olson (2001), Modeling the effect of nitrogen fixation on carbon and nitrogen fluxes at BATS, *Deep Sea Res. Part II*, *48*(8–9), 1609-1648, doi:http://dx.doi.org/10.1016/S0967-0645(00)00160-0.

Hu, J., H. Kawamura, H. Hong, and Y. Qi (2000), A Review on the Currents in the South China Sea: Seasonal Circulation, South China Sea Warm Current and Kuroshio Intrusion, *J. Oceanogr.*, *56*(6), 607-624, doi:10.1023/A:1011117531252.

Isobe, A., and T. Namba (2001), The circulation in the upper and intermediate layers of the South China Sea, *J. Oceanogr.*, *57*(1), 93-104.

Jiang, Y. W., F. Chai, Z. W. Wan, X. Zhang, and H. S. Hong (2011), Characteristics and mechanisms of the upwelling in the southern Taiwan Strait: a three-dimensional numerical model study, *J. Oceanogr.*, *67*(6), 699-708, doi:10.1007/s10872-011-0080-x.

Jiao, N., Y. Zhang, K. Zhou, Q. Li, M. Dai, J. Liu, J. Guo, and B. Huang (2014), Revisiting the CO2 "source" problem in upwelling areas: a comparative study on eddy upwellings in the South China Sea, *Biogeosciences*, *11*(9), 2465-2475, doi:10.5194/bg-11-2465-2014.

Jin, M., C. J. Deal, J. Wang, N. Tanaka, and M. Ikeda (2006), Vertical mixing effects on the phytoplankton bloom in the southeastern Bering Sea midshelf, *J. Geophys. Res.*, *111*(C3), doi:10.1029/2005jc002994.

Kalnay, E., M. Kanamitsu, R. Kistler, W. Collins, D. Deaven, L. Gandin, M. Iredell, S. Saha, G. White, and J. Woollen (1996), The NCEP/NCAR 40-year reanalysis project, *Bull. Am. Meteorol. Soc.*, *77*(3), 437-471.
Klein, P., and G. Lapeyre (2009), The Oceanic Vertical Pump Induced by Mesoscale and Submesoscale Turbulence, *Annual Review of Marine Science*, *1*(1), 351-375, doi:10.1146/annurev.marine.010908.163704.
Kuo, N.-J., Q. Zheng, and C.-R. Ho (2000), Satellite observation of upwelling along the western coast of the South China Sea, *Remote Sens. Environ.*, *74*(3), 463-470.
Kuo, N.-J., Q. Zheng, and C.-R. Ho (2004), Response of Vietnam coastal upwelling to the 1997–1998 ENSO event observed by multisensor data, *Remote Sens. Environ.*, *89*(1), 106-115, doi:10.1016/j.rse.2003.10.009.
Lévy, M., L. Mémery, and J.-M. André (1998), Simulation of primary production and export fluxes in the Northwestern Mediterranean Sea, *J. Mar. Res.*, *56*(1), 197-238.
Large, W. G., J. C. McWilliams, and S. C. Doney (1994a), Oceanic Vertical Mixing: A preview and a model with a nonlocal boundary layer parameterization, *Rev. Geophys.*, *32*(4), 363-403.
Large, W. G., J. C. McWilliams, and S. C. Doney (1994b), Oceanic vertical mixing: A review and a model with a nonlocal boundary layer parameterization, *Rev. Geophys.*, *32*(4), 363-404.
Li, J., Y. Qi, Z. Jing, and J. Wang (2014), Enhancement of eddy-Ekman pumping inside anticyclonic eddies with wind-parallel extension: Satellite observations and numerical studies in the South China Sea, *J. Mar. Syst.*, *132*, 150-161, doi:10.1016/j.jmarsys.2014.02.002.
Li, Q. P., Y. Wang, Y. Dong, and J. Gan (2015), Modeling long-term change of planktonic ecosystems in the northern South China Sea and the upstream Kuroshio Current, *J. Geophys. Res. Oceans*, *120*(6), 3913-3936, doi:10.1002/2014JC010609.
Liao, E., Y. Jiang, L. Li, H. Hong, and X. Yan (2013), The cause of the 2008 cold disaster in the Taiwan Strait, *Ocean Model*(62), 1-10, doi:10.1016/j.ocemod.2012.11.004.
Lin, I. I., C.-C. Lien, C.-R. Wu, G. T. F. Wong, C.-W. Huang, and T.-L. Chiang (2010), Enhanced primary production in the oligotrophic South China Sea by eddy injection in spring, *Geophys. Res. Lett.*, *37*(16), n/a-n/a, doi:10.1029/2010gl043872.
Lin, X., X.-H. Yan, Y. Jiang, and Z. Zhang (2016), Performance assessment for an operational ocean model of the Taiwan Strait, *Ocean Model*, *102*, 27-44, doi:10.1016/j.ocemod.2016.04.006.
Liu, F., S. Tang, and C. Chen (2013a), Impact of nonlinear mesoscale eddy on phytoplankton distribution in the northern South China Sea, *J. Mar. Syst.*, *123-124*, 33-40, doi:10.1016/j.jmarsys.2013.04.005.

Liu, F., S. Tang, R. X. Huang, and K. Yin (2016), The asymmetric distribution of phytoplankton in anticyclonic eddies in the western South China Sea, *Deep Sea Res. Part I*, doi:10.1016/j.dsr.2016.12.010.

Liu, G., and F. Chai (2009), Seasonal and interannual variability of primary and export production in the South China Sea: a three-dimensional physical-biogeochemical model study, *ICES J. Mar. Sci.*, *66*(2), 420-431, doi:10.1093/icesjms/fsn219.

Liu, K.-K., L. Atkinson, R. Quinones, and L. Talaue-McManus (2010), *Carbon and nutrient fluxes in continental margins: a global synthesis*, Springer Science & Business Media.

Liu, K. K., S. Y. Chao, P. T. Shaw, G. C. Gong, C. C. Chen, and T. Y. Tang (2002), Monsoon-forced chlorophyll distribution and primary production in the South China Sea: observations and a numerical study, *Deep-Sea Research Part I-Oceanographic Research Papers*, *49*(8), 1387-1412, doi:10.1016/s0967-0637(02)00035-3.

Liu, K. K., L. W. Wang, M. Dai, C. M. Tseng, Y. Yang, C. H. Sui, L. Oey, K. Y. Tseng, and S. M. Huang (2013b), Inter-annual variation of chlorophyll in the northern South China Sea observed at the SEATS Station and its asymmetric responses to climate oscillation, *Biogeosciences*, *10*(11), 7449-7462, doi:10.5194/bg-10-7449-2013.

Liu, Q., Y. Jia, P. Liu, Q. Wang, and P. C. Chu (2001), Seasonal and intraseasonal thermocline variability in the central south China Sea, *Geophys. Res. Lett.*, *28*(23), 4467-4470, doi:10.1029/2001gl013185.

Liu, W. T., K. B. Katsaros, and J. A. Businger (1979), Bulk parameterization of air-sea exchanges of heat and water vapor including the molecular constraints at the interface, *J. Atmos. Sci.*, *36*(9), 1722-1735.

Liu, X., J. Wang, X. Cheng, and Y. Du (2012), Abnormal upwelling and chlorophyll-aconcentration off South Vietnam in summer 2007, *J. Geophys. Res. Oceans*, *117*(C7), n/a-n/a, doi:10.1029/2012jc008052.

Loisel, H., et al. (2017), Assessment and analysis of the chlorophyll-a concentration variability over the Vietnamese coastal waters from the MERIS ocean color sensor (2002–2012), *Remote Sens. Environ.*, *190*, 217-232, doi:10.1016/j.rse.2016.12.016.

Lu, W., X.-H. Yan, L. Han, and Y. Jiang (2017), One-dimensional ocean model with three types of vertical velocities: a case study in the South China Sea, *Ocean Dyn.*, 1-10, doi:10.1007/s10236-016-1029-9.

Lu, W., X.-H. Yan, and Y. Jiang (2015), Winter bloom and associated upwelling northwest of the Luzon Island: A coupled physical-biological modeling approach, *J. Geophys. Res. Oceans*, *120*(1), 533-546, doi:10.1002/2014JC010218.

Ma, W., F. Chai, P. Xiu, H. Xue, and J. Tian (2013), Modeling the long-term variability of phytoplankton functional groups and primary productivity in the South China Sea, *J. Oceanogr.*, *69*(5), 527-544.

Ma, W., F. Chai, P. Xiu, H. Xue, and J. Tian (2014), Simulation of export production and biological pump structure in the South China Sea, *Geo-Mar. Lett.*, *34*(6), 541-554, doi:10.1007/s00367-014-0384-0.

Mahadevan, A., E. D'Asaro, C. Lee, and M. J. Perry (2012), Eddy-driven stratification initiates North Atlantic spring phytoplankton blooms, *Science*, *337*(6090), 54-58.

McWilliams, J. C. (2008), The nature and consequences of oceanic eddies, *Ocean Modeling in an Eddying Regime*, 5-15.

Mellor, G. L. (2001), One-dimensional, ocean surface layer modeling: a problem and a solution, *J. Phys. Oceanogr.*, *31*(3), 790-809.

Mellor, G. L., and T. Yamada (1982), Development of a turbulence closure model for geophysical fluid problems, *Rev. Geophys.*, *20*(4), 851-875, doi:10.1029/RG020i004p00851.

Munk, W. H. (1966), Abyssal recipes, *Deep Sea Research and Oceanographic Abstracts*, *13*(4), 707-730, doi:http://dx.doi.org/10.1016/0011-7471(66)90602-4.

Nagai, T., N. Gruber, H. Frenzel, Z. Lachkar, J. C. McWilliams, and G. K. Plattner (2015), Dominant role of eddies and filaments in the offshore transport of carbon and nutrients in the California Current System, *J. Geophys. Res. Oceans*, *120*(8), 5318-5341.

Ning, X., C. Lin, Q. Hao, C. Liu, F. Le, and J. Shi (2009), Long term changes in the ecosystem in the northern South China Sea during 1976–2004, *Biogeosciences*, *6*(10), 2227-2243.

Palacz, A. P., H. Xue, C. Armbrecht, C. Zhang, and F. Chai (2011), Seasonal and inter-annual changes in the surface chlorophyll of the South China Sea, *J. Geophys. Res.*, *116*(C9), doi:10.1029/2011jc007064.

Pascual, A., S. Ruiz, B. Buongiorno Nardelli, S. Guinehut, D. Iudicone, and J. Tintoré (2015), Net primary production in the Gulf Stream sustained by quasi-geostrophic vertical exchanges, *Geophys. Res. Lett.*, *42*(2), 441-449, doi:10.1002/2014gl062569.

Peñaflor, E. L., C. L. Villanoy, C.-T. Liu, and L. T. David (2007), Detection of monsoonal phytoplankton blooms in Luzon Strait with MODIS data, *Remote Sens. Environ.*, *109*(4), 443-450.

Qu, T. (2000), Upper-Layer Circulation in the South China Sea*, *J. Phys. Oceanogr.*, *30*(6), 1450-1460.

Qu, T. (2002), Evidence for water exchange between the South China Sea and the Pacific Ocean through the Luzon Strait, *Acta Ocean. Sin.*, *21*(2), 175-185.

Qu, T., J. B. Girton, and J. A. Whitehead (2006), Deepwater overflow through Luzon Strait, *J. Geophys. Res.*, *111*(C1), doi:10.1029/2005jc003139.

Qu, T., H. Mitsudera, and T. Yamagata (2000), Intrusion of the North Pacific waters into the South China Sea, *J. Geophys. Res.*, *105*(C3), 6415, doi:10.1029/1999jc900323.

Sasai, Y., C. Yoshikawa, S. L. Smith, T. Hashioka, K. Matsumoto, M. Wakita, K. Sasaoka, and M. C. Honda (2016), Coupled 1-D physical–biological model study of phytoplankton production at two contrasting time-series stations in the western North Pacific, *J. Oceanogr.*, 1-18, doi:10.1007/s10872-015-0341-1.

Shang, S., L. Li, J. Li, Y. Li, G. Lin, and J. Sun (2012), Phytoplankton bloom during the northeast monsoon in the Luzon Strait bordering the Kuroshio, *Remote Sens. Environ.*, *124*, 38-48, doi:10.1016/j.rse.2012.04.022.

Shaw, P.-T., S.-Y. Chao, K.-K. Liu, S.-C. Pai, and C.-T. Liu (1996), Winter upwelling off Luzon in the northeastern South China Sea, *J. Geophys. Res. Oceans*, *101*(C7), 16435-16448, doi:10.1029/96JC01064.

Shchepetkin, A. F., and J. C. McWilliams (2005), The regional oceanic modeling system (ROMS): a split-explicit, free-surface, topography-following-coordinate oceanic model, *Ocean Model*, *9*(4), 347-404, doi:10.1016/j.ocemod.2004.08.002.

Shigemitsu, M., T. Okunishi, J. Nishioka, H. Sumata, T. Hashioka, M. N. Aita, S. L. Smith, N. Yoshie, N. Okada, and Y. Yamanaka (2012), Development of a one-dimensional ecosystem model including the iron cycle applied to the Oyashio region, western subarctic Pacific, *J. Geophys. Res.*, *117*(C6), doi:10.1029/2011jc007689.

Siegel, D. A., D. J. McGillicuddy, and E. A. Fields (1999), Mesoscale eddies, satellite altimetry, and new production in the Sargasso Sea, *J. Geophys. Res.*, *104*(C6), 13359, doi:10.1029/1999jc900051.

Siegel, D. A., P. Peterson, D. J. McGillicuddy, S. Maritorena, and N. B. Nelson (2011), Bio-optical footprints created by mesoscale eddies in the Sargasso Sea, *Geophys. Res. Lett.*, *38*(13), doi:10.1029/2011gl047660.

Sverdrup, H. (1953), On conditions for the vernal blooming of phytoplankton, *Journal du Conseil*, *18*(3), 287-295.

Tang, D.-L., I.-H. Ni, D. R. Kester, and F. E. Muller-Karger (1999), Remote sensing observations of winter phytoplankton blooms southwest of the Luzon Strait in the South China Sea, *Marine Ecology-Progress Series*, *191*, 43.

Tian, J., Q. Yang, and W. Zhao (2009), Enhanced Diapycnal Mixing in the South China Sea, *J. Phys. Oceanogr.*, *39*(12), 3191-3203, doi:10.1175/2009jpo3899.1.

Townsend, D. W., M. D. Keller, M. E. Sieracki, and S. G. Ackleson (1992), Spring phytoplankton blooms in the absence of vertical water column stratification, *Nature*, *360*(6399), 59-62.

Tseng, C.-M. (2005), A unique seasonal pattern in phytoplankton biomass in low-latitude waters in the South China Sea, *Geophys. Res. Lett.*, *32*(8), doi:10.1029/2004gl022111.

Tseng, C. M., G. C. Gong, L. W. Wang, K. K. Liu, and Y. Yang (2009), Anomalous biogeochemical conditions in the northern South China Sea during the El-

Niño events between 1997 and 2003, *Geophys. Res. Lett.*, *36*(14), L14611, doi:10.1029/2009gl038252.
Wang, G., D. Chen, and J. Su (2006), Generation and life cycle of the dipole in the South China Sea summer circulation, *J. Geophys. Res.*, *111*(C6), doi:10.1029/2005jc003314.
Wang, G., J. L. Su, and P. C. Chu (2003), Mesoscale eddies in the South China Sea observed with altimeter data, *Geophys. Res. Lett.*, *30*(21), doi:10.1029/2003gl018532.
Wang, G., D. Wang, and T. Zhou (2012), Upper layer circulation in the Luzon Strait, *Aquatic Ecosystem Health & Management*, *15*(1), 39-45.
Wang, G., S. P. Xie, T. Qu, and R. X. Huang (2011), Deep South China Sea circulation, *Geophys. Res. Lett.*, *38*(5).
Wang, J. (1986), Observation of abyssal flows in the northern South China Sea, *Acta Oceanogr. Taiwan*, *16*, 36-45.
Wang, J., H. Hong, Y. Jiang, F. Chai, and X.-H. Yan (2013), Summer nitrogenous nutrient transport and its fate in the Taiwan Strait: A coupled physical-biological modeling approach, *J. Geophys. Res. Oceans*, *118*(9), 4184-4200, doi:10.1002/jgrc.20300.
Wang, J. J., D. L. Tang, and Y. Su (2010), Winter phytoplankton bloom induced by subsurface upwelling and mixed layer entrainment southwest of Luzon Strait, *J. Mar. Syst.*, *83*(3-4), 141-149, doi:10.1016/j.jmarsys.2010.05.006.
Wong, G. T. F. (2002), Nitrate anomaly in the upper nutricline in the northern South China Sea - Evidence for nitrogen fixation, *Geophys. Res. Lett.*, *29*(23), doi:10.1029/2002gl015796.
Wong, G. T. F., T. L. Ku, M. Mulholland, C. M. Tseng, and D. P. Wang (2007), The SouthEast Asian time-series study (SEATS) and the biogeochemistry of the South China Sea - An overview, *Deep Sea Res. Part II*, *54*(14-15), 1434-1447, doi:10.1016/j.dsr2.2007.05.012.
Wyrtki, K. (1961), Physical Oceanography of the Southeast Asian waters, edited.
Wyrtki, K. (1965), The average annual heat balance of the North Pacific Ocean and its relation to ocean circulation, *J. Geophys. Res.*, *70*(18), 4547-4559.
Xie, S.-P., K. Hu, J. Hafner, H. Tokinaga, Y. Du, G. Huang, and T. Sampe (2009), Indian Ocean capacitor effect on Indo-western Pacific climate during the summer following El Niño, *J. Clim.*, *22*(3), 730-747.
Xie, S. P., Q. Xie, D. Wang, and W. T. Liu (2003), Summer upwelling in the South China Sea and its role in regional climate variations, *J. Geophys. Res. Oceans*, *108*(C8).
Xiu, P., and F. Chai (2014), Connections between physical, optical and biogeochemical processes in the Pacific Ocean, *Prog. Oceanogr.*, *122*, 30-53, doi:10.1016/j.pocean.2013.11.008.
Xiu, P., F. Chai, L. Shi, H. Xue, and Y. Chao (2010), A census of eddy activities in the South China Sea during 1993–2007, *J. Geophys. Res.*, *115*(C3), C03012.

Xu, F.-H., and L.-Y. Oey (2014), State analysis using the Local Ensemble Transform Kalman Filter (LETKF) and the three-layer circulation structure of the Luzon Strait and the South China Sea, *Ocean Dyn.*, *64*(6), 905-923, doi:10.1007/s10236-014-0720-y.

Yang, H., Q. Liu, and X. Jia (1999), On the upper oceanic heat budget in the South China Sea: Annual cycle, *Adv. Atmos. Sci.*, *16*(4), 619-629.

Yang, H., and L. Wu (2012), Trends of upper-layer circulation in the South China Sea during 1959-2008, *J. Geophys. Res. Oceans*, *117*(C8), doi:10.1029/2012jc008068.

Yang, Q., W. Zhao, X. Liang, and J. Tian (2016), Three-Dimensional Distribution of Turbulent Mixing in the South China Sea, *J. Phys. Oceanogr.*, *46*(3), 769-788.

Zheng, Z.-W., Q. Zheng, Y.-C. Kuo, G. Gopalakrishnan, C.-Y. Lee, C.-R. Ho, N.-J. Kuo, and S.-J. Huang (2016), Impacts of coastal upwelling off east Vietnam on the regional winds system: An air-sea-land interaction, *Dyn. Atmos. Oceans*, doi:10.1016/j.dynatmoce.2016.10.002.

Zhuang, W., Y. Du, D. Wang, Q. Xie, and S. Xie (2010a), Pathways of mesoscale variability in the South China Sea, *Chin. J. Oceanol. Limnol.*, *28*, 1055-1067.

Zhuang, W., S.-P. Xie, D. Wang, B. Taguchi, H. Aiki, and H. Sasaki (2010b), Intraseasonal variability in sea surface height over the South China Sea, *J. Geophys. Res.*, *115*(C4), doi:10.1029/2009jc005647.

Appendix A

PUBLISHED PAPERS DURING PHD STUDY

W. Lu, X.-H. Yan, L. Han, and Y. Jiang (2017), One-dimensional ocean model with three types of vertical velocities: a case study in the South China Sea, *Ocean Dyn.*, 1-10, doi:10.1007/s10236-016-1029-9.

W. Lu, X.-H. Yan, and Y. Jiang (2015), Winter bloom and associated upwelling northwest of the Luzon Island: A coupled physical-biological modeling approach, *J. Geophys. Res. Oceans*, 120(1), 533-546, doi:10.1002/2014JC010218.

Liao, E., **W. Lu**, X.-H. Yan, Y. Jiang, and A. Kidwell (2015), The coastal ocean response to the global warming acceleration and hiatus, *Scientific Reports*, 5, 16630, doi:10.1038/srep16630.

W. Lu, Y. Jiang, and J. Lin (2013), MODELING PROPAGATION OF 2011 HONSHU TSUNAMI, *Engineering Applications of Computational Fluid Mechanics*, 7(4), 507-518.

W. Lu, X.-H. Yan, Y. Jiang, E. Liao, W. Zhuang, and L. Oey (2017), On the controlling factors of the productivity in the summer Vietnam upwelling system (*in preperation*).

W. Lu, X.-H. Yan, and Y. Jiang (2017), Comparative modeling the spatio-temporal variability of carbon sequestration in the South China Sea (*in preperation*).

Appendix B

PERMISSION FROM JOURNAL OF GEOPHYSICAL RESEARCH: OCEANS

This Agreement between Mr. Wenfang Lu ("You") and John Wiley and Sons ("John Wiley and Sons") consists of your license details and the terms and conditions provided by John Wiley and Sons and Copyright Clearance Center.

License Number	4121840754482
License date	Jun 04, 2017
Licensed Content Publisher	John Wiley and Sons
Licensed Content Publication	Journal of Geophysical Research: Oceans
Licensed Content Title	Winter bloom and associated upwelling northwest of the Luzon Island: A coupled physical-biological modeling approach
Licensed Content Author	Wenfang Lu,Xiao-Hai Yan,Yuwu Jiang
Licensed Content Date	Jan 29, 2015
Licensed Content Pages	14
Type of use	Dissertation/Thesis
Requestor type	Author of this Wiley article
Format	Print and electronic
Portion	Full article
Will you be translating?	Yes, including English rights
Number of languages	1
Languages	English; Chinese

Title of your thesis / dissertation	PHYSICAL MODULATION TO THE BIOLOGICAL PRODUCTION IN THE SOUTH CHINA SEA: A PHYSICAL-BIOLOGICAL COUPLED MODEL APPROACH
Expected completion date	Aug 2017
Expected size (number of pages)	120
Requestor Location	Mr. Wenfang Lu C3-401, Xiping building Xiamen University Xiang'An Campus Xiamen, Fujian 361105 China Attn: Mr. Wenfang Lu
Publisher Tax ID	EU826007151
Billing Type	Invoice
Billing Address	Mr. Wenfang Lu C3-401, Xiping building Xiamen University Xiang'An Campus Xiamen, China 361105 Attn: Mr. Wenfang Lu
Total	0.00 USD

Appendix C

PERMISSION FROM OCEAN DYNAMICS

License Number	4159251177145
License date	Jul 31, 2017
Licensed Content Publisher	Springer
Licensed Content Publication	Ocean Dynamics
Licensed Content Title	One-dimensional ocean model with three types of vertical velocities: a case study in the South China Sea
Licensed Content Author	Wenfang Lu
Licensed Content Date	Jan 1, 2016
Licensed Content Volume	67
Licensed Content Issue	2
Type of Use	Thesis/Dissertation
Portion	Full text
Number of copies	1
Author of this Springer article	Yes and you are the sole author of the new work
Order reference number	
Title of your thesis / dissertation	PHYSICAL MODULATION TO THE BIOLOGICAL PRODUCTION IN THE SOUTH CHINA SEA: A PHYSICAL-BIOLOGICAL COUPLED MODEL APPROACH

Expected completion date	Aug 2017
Estimated size(pages)	120
Requestor Location	Mr. Wenfang Lu C3-401, Xiping building Xiamen University Xiang'An Campus Xiamen, Fujian 361105 China Attn: Mr. Wenfang Lu
Billing Type	Invoice
Billing Address	Mr. Wenfang Lu C3-401, Xiping building Xiamen University Xiang'An Campus Xiamen, China 361105 Attn: Mr. Wenfang Lu
Total	0.00 USD